TU Delft

Delft University of Technology

Reader-friendly Edible Binarycodes and Sensors Based on Smart Hydrogel

Zhang, M.

DOI
10.4233/uuid:8570eb94-279e-4a3c-b662-b999fdac517c

Publication date
2024

Document Version
Final published version

Citation (APA)
Zhang, M. (2024). *Reader-friendly Edible Binarycodes and Sensors Based on Smart Hydrogel*. [Dissertation (TU Delft), Delft University of Technology]. https://doi.org/10.4233/uuid:8570eb94-279e-4a3c-b662-b999fdac517c

Important note
To cite this publication, please use the final published version (if applicable).
Please check the document version above.

Copyright
Other than for strictly personal use, it is not permitted to download, forward or distribute the text or part of it, without the consent of the author(s) and/or copyright holder(s), unless the work is under an open content license such as Creative Commons.

Takedown policy
Please contact us and provide details if you believe this document breaches copyrights.
We will remove access to the work immediately and investigate your claim.

This work is downloaded from Delft University of Technology.
For technical reasons the number of authors shown on this cover page is limited to a maximum of 10.



Reader-friendly Edible Binarycodes and Sensors Based on Smart Hydrogel

Mengmeng Zhang

Reader-friendly edible Binarycodes and sensors based on smart hydrogel

Mengmeng Zhang

Reader-friendly Edible Binarycodes and Sensors Based on Smart Hydrogel

Dissertation

for the purpose of obtaining the degree of doctor
at Delft University of Technology
by the authority of the Rector Magnificus, prof.dr.ir. T.H.J.J. van der Hagen,
chair of the Board for Doctorates
to be defended publicly on
Monday 12 February 2024 at 10 o'clock

by

Mengmeng ZHANG

Master of Science in Materials Science, Yantai University, China
born in Shandong, China.

This dissertation has been approved by the promotors.
Composition of the doctoral committee:

Rector Magnificus,	chairperson
Dr.habil. E. Mendes	Delft University of Technology, promoter
Dr. H. B. Eral	Delft University of Technology, copromoter
Independent members:	
Prof.dr. J.H. van Esch	Delft University of Technology
Prof.dr.ir. T.J.H. Vlugt	Delft University of Technology
Prof.dr.ir. J.T. Padding	Delft University of Technology
Dr. C. M. Marques	Délégation Alsace du CNRS, France
Dr. V. Garbin	Delft University of Technology
Prof.dr. S.J. Picken	Delft University of Technology, reserve member

This research was supported by the China Scholarship Council (CSC) under Grant No. 201808370175.

Cover by: Mengmeng Zhang

Printed by: Ridderprint

Copyright © 2024 by M. Zhang, all rights reserved
978-94-6366-812-5
An electronic version of this dissertation is available at
http://repository.tudelft.nl/

to my parents and sister
to my young man Zelu

CONTENTS

SUMMARY ix

SAMENVATTING xi

Part I 1

1 INTRODUCTION 3
- 1.1 Counterfeiting and deterioration: global threats to health and trust 3
- 1.2 The limitations of current advanced packaging and sensor technologies in combating counterfeiting and deterioration 4
- 1.3 Thesis outline 5
- References 7

2 TEMPLATED HYDROGEL MICROPARTICLES FOR ANTICOUNTERFEITING 9
- 2.1 Introduction 10
- 2.2 Materials and methods 11
  - 2.2.1 Hydrogel microparticle synthesis 11
  - 2.2.2 Finite element simulations 12
- 2.3 Results and discussion 13
  - 2.3.1 Hydrogel microparticle synthesis strategy 13
  - 2.3.2 Optimization of trapping efficiency 17
- 2.4 Conclusion 23
- References 26

3 PUF MICROPARTICLES FOR ANTICOUNTERFEITING 31
- 3.1 Introduction 32
- 3.2 Materials and methods 35
  - 3.2.1 Materials 35
  - 3.2.2 Preparation of single-diameter PUF microparticle 35
  - 3.2.3 Preparation of oil/water PUF microparticle 35
- 3.3 Results and discussion 36
  - 3.3.1 Two types of on-dose PUF microparticle 36
  - 3.3.2 Working algorithm 39
  - 3.3.3 Evaluation of single-diameter on-dose PUF 42
- 3.4 Conclusion 46
- References 47

4 HUMIDITY INDICATOR 51
- 4.1 Introduction 52
- 4.2 Materials and methods 54

4.2.1 Fabrication of the EHI . . . 54
4.2.2 Protocol of demonstrations . . . 55
4.2.3 Thermogravimetric analysis (TGA) . . . 55
4.2.4 Thickness and aspect ratio test . . . 55
4.3 Results and discussion . . . 56
4.3.1 Fabrication and demonstration . . . 56
4.3.2 Rolling mechanism . . . 60
4.3.3 Tunability . . . 63
4.4 Conclusion . . . 68
References . . . 69
5 TIME-TEMPERATURE INDICATOR 73
5.1 Introduction . . . 74
5.2 Materials and methods . . . 75
5.2.1 Fabrication of pitaya extracts and alginate-based TTI . . . 75
5.2.2 Thermal behavior test under various pH conditions . . . 76
5.2.3 Colorimetric assay . . . 76
5.2.4 Modified atmosphere test . . . 77
5.2.5 Plate count test of *L. casei Shirota* . . . 77
5.3 Results and discussion . . . 79
5.3.1 Color evolution behavior of pitaya extracts . . . 79
5.3.2 Alginate-based TTI . . . 85
5.4 Conclusion . . . 89
References . . . 90
6 CONCLUSIONS 93
Part II Appendixes 97
A APPENDIX TO CHAPTER 2 TEMPLATED HYDROGEL MICROPARTICLES FOR ANTICOUNTERFEITING 99
A.1 Mobile phase . . . 99
A.2 Size and velocity, geometry and spacing based on COMSOL simulation . 100
A.2.1 Size . . . 100
A.2.2 Velocity profile . . . 103
A.2.3 Geometries . . . 104
A.2.4 Spacing . . . 108
A.3 Validation . . . 111
A.4 Movies . . . 112
B APPENDIX TO CHAPTER 3 PUF MICROPARTICLES FOR ANTICOUNTERFEITING 113
B.1 Image processing . . . 113

B.2 Data for NIST statistical testing suite . . . 114
B.3 Matlab code . . . 115
B.4 Images for performance investigation . . . 116
B.5 Raw results - NIST statistical test suite . . . 118
B.6 Hamming distances . . . 120
C APPENDIX TO CHAPTER 4 HUMIDITY INDICATOR 121
C.1 TGA test . . . 121
C.2 Characteristic study of casein/glycerol film . . . 122
C.3 Bending behavior study . . . 125
C.4 More example applications . . . 126
C.5 Movies . . . 127
D APPENDIX TO CHAPTER 5 TIME-TEMPERATURE INDICATOR 129
D.1 Two degradation pathways . . . 129
D.2 Color evolution under various conditions . . . 130

Part III 133

ACKNOWLEDGMENTS 135

CURRICULUM VITÆ 141

LIST OF PUBLICATIONS 143

SUMMARY

Food and medicines are two of the most essential categories of goods for human beings, providing vital nourishment and healthcare. However, as these products are commercialized and distributed on a global scale, consumers face the threat of counterfeit and deteriorated products. In response, this dissertation presents four prototypes consisting of On-Dose-Authentication (ODA) binarycodes and battery-less indicators based on smart hydrogel that are edible and reader-friendly to address these issues.

First, a microfluidic platform for continuous synthesis of hydrogel microparticles with superparamagnetic colloids (SPCs) embedded at prescribed positions has been established. The shape of the cross-linked microparticle is independently controlled by stop-flow lithography, whereas the position of trapped SPCs is dictated by virtual magnetic molds made of 2D nickel patches facilitating magnetic trapping. The spatial positions of trapped SPCs collectively function as a binary code matrix for product authentication. The proposed magnetic microparticles will contribute to the development of soft matter-inspired product quality control, tracking, and anti-counterfeiting technologies. (Chapter 2)

Second, a Physical Unclonable Functions (PUF) algorithm was developed to enhance the ODA binary codes' safety level. This algorithm exploits the diameter and coordinates of spheres as input, abandoning color and intensity as inputs, enabling imaging using common illumination and low-magnification microscopy hence lifting the reading constraints to advanced labs that are usually found in other current graphical PUF systems. Two sets of Poly(ethylene glycol) diacrylate ODA-PUF tags that can be read out via this algorithm were fabricated. The sets are single-diameter PUF leveraging random distributed superparamagnetic colloids of identical diameters and multiple-diameter PUF utilizing vortexed sunflower oil drops of various diameters, respectively. The performance of the single-diameter system was investigated. It passed NIST Statistical tests, demonstrating sufficient randomness, ideal bit uniformity, Hamming distance, and device uniqueness. The encoding capacity of the single-diameter system was found to be 9.2×10^{18}, which can satisfy labeling the annual output of Aspirin. (Chapter 3)

Third, a humidity indicator has been created that mechanically bends and rolls itself irreversibly upon exposure to high humidity conditions. The indicator is made of two food-grade polymer films with distinct ratios of a milk protein, casein, and a plasticizer, glycerol, that are physically attached to each other. Based on the thermogravimetric analysis and microstructural characterization, the bending mechanism is a result of hygroscopic swelling and consequent counter diffusion of water and glycerol. Guided by this mechanism, the rolling behavior, including response time and final curvature, can be tuned by the

geometric dimensions of the indicator. As the proposed indicator is made of food-grade ingredients, it can be placed directly in contact with perishable products to report exposure to undesirable humidity inside the package, without the risk of contaminating the product or causing oral toxicity in case of accidental ingestion - features that commercial inedible electronic and chemo-chromatic sensors cannot provide presently. (Chapter 4)

Finally, an alginate TTI bead that encapsulates betacyanin, a natural colorant extracted from purple pitaya, is proposed to continuously monitor and reflect the temperature history of the perishable products to diagnose the storage conditions. The instability of betacyanin is exploited to demonstrate undesirable temperature abuse through visual color changes. The thermochromic change of the purple pitaya extract and the pitaya-extract-encapsulated bead was investigated under various temperatures, pH, and gaseous atmosphere conditions. Experimental results show that the proposed TTI exhibits an irreversible thermochromic change under a wide operation temperature range up to at least 100 °C with negligible disturbance from the gaseous composition. (Chapter 5)

SAMENVATTING

Twee van de meest essentiële basisbehoeften van de mens zijn medicijnen en voedsel, zij zijn essentieel voor de gezondheid van de mens. Echter, het in industraliseren en globaliseren van de voedsel en medicijnen industrie heeft als effect dat de staan consumenten bloot kan staan aan de dreiging van namaak en minder kwalitatieve producten. Als reactie hierop presenteert deze dissertatie vier items die alle bestaan uit On-Dose-Authentication (ODA) binaire codes en batterijloze sensoren op basis van slimme hydrogel. Deze laatste zijn eetbaar en eenvoudig af te lezen om de hierboven genoemden problemen aan te pakken.

Ten eerste is er een microfluïdisch platform opgezet voor de continue synthese van hydrogel-micropartikels met superparamagnetische colloïden (SPC's) ingebed op voorgeschrevenposities. De vorm van de cross-linked micropartikel wordt onafhankelijk gecontroleerd door stop-flow lithografie. Tegelijkertijd wordt de positie van de opgesloten SPC's bepaald door virtuele magnetische mallen gemaakt van 2D nikkel platen die magnetische vangst mogelijk maken. De ruimtelijke posities van de SPC's functioneren collectief als een binair-code-matrix voor productauthenticatie. De voorgestelde magnetische micropartikels zullen bijdragen aan de ontwikkeling van soft matter-geïnspireerde kwaliteits controle, tracking technologieën en het bevorderen van het bestrijden van namaak producten. (Hoofdstuk 2)

Ten tweede is er een Physical Unclonable Functions (PUF) algoritme ontwikkeld om het veiligheidsniveau van de ODA binaire codes te verhogen. Dit algoritme maakt gebruik van de diameter en coördinaten van bollen als input. Waarbij de kleur en intensiteit als input worden genegeerd. Hierdoor is het mogelijk om afbeeldingen te krijgen die gemaakt zijn met microscopen die een lage vergroting hebben. Hiermee vervalt de noodzaak om gebruik te maken van PUF systemen die vooral benut worden in geavanceerde laboratoria. Twee sets Poly(ethylene glycol) diacrylaat ODA-PUF tags werden vervaardigd die vervolgens kunnen worden uitgelezen door dit algoritme. De sets zijn een vaste diameter PUF die gebruik maakt van willekeurig verdeelde superparamagnetische colloïden van identieke diameters . Een multi-diameter PUF die gebruik maakt van vortexed zonnebloem olie druppels van verschijnende diameters. Het prestatieniveau van het vaste diameter systeem werd onderzocht en slaagde voor NIST Statistische tests, waarbij voldoende willekeurigheid, ideale bit uniformiteit, Hamming-afstand en apparaat uniciteit werden gedemonstreerd. De coderingscapaciteit van het vaste diameter systeem werd vastgesteld op 9.2×10^{18}, wat voldoende is voor het labelen van de jaarlijkse output van Aspirine (hoofdstuk 3).

Ten derde is er een luchtvochtigheidsindicator ontwikkeld die zichzelf mechanisch irreversibel buigt en oprolt bij blootstelling aan hoge luchtvochtigheidsomstandigheden. De indicator bestaat uit twee voedselveilige polymeerfilms met verschillende verhoudingen van melkeiwit, caseïne, en de weekmaker glycerol, die fysiek aan elkaar zijn bevestigd. Op basis van de thermogravimetrische analyse en microstructurele karakterisering. Blijkt dat het buigmechanisme het gevolg is van hygroscopische zwelling en daaropvolgende counter diffusie van water glycerol. Gebaseerd op dit mechanisme kan het rolgedrag, inclusief reactietijd en uiteindelijke kromming, worden afgestemd op de geometrische afmetingen van de indicator. Aangezien de hier eerder genoemde indicator gemaakt is van voedselveilige ingrediënten, kan deze rechtstreeks in contact worden gebracht met bederfelijke producten om blootstelling aan ongewenste luchtvochtigheid in de verpakking te melden. Hierdoor is er geen risico van besmetting van het product of het veroorzaken van orale toxiciteit bij accidentele inname. Dit kunnen de huidige niet-eetbare elektronische en chemo-chromatische sensoren momenteel niet. (hoofdstuk 4)

Tot slot wordt een alginaat TTI bead voorgesteld die betacyanine, een natuurlijk kleurmiddel uit paarse pitaya, omhult en continu de temperatuurgeschiedenis van bederfelijke producten kan monitoren en de opslagomstandigheden te diagnosticeren. De instabiliteit van betacyanine wordt benut om ongewenst temperatuurmisbruik aan te tonen door middel van visuele kleurveranderingen. De thermochromische verandering van het paarse pitaya-extract en de pitaya-extract-omhulde kraal werd onderzocht onder verschillende temperaturen, pH en gasvormige atmosfeeromstandigheden. Experimentele resultaten tonen aan dat de voorgestelde TTI een irreversibele thermochromische verandering vertoont onder een breed werktemperatuurbereik tot ten minste 100 °C met verwaarloosbare verstoring van de gas samenstelling. (Hoofdstuk 5)

PART I

1 INTRODUCTION

1.1 Counterfeiting and deterioration: global threats to health and trust

The convenience brought about by the commercialization of food and medicines has undoubtedly improved the lives of many worldwide. However, this convenience is overshadowed by the alarming prevalence of counterfeit and deteriorated products, posing significant risks to consumers' well-being.

Counterfeiters target a wide range of pharmaceutical products, including vaccines, common antibiotics, anti-malarial drugs, cancer treatments, and other life-saving medications[1]. These fraudulent practices not only undermine individual health but also have a significant global impact on public health. For instance, developing countries spend approximately $30.5 billion on substandard and falsified medications, resulting in an estimated 100,000 deaths annually in Africa alone[2, 3].

While counterfeiting is a deliberate criminal act, deteriorated products often result from the unintended consequences of improper storage. Many of the improper storage instances are attributed to fluctuations in temperature and humidity, which can compromise products' quality and effectiveness. For example, insulin is sensitive to temperature fluctuations and can be only stored in a narrow temperature range from 4 to 8 °C to maintain its potency. Similarly, the polyunsaturated fatty acids in the infant milk formula powder are prone to oxidize due to improper storage not just high temperature but also high moisture, posing the newborns at high risk[4]. It is hard to provide an exact figure of diabetic patients and babies affected. However, 80% of diabetics were reported to store insulin at the wrong temperature at household[5]. Improper storage led to the disposal of 550 million infant formula cans in 2009[6].

The implications of counterfeit and deteriorated medicines and foodstuffs extend far beyond individual health risks. These practices undermine economies, lead to substantial wastage, endanger public health, and erode trust and confidence in brands. To address these pressing concerns, effective measures such as advanced packaging and monitoring systems are imperative to ensure the authenticity and quality of products, safeguarding the welfare of consumers, and preserving public trust. To this end, advanced packaging

and sensor technologies in combating counterfeiting and deterioration are a step in the right direction.

1.2 The limitations of current advanced packaging and sensor technologies in combating counterfeiting and deterioration

Advanced packaging solutions, such as barcodes, holograms, and Radio Frequency Identification (RFID)[7], have been used to improve product authentication and distribution supervision. However, these solutions have limitations. These include high costs, restricted accessibility to advanced laboratory facilities for authentication, vulnerability to theft or recycling for counterfeit purposes, and conflicts with sustainability goals with excessive packaging.

As a potentially powerful tool to combat rampant counterfeiting on the packaging, the on-dose authentication (ODA) measure used as "in-drug labeling" is introduced[8]. ODA labels are usually made from biocompatible or edible materials that are directly embedded into the end products themselves. The well-explored ODA measures include microtaggants[9, 10], encoded-multifunctional hydrogel microparticles, physically unclonable function (PUF) barcodes[11], 3D printed medicines[12], covert films[13], etc. These ODA measures offer advantages such as direct embedding into products, micro-scale fabrication, and compatibility with portable optical instruments for easy reading. However, the easy-to-read measures can be cracked and imitated, while more secure options involve complex data processing and expensive equipment, making them less suitable for low-priced items.

Ideal ODA should not only ensure readability but also guarantee a robust level of cryptographic security. In this context, employing a dual-authentication ODA label that combines both optical and magnetic verification represents a significant stride toward achieving this goal. Furthermore, the exploration of PUF, which functions as fingerprints hence known for its unclonable nature[11], can further enhance its readability and security.

On the other hand, as an effective solution to maintain product quality, the current storage monitoring systems for storage environments primarily focus on overseeing the environmental conditions of entire batches of goods. However, this approach results in significant and unnecessary waste due to the fact that each unique item may be subjected to different environmental conditions. These regulations mandate the disposal of entire batches upon detecting unfavorable conditions, even if some items remain safe. Moreover, the ongoing issue of product deterioration is exacerbated by inadequate storage practices among downstream participants in the distribution chain. Specifically, customers often lack the necessary capital and knowledge to implement proper storage conditions, leading to suboptimal environments for preserving product quality[14, 15]. This lack of awareness and resources further perpetuates the problem of product deterioration, posing significant

challenges in maintaining the freshness and quality of goods throughout the distribution process.

In response to the above challenges in monitoring systems, innovative solutions are imperative. Biocompatible, battery-less, and low-cost quality control indicators are believed to offer a more dependable approach to ensure the safety on a single product level. These indicators can provide real-time information about the specific conditions each product is exposed to, and empower consumers with the knowledge they need to handle products properly, allowing for targeted interventions to prevent spoilage or degradation. By shifting the focus from batch-level monitoring to individual product-level tracking, we can potentially revolutionize the way we ensure product quality and safety throughout the supply chain.

1.3 Thesis outline

This thesis presents a range of prototypes for On-Dose-Authentication (ODA) binarycodes and battery-less indicators that aim to address the issues of counterfeit and deteriorated products respectively.

Chapter 2 presents a microfluidic platform designed for the continuous synthesis of hydrogel microparticles with embedded superparamagnetic colloids (SPCs) at specific positions. The shape of the cross-linked microparticles is controlled through stop-flow lithography, while the positions of the trapped SPCs are determined by virtual magnetic molds composed of 2D nickel patches, which enable magnetic trapping. The spatial arrangement of the trapped SPCs serves as a binary code matrix for product authentication.

Combining analytical and finite element methods, the study enhances SPC trapping efficiency by investigating magnetic field microgradients produced by nickel patches. These magnetic microparticles, based on soft matter principles and a binary code matrix formed by embedded SPC positions, have the potential to transform product quality control, tracking, and anti-counterfeiting methods.

Chapter 3 focuses on graphical Physical Unclonable Functions (PUF). This system offers an efficient and unclonable method of authentication, even if the counterfeiter is aware of the production process. However, existing graphical PUFs rely on specific illumination and detection technology, making them impractical for use outside advanced laboratories. Additionally, these PUFs often employ toxic fluorophores or nanowires, limiting their application in edible products like pharmaceuticals and foods.

To address these limitations, this chapter introduces an optical physically unclonable function (PUF) synthesized by randomly embedding superparamagnetic colloids and emulsion droplets within biocompatible hydrogel particles to generate cryptographic keys. The proposed PUFs can be placed directly on tagged product acting as on-dose authentication measures due to their biocompatible nature. Two types of on-dose PUFs are showcased:

one utilizing superparamagnetic colloids with a single particle diameter (single-diameter), and the other utilizing vortexed sunflower oil droplets with broad size distribution(multiple-diameter). We demonstrate that the proposed PUFs offer sufficient statistical randomness and thus are unclonable, providing extra security. Moreover, they allow imaging under white light illumination and low-magnification microscopy, thereby making the reading process more accessible.

Chapter 4 introduces a humidity indicator that exhibits irreversible mechanical bending and rolling when exposed to high humidity conditions. The indicator consists of two food-grade polymer films, with varying ratios of casein (a milk protein) and glycerol (a plasticizer), which are physically attached to each other. The bending mechanism sounds mainly driven by hygroscopic swelling and the subsequent counter-diffusion of water and glycerol, as suggested by thermogravimetric analysis and microstructural characterization. Based on the hygroscopic swelling mechanism, we demonstrate the rolling behavior of the indicator, including response time and final curvature, can be adjusted by manipulating its geometric dimensions. This flexibility allows for customization and optimization of the indicator's performance according to specific requirements.

To diagnose eventual temperature abuse, **Chapter 5** proposes an alginate time-temperature indicator (TTI) bead that contains betacyanin, a natural colorant derived from purple pitaya. The instability of betacyanin is leveraged to indicate undesirable temperature abuse through visual color changes. The thermochromic properties of the purple pitaya extract and the encapsulated bead are investigated under various temperature, pH, and gaseous atmosphere conditions. Experimental results reveal that the proposed TTI exhibits an irreversible thermochromic change over a wide temperature range, with operations up to at least 100 °C, while remaining unaffected by the gaseous composition. This indicates its suitability for monitoring food storage conditions. Additionally, the TTI has shown promise for labeling chilled foods in situations where sensory detection of heat-induced damage is impractical, which is illustrated by its successful application in drinkable probiotics.

This dissertation is composed of six chapters, some of which are derived from previously published articles. Chapter 2 to Chapter 5 are self-contained and stand-alone pieces that do not rely on the prior reading of preceding chapters. Each chapter includes its own introduction, literature review, and bibliography. Therefore, readers can choose to directly access the chapter of their interest without sacrificing the overall continuity of the thesis.

REFERENCES

[1] K. Dégardin, Y. Roggo, and P. Margot. "Understanding and fighting the medicine counterfeit market." *Journal of pharmaceutical and biomedical analysis* 87 (2014), pp. 167–175.

[2] W. H. Organization. *A study on the public health and socioeconomic impact of substandard and falsified medical products*. Tech. rep. 2017.

[3] S. M. Beargie et al. "The economic impact of substandard and falsified antimalarial medications in Nigeria." *PloS one* 14.8 (2019), e0217910.

[4] D. Wang, H. Xiao, X. Lyu, H. Chen, and F. Wei. "Lipid oxidation in food science and nutritional health: A comprehensive review." *Oil Crop Science* 8.1 (2023), pp. 35–44.

[5] K. Braune, L. A. Kraemer, J. Weinstein, A. Zayani, and L. Heinemann. "Storage Conditions of Insulin in Domestic Refrigerators and When Carried by Patients: Often Outside Recommended Temperature Range." *Diabetes Technol Ther* 21.5 (2019), pp. 238–244.

[6] N. Joffe, F. Webster, and N. Shenker. *Support for breastfeeding is an environmental imperative*. Tech. rep. 2019.

[7] R. Shah, P. Prajapati, and Y. Agrawal. "Anticounterfeit packaging technologies." *Journal of advanced pharmaceutical technology & research* 1 (2010), pp. 368–73.

[8] H. Zhang et al. "Materials and technologies to combat counterfeiting of pharmaceuticals: current and future problem tackling." *Advanced Materials* 32.11 (2020), p. 1905486.

[9] S. Han et al. "Lithographically Encoded Polymer Microtaggant Using High-Capacity and Error-Correctable QR Code for Anti-Counterfeiting of Drugs." *Advanced Materials* 24.44 (2012), pp. 5924–5929.

[10] I. Rehor et al. "Biodegradable Microparticles for Simultaneous Detection of Counterfeit and Deteriorated Edible Products." *Small* 13.39 (2017), p. 1701804.

[11] J. W. Leem et al. "Edible unclonable functions." *Nature Communications* 11.1 (2020), p. 328.

[12] S. J. Trenfield et al. "Track-and-trace: Novel anti-counterfeit measures for 3D printed personalized drug products using smart material inks." *International Journal of Pharmaceutics* 567 (2019), p. 118443.

[13] S. Takei. "Safety-oriented photolithography of water-soluble resist using water-coating and water-developable processes for edible pharmaceutical polymer films." *Applied Physics Express* 11.8 (2018), p. 086501.

[14] M. Terpstra, L. Steenbekkers, N. De Maertelaere, and S Nijhuis. "Food storage and disposal: Consumer practices and knowledge." *British Food Journal* 107.7 (2005), pp. 526–533.

[15] J. Aschemann-Witzel, I. De Hooge, P. Amani, T. Bech-Larsen, and M. Oostindjer. "Consumer-related food waste: Causes and potential for action." *Sustainability* 7.6 (2015), pp. 6457–6477.

2

TEMPLATED HYDROGEL MICROPARTICLES FOR ANTICOUNTERFEITING

This chapter is based on the article:
Zhang, M., Warth, T., Boon, N., Demirörs, A. F., Eral, H. B., Microfluidic Synthesis of Hydrogel Microparticles with Superparamagnetic Colloids Embedded at Prescribed Positions for Anticounterfeiting Applications. Advanced Material Interfaces 2022, 9, 2200899.

2.1 Introduction

Globalization has enabled unprecedented ease of access to products for consumers. However, this ease of access has also exposed consumers to an alarming number of counterfeit products [1, 2]. This is especially worrisome when the products targeted are vaccines, antibiotics, and other life-saving commodities. While the products themselves are difficult to imitate, labels and packaging can be easily manipulated. Common counterfeiting strategies include: (i) tampering with the details on authentic packaging (e.g. altering the expiry date), (ii) using authentic packaging for counterfeit products to pass off counterfeits as authentic. In response, manufacturers and researchers have developed advanced packaging solutions. Some representative solutions are barcodes, holograms, sealing tapes, radio frequency identification devices (RFID)[3], watermarks, and optical/-chemical/biological (DNA) tags[4]. Unfortunately, most of these solutions are not widely implemented due to their high cost and complicated authentication schemes.

As a potentially powerful tool to combat rampant counterfeiting on the packaging, the on-dose authentication (ODA) measure used as "in-drug labelling" is introduced[5]. ODA enables verification of the end product as genuine and ODA labels are usually made from biocompatible or edible materials which are directly embedded into the end products themselves. Bio-based materials are a promising class of materials that are currently under-explored for ODA applications[6–9]. ODA technologies include Quick Response (QR) microtaggants[10], encoded-multifunctional hydrogel microparticles[7, 11–13], physically unclonable function (PUF) barcodes[14], 3D printed medicines[15, 16] and safety-oriented photolithography of edible pharmaceutical polymer films[17]. Compared to traditional authentication protocols, ODA labels are more robust and resilient. ODA labels themselves cannot be easily tampered with without damaging the integrity of the product and fabrication of ODA labels requires highly specialized equipment and skilled operators, both of which are not easily accessible to counterfeit syndicates. Scalable production of ODA labels is possible through micro-scale fabrication techniques based on microfluidics[7, 12, 13] and customizable codes embedded in ODA labels such as QR microtaggants[10] and encoded-multifunctional hydrogel microparticles[7] can be easily read using current smartphone technology. ODA labels can also be 3D printed at centimeter-scale[15] for easy authentication by the naked eye.

Despite these advantages, ODA labels are not widely implemented yet due to the difficulty in striking a balance between ease of verifying authenticity and cryptographic safety. To illustrate this point, let's take the example of physical unclonable function (PUF) barcode[14]. The PUF barcodes provide very high cryptographic safety yet accessing the stored information is not straightforward. Only a cryptographic key can read these ODAs under a series of light illuminations with various excitation wavelengths. Consequently, the information in PUFs described by Leem et al. [14] can only be authenticated with

dedicated lab equipment not available readily to end users. The need for dedicated lab equipment increases the cost of PUF ODA limiting their utilization in low-cost products. On the other end of the spectrum, ODA measures produced by flow lithography[7] utilize the shape of the barcode to store information, and cell phones can be used for authenticity verification. In other words, they are easier to produce and authenticate yet they do not provide the high level of cryptographic safety PUFs provide. Ideal ODA should be not only easy to read but also it should provide a high level of cryptographic safety. In this sense, a dual-authentication ODA label utilizing both optical and magnetic verification is a step in the right direction.

In this study, magnetic ODA labels made of hydrogel microparticles with superparamagnetic colloids embedded at prescribed positions were synthesized using a microfluidic approach. This approach parleys stop-flow lithography (SFL)[18] with virtual magnetic moulds (VMMs)[19] made of magnetically activated nickel patches. The pattern of Ni patches collectively denotes a binary code. The embedding efficiency was optimized through a combination of analytical scaling arguments and finite element simulations. The resulting hydrogel microparticles can effectively function as magnetic ODA labels with dual authentication (optical and magnetic) providing additional cryptographic security than the previously proposed hydrogel microparticles[7] offering only optical authentication.

2.2 Materials and methods

2.2.1 Hydrogel microparticle synthesis

Materials 2-Hydroxy-2-methy-lpropiophenone (CAS No. 7473-98-5), Poly(ethylene glycol) diacrylate (average Mn 700), and grids for transmission electron microscopy (grid size 400 mesh × 62 μm pitch, nickel) were purchased from Sigma-Aldrich. Cinnamon Cassia oil (CAS No. 8007-80-5) was purchased from Aromaolie Ki-Line VOF. Sigma-Aldrich Sylgard 184 silicone elastomer kit was purchased from Dow Corning. All the SPCs (S2451, S2180, AR488 and S246) with saturation magnetization values in the range from 15~ 25 Am^2/kg were purchased from MicroParticles GmbH, the densities of the colloids are 1.79, 1.62, 1.49 and 1.51 g/cm^3 while the diameters are 1.43, 3.90, 4.54 and 10.3 μm respectively. The SPC consists of a core made of polystyrene with iron oxide particles incorporated inside the polystyrene. The core is covered by a carboxyl group polymer shell with a thickness of 100-500 nm to prevent any leakage of the iron oxide particles to the surrounding medium. For easier observation, fluorescent dyes were also functionalized in the shell. The shell thickness is ignored in the calculations and simulations.

Fabrication of magnetic moulds Nickel patches are deposited on a thin glass slide via e-beam deposition of nickel on a lithographically patterned surface. The protocol was similar to the literature[19]: followed by standard photolithography, after dissolving the exposed photoresist regions, a thin nickel layer was deposited by electron beam evaporation and the sacrificial layer was removed subsequently. The patterns of the Ni patches were controlled by the lithography mask. Despite that the ready patch was 200 nm thick due to the experimental constraint, it showed good magnetic interaction with the colloids.

Preparation of the microfluidic channel Polydimethylsiloxane (PDMS) microfluidic devices were fabricated in a similar way as described in the literature[7]. A single straight channel design that is 35 μm in height, 1 cm in length and 500 μm in width was used since no complicated fluid was involved. After puncturing one 0.3 mm hole on each end of the channel using a biopsy needle, the devices were attached to the magnetic patches slide with a thin layer of spin-coated and semicured (65 °C, 30 min, ratio base: curing agent= 10:1 wt%) PDMS layer. The whole device was then cured at 65 °C overnight. The ready device was around 2 mm in thickness and 10 mm by 10 mm in width and length.

Injected suspension The injected suspension is a mixture of photo-initiator (2-hydroxy-2-methylpropiophenone) with PEGDA-700 at a proportion 1:20 vol% and without any magnetic content tuned to assure the edibility. To get a homogeneous distribution of the SPCs, the suspension was vortexed and placed in a sonication bath for 30 minutes at room temperature.

Microparticle synthesis The SFL setup was modified from the literature[7]. As depicted in Figure 2.1(a), the microfluidic device was set with the Ni patch at the bottom and placed on a microscope (Nikon Ti-E inverted) which was equipped with a motorized stage. The inlet was connected to the remotely controlled air pump (0.5 psi) and the outlet to the collecting Eppendorf tube via silicone tubes. Andor CCD camera was hooked to the microscope to record the real-time tracking of the magnetic colloids' behavior. The external magnetic field was provided by an axially magnetized permanent neodymium magnet (Terramag H-N 40/150 Permanent magnet Ring NdFeB) with a residual magnetism of 1.26 T. The ring shape made sure that it could be placed around the objective under the channel.

2.2.2 Finite element simulations

In COMSOL setup, the No Currents (mfnc) module was used alongside the finite elements method. The Ni patches ($\mu_r = 600$) are placed inside an air sphere ($\mu_r = 1$) which is 4 times larger than the Ni patches in diameter. Outside the air sphere, there is a second air

shell in 5 μm thickness, which is defined as the layer for the finite element method. The homogeneous external magnetic field ($H = 100 KA m^{-1} = 0.1245 T$) is set perpendicular to the Ni patches. A zero magnetic scalar potential (ΔV_m)is set at the bottom below the Ni patches. The constitutive relation applied is shown in Equation (2.1) and the reduced H-field is expressed as Equation (2.2) where H_b is the background magnetic field.

$$\nabla \cdot \vec{B} = \nabla \cdot (\mu_0 \mu_r \vec{H}) = 0 \tag{2.1}$$

$$\vec{H} = -\nabla V_m + \vec{H}_b \tag{2.2}$$

The microgradient $|\vec{H}| \frac{\partial |\vec{H}|}{\partial z}$ induced by Ni patches of different geometries, sizes, and arrangements are investigated in COMSOL. Lines and slices were cut along z-axis when assessing the scenario in Figure 2.2(b) while the x-axis for Figure 2.2(c). ImageJ was applied where a measurement of the effective magnetostatic force height is needed.

We assumed that the microchannel would be around 20 μm, and most of the colloids would flow through the middle of the microchannel due to Hagen-Poiseuille flow. As such, the value of the $|\vec{H}| \frac{\partial |\vec{H}|}{\partial z}$ in the numerical study is all obtained from the cutlines at a height of 10 μm above the Ni patch (as schematically shown in Figure A.S7) unless otherwise stated.

2.3 Results and discussion

2.3.1 Hydrogel microparticle synthesis strategy

The four steps to synthesize hydrogel microparticles are depicted in Figure 2.1(a, b). Firstly, a suspension containing UV-responsive oligomer (PEGDA), a photoinitiator, and SPCs are pumped into the channel (illustrated in Figure 2.1b as *Fill* step). SPCs are initially scattered randomly due to Brownian motion (Figure A.S1). After the channel is filled, flow is stopped and an external magnetic field is imposed using a ring-shaped permanent magnet. SPCs move towards the Ni patches and are assembled into a pattern dictated by the VMMs as shown in Figure 2.1(b) as *Trap* step. Next, a beam of UV light is passed through a mask to trigger photo-polymerization in the geometry dictated by the mask in *Photo-polymerize* step. After synthesis is completed, the channel is purged and the microparticles are collected in *Purge* step. The microparticles can be synthesized in batch mode by keeping the suspension in the channel stagnant while the microscope objective is moved along the channel using an automated stage[7, 20] or they can be synthesized in continuous mode commonly referred to as stop flow lithography[18, 21]. When the continuous mode is desired, the suspension continuously flows into the channel via

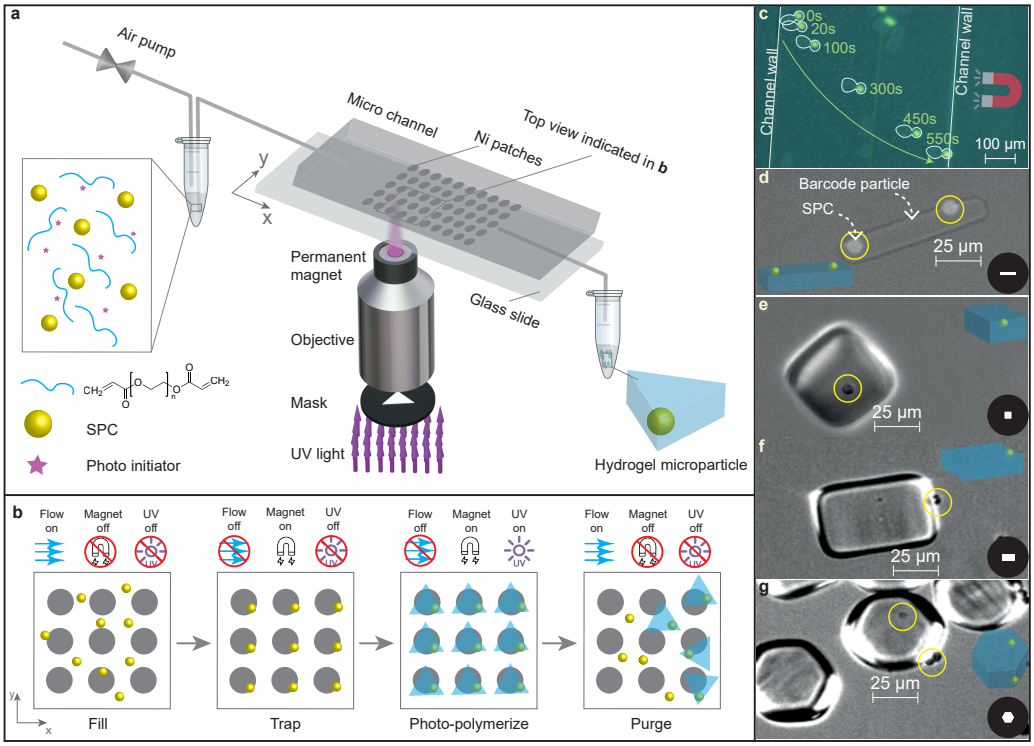

Figure 2.1: Scheme of the hydrogel microparticles synthesis. (a) Solution containing polymer (PEGDA), photoinitiator, and superparamagnetic colloids(SPCs) are pumped through a microfluidic channel. The VMMs placed on the bottom of the channel are magnetized on-demand to trap SPCs. UV light passing through a mask placed at the field stop of the microscope crosslinks the PEGDA to trap SPCs are designated positions. (b) Illustration of four steps involved in synthesis from the top view. (c) hydrogel microparticles respond to the external magnetic field and move from one channel wall to the other when a permanent magnet is brought in contact. Extracted from movie A.S1. (d-g), which can be accessed by scanning the QR code provided in the Appendix. The microscopy pictures of microparticles of different shapes with SPCs placed at designated positions. Their scale bars are all 25 µm. The mask used in synthesis of each particle is given along with a 3D illustration of the microparticle with embedded SPC.

a pressure-regulated air pump while the synthesis of microparticles is realized through a series of photo-polymerization and magnetic trapping steps repeated. The canonical process flow is outlined in Figure 2.1(b): Step I. Fill: pressure on, magnet off, shutter closed - 1 s; Step II. Trap: pressure off, magnet on, shutter closed - 1 s; Step III. Photo-polymerize: pressure off, magnet on, shutter on– 0.5 s. Step IV. Purge: pressure on, magnet off, shutter closed - 1 s.

The shape of the microparticle is controlled by the mask used during photo-polymerization, while the pattern of the SPCs is dictated by the lithographically deposited pattern of the VMMs. Microparticles of various shapes with SPCs embedded at designated positions were produced (strips, squares, rectangles, and hexagons) and are presented in Figure 2.1(d to g). The top and bottom insets show the 3D illustration of the microparticle with embedded SPCs and the mask respectively. We note that SPCs were successfully embedded regardless of microparticle shapes and were responsive to an external magnetic field (see Figure 2.1(c) and corresponding movie A.S1, which can be accessed by scanning the QR code provided in the Appendix). We envision that the response of synthesized microparticles towards an external field illustrated in Figure 2.1(c) may be utilized to first collect microparticles dispersed in a liquid formulation and then to check for authenticity by decoding the binary code. Moreover, the existence of magnetic response as illustrated in Figure 2.1(c) may be interpreted as the first step of a dual-authentication process followed by optical authentication as illustrated by Rehor et al. [7].

The incorporation of VMMs [19] in SFL technology[22] affords several advantages. Firstly, magnetic assembly of materials is contactless which is highly desirable in the manufacture of edible ODA labels and particles[6, 9, 11, 23, 24]. Secondly, the fidelity of assembling materials using magnetic moulds is shown to be as high as 97%[19] which is promising for applications requiring high encoding accuracy and capacity. Thirdly, the production of nickel patches acting as VMMs requires highly precise techniques such as electron beam deposition which is not easily accessible and hence serves as a technological barrier to counterfeiting operations. Fourthly, precise and highly customizable ODA labels[25–30] can be mass-produced via SFL[18, 31]. Leveraging both optical and magnetic authentication schemes, a higher level of cryptographic safety can be achieved in a single scheme[7].

Other methods such as 3D printing[32], micro-engraving[5, 33], 2-photon lithography[34] have also been considered from resolution and regulatory compliance point of view for the synthesis of proposed microparticles. 3D printing has seen considerable interest in literature as certain drug excipients in molten form or as a viscous formulation can be extruded, providing an easy route to commercialization with minimal regulatory hindrance. However, for most of the 3D printer types, the feature resolution depends highly on the designed geometry and print orientation and usually larger than 10 µm. The same resolution issue is also relevant in micro-engraving. 2-photon lithography offers nanome-

ter resolution yet this comes at the expense of very slow operation. Beyond resolution issues, all these methods are not continuous forcing us to choose stop-lithography as the ideal manufacturing method for this study.

Since magnetic microparticles are proposed for labeling pharmaceuticals, the biosafety and cytotoxicity of the ingredients are essential to evaluate. Polyethylene glycol (PEG) is commonly used as an excipient in pharmaceutical formulations and it is approved for clinical use by the Food and Drug Administration(FDA) due to its acceptable biosafety[35]. Iron oxide nanoparticles are found to be biocompatible and stable in aqueous solutions. Due to this nature, iron oxide nanoparticles have been employed for multiple clinical applications[36]. The trace of polystyrene in the SPC is deemed acceptable if the daily intake is less than 1.5 mg[12]. The only biosafety concern is the fluorescent dye adopted in the SPC. However, the fluorescent dye is utilized for visualization purposes in this study and can be removed in real-life applications since the barcode decoding can be performed by visible light microscopy. Therefore, we generally consider the proposed magnetic microparticles biosafe. Moreover, the photo-polymerized PEG hydrogels have been widely used in cell encapsulation[37] and tissue engineering fields[38]. Therefore, it is possible to find many equivalent hydrogel materials[7, 30, 39, 40] for the purpose of this work when the cytotoxicity of PEGDA is considered of ultimate importance in some application fields.

In addition to the cytotoxicity, another concern for the real-world application is the deformation of PEG hydrogel microparticles upon exposure to high humidity conditions. Due to its hygroscopic nature, microparticles may swell and deform anisotropically resulting in deformation of the code. Thankfully, the swelling ratio of PEG hydrogels can be adjusted by crosslink density via manipulating the monomer molecular weight, initiator concentration, irradiation time, and light intensity[41, 42]. Moreover, the PEG hydrogel coding can be made in a way that after homogeneous swelling the code reads the same. Here we will not explore this large parameter space in this study. However, it should be noted that the durability of the microparticles should be optimized to minimize deformations in proposed microparticles taking into account the exact storage conditions of the product. Furthermore, superparamagnetic iron oxide nanoparticles are widely applied for electromagnetic interference shielding[43, 44], therefore there is concern that our composite particles might have decreased durability due to the electromagnetic Interference pollution. However, our binarycode only is exposed to a magnetic field produced by a permanent magnet when authenticated. The dose and duration of exposure are relatively trivial. Therefore, in this study, the durability of binarycode in the presence of electromagnetic interference pollution is not further explored.

2.3.2 Optimization of trapping efficiency

Despite its promise, there are two major issues with the proposed microparticle manufacturing process. The first issue is the long time duration required to trap for SPCs on VMMs (referred to as trapping time). Our experiments showed that trapping time could be as long as a few minutes (Supplementary movie A.S4, which can be accessed by scanning the QR code provided in the Appendix) which is far from our desire of a few seconds. The second issue is authentication failure due to the incorrect placement of SPCs on VMMs. SPCs have to be trapped in the specific configuration outlined by the magnetic moulds so that the binary code can be decoded successfully. However, as depicted in Figure 2.3(a), some SPCs (highlighted in red) are deposited in the voids between Ni patches, or no SPCs are trapped on some patches (highlighted in blue). A simple solution to address the issue of SPCs sedimenting in the voids might be to decrease the distance between VMMs. Yet this solution is not practical as the photolithography step is less reliable when distances are less than one micron. One may also rationalize that increasing the concentration of SPCs will result in fewer unoccupied VMMs yet high volume fractions might cause aggregation/chaining of SPCs under the magnetic force and further exacerbate reading failure due to SPCs sedimenting at voids. At the same time, to ensure the edibility of this ODA code, we limit the selection of raw materials to the generally recognized as safe (GRAS) list. For instance, magnetic susceptibility tuning agents, commonly used in magnetic trapping[19] are intentionally avoided due to their toxicity. To address these issues, a better understanding of the forces acting on the colloids in the presence of magnetic field gradients induced by VMMs is crucial. Therefore, we explored two scenarios as represented in Figure 2.2(a) and Figure 2.3(b) and will discuss them in the following sections.

2.3.2.1 *Force balance in Scenario A: Optimizing the magnetic microgradient along z for trapping time*

As schematized in Figure 2.2(a), Scenario A assumes a SPC is sedimenting from a certain height above the Ni patch center through a liquid. As a results, it will experience magnetic force ($\vec{F_m}$), hydrodynamic drag force ($\vec{F_d}$), buoyancy ($\vec{F_b}$) and gravitational force ($\vec{F_g}$).

We first investigate the magnetic force, which depends on the Ni patch and SPC size, in combination with the position of SPC relative to patch. Specifically, we look at the vertical (z) component of this force along z axis in our calculation of the trapping time. Using the magnetic force as in [19], we find that its vertical component $F_{m,z}$ is given by

$$F_{m,z} = 4\pi r^3 \mu_0 \frac{\chi_{part} - \chi_{sol}}{\chi_{part} + 2\chi_{sol} + 3} |\vec{H}| \frac{\partial |\vec{H}|}{\partial (z)} \tag{2.3}$$

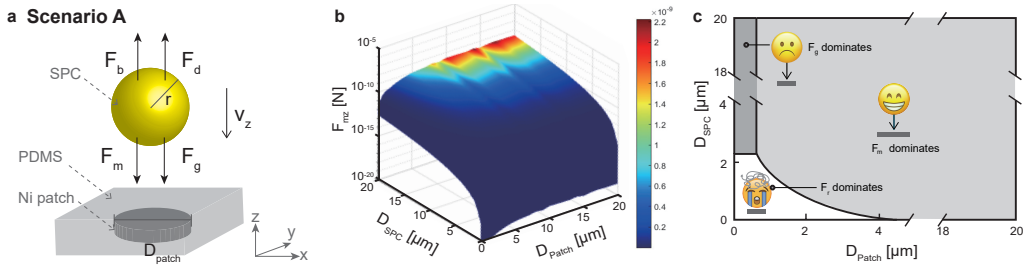

Figure 2.2: Analysis of forces acting on SPC based on Scenario A. (a) Scenario A: SPC sedimenting above a Ni patch and the forces acting on the SPC are illustrated; (b) The magnetostatic force, $F_{m,z}$ exerted on the SPC due to magnetic field gradient created by the Ni patch, obtained through Equation (2.3); (c) The phase map of the dominating force.

in which r is the radius of the SPC, μ_0 is the magnetic permeability of free space, χ_{part} and χ_{sol} are the magnetic susceptibility of SPC and the solution. Here μ_0, χ_{part} and χ_{sol} are constant. The microgradient $|\vec{H}|\frac{\partial|\vec{H}|}{\partial z}$ is directly proportional to the magnitude of the magnetic force, which depends on the magnetic field strength $H = |\vec{H}|$ and its gradient along the vertical (z) axis.

We use the COMSOL Multiphysics package as a finite element analysis tool to calculate the vertical magnetic force $F_{m,z}$ acting on a SPC placed at a canonical height of 10 μm above a single circular Ni patch for a various combinations of D_{SPC} and D_{patch}, as shown in Figure 2.2(b). The depicted range of D_{SPC} and D_{patch} is chosen to represent the relevant experimental values in this study. The canonical height of 10 μm is chosen as the channel height is 35 μm and SPC sizes range from 1.43 to 10.3 μm (described in the Numerical and experimental setup section). As seen in Figure 2.2(b), the colloid will experience a stronger magnetic force if it sediments onto a larger D_{patch}. This is further demonstrated in Figure A.S3: A larger Ni patch is able to produce a stronger microgradient hence a larger magnetic force. Similarly, the size of D_{SPC} also exhibits a positive correlation because a larger volume SPC interacts stronger with the magnetic field in comparison to a smaller one.

Using $F_{m,z}$ calculated for various D_{SPC} and D_{patch} values, we can compare the magnitude of all possible forces acting on the SPC in Scenario A and identify the dominating force for the SPC sedimentation. The magnitude of all the other forces, i.e. the hydrody-

namic drag force (F_d), buoyancy (F_b), gravitational force (F_g), and apparent Brownian force (F_r), is represented by

$$\begin{aligned} F_b &= \rho_l g \frac{4\pi}{3} r^3 \\ F_d &= 6\pi\nu\mu r \\ F_g &= \rho_p g \frac{4\pi}{3} r^3 \\ F_r &= \zeta m_p \sqrt{\frac{216 k_b}{\pi(\frac{\rho_p}{\rho_l})^2 C_{Cun}}} \sqrt{\frac{\eta_f T}{\rho_l d^5 \Delta t}} \end{aligned} \tag{2.4}$$

in which ρ_p and ρ_l represent the densities of the SPC and the surrounding liquid respectively, ζ represents the Gaussian random number with zero mean and unit variance, m_p is the mass of the SPC, k_b is the Boltzmann constant, η_f the kinematic viscosity of the fluid surrounding the SPC. The Cunningham correction factor, C_{Cun}, accounts for the non-continuum effects of the drag force. As the Reynolds number Re is much smaller than unity in this study, the drag force is best described by Stokes' law. Here, the magnitude of the Brownian force (F_r) results from a dimensionless scaling analysis[45].

In Figure 2.2(c), effective gravitational force, $F_g - F_b$, and Brownian force F_r are calculated and compared to F_m. The dominating force is identified in a parameter space of patch and colloid size. The region Brownian force is dominant in the parameter range where $F_r/F_m > 1 \cap F_r/(F_g - F_b) > 1$ highlighted in white (F_r dominates). In this part of the parameter space, the SPC will not be easily trapped as the Brownian force dominates and randomizes the SPC motion counteracting trapping. The dark grey section of the parameter space (F_g dominates) corresponds to a region where gravitational force dominates ($(F_g - F_b)/F_m > 1 \cap (F_g - F_b)/F_r > 1$) hence the SPC will sediment on the patch under the gravitational pull. The light grey region (F_m dominates) illustrates the parameter space where $F_m/F_r > 1 \cap F_m/(F_g - F_b) > 1$. In this region, F_m is larger than both the Brownian force and the gravitational force, therefore the SPCs are expected to get trapped by the patch. This parameter phase diagram provides an overview of which forces dominate fin the parameter space spanning D_{patch} and D_{void}. We found out that small Ni patches ($D_{patch} \leqslant\sim 0.67\ \mu m$) only induce weak F_m and therefore lead to the fact that the gravitational force $F_g - F_b$ dominates when $D_{SPC} \geqslant 2.2\mu m$. When the SPC is smaller than 2.2 μm the Brownian force, F_r, will dominate and complicate trapping. When $D_{patch} \geqslant\sim 4\mu m$, the magnetic force will always prevail regardless of the size of SPC.

We found that the size of the Ni patch influences the maximal height above the surface that magnetic forces reach while the shape of the patch remains insignificant. Figure A.S4 in the Appendix shows the sediment action speed for several practical D_{SPC} used in our experiments. The micrograd ients profiles of the magnetic field along the full x-z plane

are numerically evaluated in Figure A.S3 in the Appendix. From these profiles, we found that the diameter of the Ni patch determines the maximal elevation that the magnetic force can reach, and thus 'pull in' particles. Besides the patch size, various patch geometries are also numerically evaluated in Figure A.S5 and S6. These results emphasize that varying the patch geometry only has a minor effect on the resulting vertical magnetic force. For completeness, we show the SPC trajectory rebuilt using Particle tracking velocimetry in a microfluidic channel with various D_{patch} in Figure A.S10 in the Appendix. These observations have good agreement with the dominating force analysis.

2.3.2.2 *Force balance in Scenario B: Optimization of the magnetic microgradient along x direction for trapping ratio*

We proceed by considering a particle that happens to settle in the interstitial space between adjacent Ni patches. In this scenario, the SPC needs to move along x-axis to approach the Ni patches to get trapped, as illustrated in Figure 2.3(b). Consequently, we focus on the horizontal x microgradient of the magnetic field and consider the horizontal component of the magnetic force

$$F_{m,x} = 4\pi r^3 \mu_0 \frac{\chi_{part} - \chi_{sol}}{\chi_{part} + 2\chi_{sol} + 3} |\vec{H}| \frac{\partial |\vec{H}|}{\partial (x)} \tag{2.5}$$

To build a working understanding of the forces involved in scenario B, we investigate numerically how the distance between patches, D_{void}, influences magnetic microgradients for a fixed patch diameter D_{patch} in COMSOL. For the finite element calculations, three Ni patches are arranged with different "patch to void" ratios, i.e., $D_{void} : D_{patch} = 0.5$, 1, 2, and 3 respectively whereas D_{patch} is canonically fixed as 5 μm. Here we choose a cutline at 4 μm high above the Ni patches (depicted in Figure A.S7 in the Appendix) to elaborate the horizontal microgradient because 4 μm is able to compensate for the thickness of Polydimethylsiloxane (PDMS) layer (around 1 μm) and the size of SPC. The results are shown in Figure 2.3(c). The minimal horizontal microgradient value is chosen as 10^{12} A^2/m^3, corresponding to an effective force that makes that trapping occur within experimentally reachable time spans. This cut-off value is plotted as a grey dashed line. A more detailed contour plot for the microgradients in the xz-plane can be found in Figure A.S8 in the Appendix.

As seen from Figure 2.3(c1) and (c2), for small $D_{void} : D_{patch}$ value, i.e. 0.5 and 1 exhibit similar "seagull" profiles. The microgradient reaches its maximum value at the edge of the patches and gently descends as leaving the edge. The microgradient value is always above the minimum value of 10^{12} A^2/m^3 . Consequently, the SPCs will move towards the patches and will be trapped. Interestingly, the $D_{void} : D_{patch}$ =0.5 array induces a smaller microgradient in the patch center as highlighted in green. It appears that the

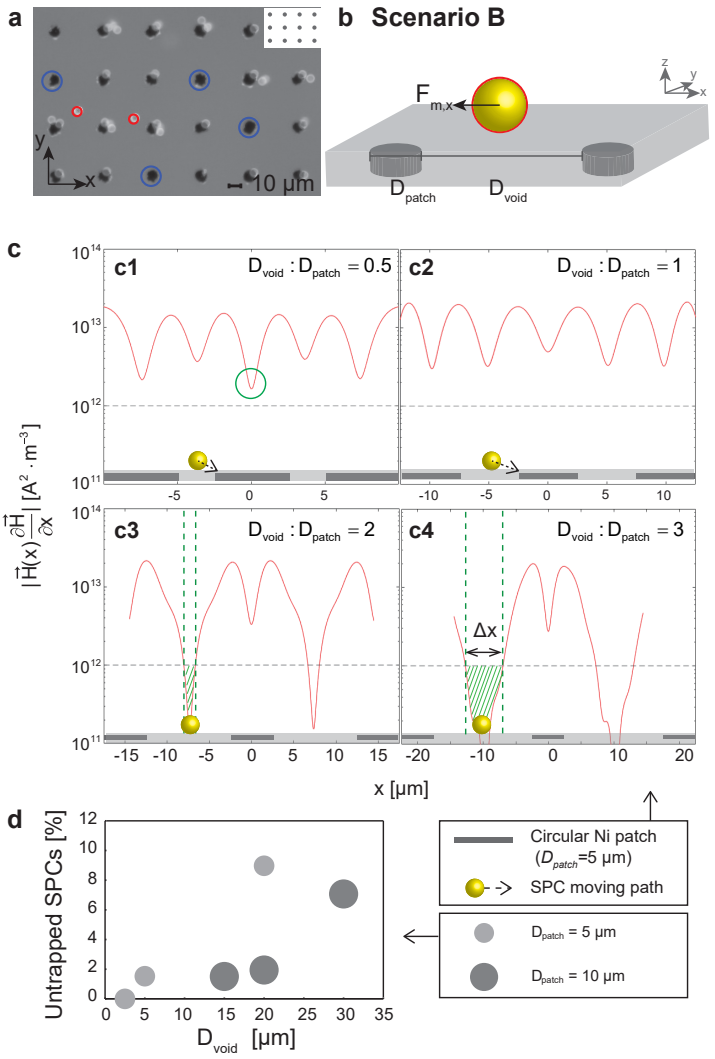

Figure 2.3: (a) Micrograph illustrating the challenges in defining optimal experimental parameters for high fidelity trapping of SPCs. SPCs (10 vol%, diameter=4.54 µm) are trapped by circular Ni patches ($D_{patch} = 10\mu m$, $D_{void} = 30\mu m$) in the presence of an external magnetic field. The insert shows the pattern of the Ni patches used. Two failure events are highlighted (i) SPCs that can be not trapped by Ni patches highlighted by red circles and (ii) empty patches where no SPC is trapped highlighted in blue. (b) Scenario B: SPC settles between Ni patches; (c) The horizontal micrograidents $|\vec{H}|\frac{\partial \vec{H}}{\partial x}$ induced by Ni patch array of various voids as a function of position. The diameter of the patches D_{patch} is 5 µm while the distance of two adjacent Ni patches, D_{void}, are (c1) 2.5 µm; (c2) 5 µm; (c3) 10 µm; (c4) 15 µm. Three circular Ni patches are placed on z= 0 µm as indicated by the grey blocks. The data are obtained from the cutlines at a height of 4 µm above Ni patches which is schematized in Figure A.S7 in the Appendix. The grey dashed line indicates the minimal value (10^{12} A^2m^{-3}) needed for trapping the SPC. (d) The percentage of untrapped SPCs (D_{SPC}=4.54 µm) under the conditions of various D_{patch} and D_{void} combinations.

closely packed virtual moulds act as a single virtual mould because the magnetic dipoles cancel each other out in the center and yield a lower micrograd ient[46]. This observation is further clarified in Figure A.S9 in the Appendix.

While small $D_{void} : D_{patch}$ is not so ideal, larger ratios are not desirable at all. In Figure 2.3(c3) and (c4) corresponding to $D_{void} : D_{patch}$=2 and 3, the horizontal microgradients exhibit "cliff" profiles. The microgradient still reaches its maximum value at the patch edge but it precipitously goes below 10^{11} A^2/m^3 when moving to the interstitial spacing. As it falls below the grey line, a "dead zone" as indicated by the green shadow shows up. In Figure 2.3(c4), the distance of this "dead zone" Δx is around 5.8 μm. When Δx is larger than the SPC itself, a failure of trapping and consequently a higher untrapped ratio is foreseen. Note that in Figure 2.3(c), the value of the valleys is supposed to be zero, which is smoothed by the mesh size and the steep gradient around it. Despite that, we consider the results reasonable because the forced objects are full spheres instead of point objects in reality.

To check the validity of trends observed in finite element calculations, a set of trapping experiments were run and the ratios of untrapped beads relative to total SPCs injected under two different D_{patch} with various D_{void} is presented in Figure 2.3(d). For these analyses, the number of untrapped SPCs and the total number of SPCs injected were followed and counted with the OpenCV package in Python. It can be seen that the percentage of untrapped beads increases from 0% to 9% for an increasing D_{void}, while the D_{patch} is set constant at 5 μm. A similar increase occurs from 1% to 7% for $D_{patch} = 10$ μm for an increasing D_{void} size. These experimental results are in good agreement with the numerical analysis.

2.3.2.3 *Washing of the untrapped sedimented SPCs*

From the discussions above, it is concluded that there is a delicate balance between the SPC size, patch size, patch distance, and microchannel height which has to be considered in order to achieve SPC assembly over the VMMs within a reasonable time. However, a large patch distance is always necessary in order to realize a blank position in the binary code. This unfortunately will break this delicate balance. Such a dilemma is demonstrated in Figure 2.4(a1) using 2 sets of patch arrays that can be decoded into "TUD" (Technical University of Delft) and "ETH" (Swiss Federal Institute of Technology). In these arrays, the patch represents for bit "1" and void for "0". Each row is composed of 8 bits and represents a letter. Unfortunately, only the letter "U" (01010101, see Figure 2.4(b)) possesses the desirable arrangement,i.e., $D_{void} : D_{patch}$=1 but the other letters are not ideally arranged. Consequently, we would foresee a high untrapped ratio with such an array according to the previous finite element analysis study.

To further improve our trapping efficiency, we incorporate a washing step into our protocol. To be more explicit, we use a polymer solution with no SPCs from a different inlet

to wash away the untrapped SPCs over the voids while keeping the magnetic field on. This extra step takes place between the *Trap* step and the *Photo-polymerize* and is programmed as: pressure on, magnet on, shutter closed. A demonstration of this step is shown in Supplementary Movie A.S2, which can be accessed by scanning the QR code provided in the Appendix, and a set of images extracted is illustrated in Figure 2.4(a2-a4). When the washing step started, i.e., 0s in Figure 2.4(a2), there was only one valid binary code as labeled by a checkmark. Along with the polymer solution flow, the untrapped SPCs were flushed through the channel and were trapped by the magnetic active patches that they passed by. In this way, the code efficiency increased from 25% at 0s (Figure 2.4(a2)) to 50% at 185s (Figure 2.4(a3)), thus the fidelity of complex binary codes was improved. By increasing the washing time further, the number and the exact position of the SPCs may change from run to run but we can reproducibly incorporate the intended code to microparticles and decode the incorporated code. Finally, we have achieved 100% code efficiency at 245s with an optimized initial SPC concentration (Figure 2.4(a4)).

In Figure 2.4(b), we illustrate the optical decoding method: First, the microscope image of the binary code is captured as highlighted in yellow. The image is meshed to 3 by 8 individual code regions. Following that, the SPC in the individual area is identified and the value is attributed to a binary code. No matter how the morphology of the SPC aggregates in each mesh is, the code is read as *1* if there are any SPCs in this area or *0* otherwise.

2.4 Conclusion

We present a microfluidic synthesis method for producing PEGDA microparticles with SPCs embedded at designated positions combining virtual magnetic moulds with stop-flow lithography. The hydrogel microparticles may function as an on-dose anti-counterfeiting measure for food and medicine. The embedded SPCs collectively act as a binary code matrix that can be read optically while their superparamagnetic nature makes the microparticles responsive to the magnetic field. However, we encountered undesired scenarios such as untrapped SPCs settling in interstitial gaps of our Ni patches, as well as excessive trapping times. These scenarios result in unreliable encoding and reading of the binary code as well as unacceptably long production times. To overcome these experimental challenges, a combined scaling argument and finite element study were conducted. We identified $D_{void} : D_{patch}$=1 as the optimum experimental parameter to get a high trapping efficiency. Smaller or larger spacing will lead to a decline of magnetostatic force at the void and result in untrapped SPCs. To rule out such undesired scenarios, we proposed a washing strategy that has proven to compensate the undesired $D_{void} : D_{patch}$ ratio in the binary code. The proposed magnetic microparticles may inspire the development of quality control, tracking, and anti-counterfeiting technologies in order to combat increasing counterfeiting crime. Besides that, this approach successfully assembles SPCs into

anisotropic patterns and traps them in a hydrogel matrix with desired 3D geometry, showing potential for synthesis of magnetically responsive structures such as microswimmers, micro self-propellers, and soft microrobots.

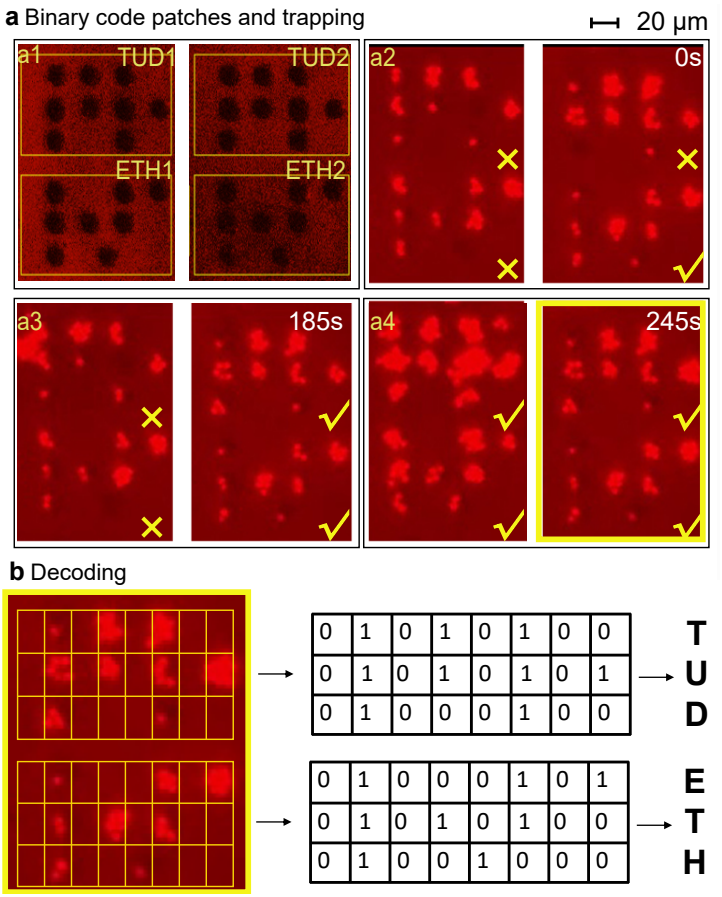

Figure 2.4: A demonstration of the wash strategy and decoding method. (a) The Ni patches design which composed of binary-codes corresponding to the abbreviation of institutes collaborating in this study "TUD" for the Technical University of Delft and "ETH" for the Swiss Federal Institute of Technology in Zürich. More effective binary codes were formed as the washing step went on. (b) Illustration of the decoding process: The decoding method involves 3 steps. Step 1: read the barcode under microscope. Step 2: mesh the output image and identify the SPCs in each mesh, assign *1* to the matrix when SPC is detected and *0* otherwise. Step 3: translate the ASCII code into text.

REFERENCES

[1] W. H. Organization. *A study on the public health and socioeconomic impact of substandard and falsified medical products*. Tech. rep. 2017.

[2] S. M. Beargie et al. "The economic impact of substandard and falsified antimalarial medications in Nigeria." *PloS one* 14.8 (2019), e0217910.

[3] R. Shah, P. Prajapati, and Y. Agrawal. "Anticounterfeit packaging technologies." *Journal of advanced pharmaceutical technology & research* 1 (2010), pp. 368–73.

[4] M. Puddu, D. Paunescu, W. J. Stark, and R. N. Grass. "Magnetically recoverable, thermostable, hydrophobic DNA/silica encapsulates and their application as invisible oil tags." *ACS nano* 8.3 (2014), pp. 2677–2685.

[5] H. Zhang et al. "Materials and technologies to combat counterfeiting of pharmaceuticals: current and future problem tackling." *Advanced Materials* 32.11 (2020), p. 1905486.

[6] H. B. Eral et al. "Governing principles of alginate microparticle synthesis with centrifugal forces." *Langmuir* 32.28 (2016), pp. 7198–7209.

[7] I. Rehor et al. "Biodegradable Microparticles for Simultaneous Detection of Counterfeit and Deteriorated Edible Products." *Small* 13.39 (2017), p. 1701804.

[8] Y. N. Vakkipurath Kodakkadan et al. "Arbitrarily-shaped microgels composed of chemically unmodified biopolymers." *Biomater. Sci.* 8 (11 2020), pp. 3044–3051.

[9] C. C. Schuurmans et al. "Complex coacervation-based loading and tunable release of a cationic protein from monodisperse glycosaminoglycan microgels." *Soft Matter* 14.30 (2018), pp. 6327–6341.

[10] S. Han et al. "Lithographically Encoded Polymer Microtaggant Using High-Capacity and Error-Correctable QR Code for Anti-Counterfeiting of Drugs." *Advanced Materials* 24.44 (2012), pp. 5924–5929.

[11] Y. C. Saraswat et al. "Shape anisotropic colloidal particle fabrication using 2-photon polymerization." *Journal of colloid and interface science* 564 (2020), pp. 43–51.

[12] G. Tang et al. "Faithful fabrication of biocompatible multicompartmental memomicrospheres for digitally color-tunable barcoding." *Small* 16.24 (2020), p. 1907586.

[13] G. Tang et al. "Gas-shearing fabrication of multicompartmental microspheres: a one-step and oil-free approach." *Advanced Science* 6.9 (2019), p. 1802342.

[14] J. W. Leem et al. "Edible unclonable functions." *Nature Communications* 11.1 (2020), p. 328.

[15] S. J. Trenfield et al. "Track-and-trace: Novel anti-counterfeit measures for 3D printed personalized drug products using smart material inks." *International Journal of Pharmaceutics* 567 (2019), p. 118443.

[16] Z. Grof and F. Štěpánek. "Artificial intelligence based design of 3D-printed tablets for personalised medicine." *Computers & Chemical Engineering* 154 (2021), p. 107492.

[17] S. Takei. "Safety-oriented photolithography of water-soluble resist using water-coating and water-developable processes for edible pharmaceutical polymer films." *Applied Physics Express* 11.8 (2018), p. 086501.

[18] D. Dendukuri, S. S. Gu, D. C. Pregibon, T. A. Hatton, and P. S. Doyle. "Stop-flow lithography in a microfluidic device." *Lab on a Chip* 7.7 (2007), pp. 818–828.

[19] A. F. Demirörs, P. P. Pillai, B. Kowalczyk, and B. A. Grzybowski. "Colloidal assembly directed by virtual magnetic moulds." *Nature* 503 (2013), p. 99.

[20] R. N. Georgiev et al. "Universal motion of mirror-symmetric microparticles in confined Stokes flow." *Proceedings of the National Academy of Sciences* 117.36 (2020), pp. 21865–21872.

[21] H. Z. An, E. R. Safai, H. B. Eral, and P. S. Doyle. "Synthesis of biomimetic oxygen-carrying compartmentalized microparticles using flow lithography." *Lab on a Chip* 13.24 (2013), pp. 4765–4774.

[22] D. Dendukuri, D. C. Pregibon, J. Collins, T. A. Hatton, and P. S. Doyle. "Continuous-flow lithography for high-throughput microparticle synthesis." *Nature materials* 5.5 (2006), pp. 365–369.

[23] H. Z. An, H. B. Eral, L. Chen, M. B. Chen, and P. S. Doyle. "Synthesis of colloidal microgels using oxygen-controlled flow lithography." *Soft Matter* 10.38 (2014), pp. 7595–7605.

[24] D. C. Pregibon, M. Toner, and P. S. Doyle. "Magnetically and Biologically Active Bead-Patterned Hydrogels." *Langmuir* 22.11 (2006). PMID: 16700603, pp. 5122–5128.

[25] J. Lee et al. "Universal process-inert encoding architecture for polymer microparticles." *Nature materials* 13.5 (2014), pp. 524–529.

[26] Y. Dou et al. "A review on self-assembly in microfluidic devices." *Journal of Micromechanics and Microengineering* 27.11 (2017), p. 113002.

[27] R. A. Hughes, E. Menumerov, and S. Neretina. "When lithography meets self-assembly: a review of recent advances in the directed assembly of complex metal nanostructures on planar and textured surfaces." *Nanotechnology* 28.28 (2017), p. 282002.

[28] L. Wang, S. Dong, and J. Hao. "Recent progress of magnetic surfactants: Self-assembly, properties and functions." *Current Opinion in Colloid & Interface Science* 35 (2018), pp. 81–90.

[29] Y. N. V. Kodakkadan et al. "Arbitrarily-shaped microgels composed of chemically unmodified biopolymers." *Biomaterials science* 8.11 (2020), pp. 3044–3051.

[30] I. Rehor et al. "Photoresponsive hydrogel microcrawlers exploit friction hysteresis to crawl by reciprocal actuation." *Soft robotics* 8.1 (2021), pp. 10–18.

[31] M. E. Helgeson, S. C. Chapin, and P. S. Doyle. "Hydrogel microparticles from lithographic processes: Novel materials for fundamental and applied colloid science." *Current opinion in colloid & interface science* 16.2 (2011), pp. 106–117.

[32] A. Kjar and Y. Huang. “Application of Micro-Scale 3D Printing in Pharmaceutics.” *Pharmaceutics* 11.8 (2019), p. 390.

[33] R. L. Jie Fei. “Drug-laden 3D biodegradable label using QR code for anti-counterfeiting of drugs.” *Materials Science and Engineering: C* 63 (2016), pp. 657–662.

[34] Y. C. Saraswat et al. “Shape anisotropic colloidal particle fabrication using 2-photon polymerization.” *Journal of Colloid and Interface Science* 564 (2020), pp. 43–51.

[35] P. Xue, X. Zhang, Y. J. Chuah, Y. Wu, and Y. Kang. “Flexible PEGDA-based microneedle patches with detachable PVP–CD arrowheads for transdermal drug delivery.” *RSC Advances* 5.92 (2015), pp. 75204–75209.

[36] D.-E. Coricovac et al. “Biocompatible colloidal suspensions based on magnetic iron oxide nanoparticles: synthesis, characterization and toxicological profile.” *Frontiers in Pharmacology* 8 (2017), p. 154.

[37] P. Panda et al. “Stop-flow lithography to generate cell-laden microgel particles.” *Lab Chip* 8 (7 2008), pp. 1056–1061.

[38] A. Sun et al. “Current research progress of photopolymerized hydrogels in tissue engineering.” *Chinese Chemical Letters* 32.7 (2021), pp. 2117–2126.

[39] H. B. Eral et al. “Governing Principles of Alginate Microparticle Synthesis with Centrifugal Forces.” *Langmuir* 32.28 (2016). PMID: 27311392, pp. 7198–7209.

[40] C. C. L. Schuurmans et al. “Complex coacervation-based loading and tunable release of a cationic protein from monodisperse glycosaminoglycan microgels.” *Soft Matter* 14 (30 2018), pp. 6327–6341.

[41] H. Z. An, H. B. Eral, L. Chen, M. B. Chen, and P. S. Doyle. “Synthesis of colloidal microgels using oxygen-controlled flow lithography.” *Soft Matter* 10 (38 2014), pp. 7595–7605.

[42] A. Cavallo, M. Madaghiele, U. Masullo, M. G. Lionetto, and A. Sannino. “Photo-crosslinked poly (ethylene glycol) diacrylate (PEGDA) hydrogels from low molecular weight prepolymer: swelling and permeation studies.” *Journal of Applied Polymer Science* 134.2 (2017).

[43] Z. Lou et al. “Fabrication of Fe/C composites as effective electromagnetic wave absorber by carbonization of pre-magnetized natural wood fibers.” *Journal of Bioresources and Bioproducts* 4.1 (2019), pp. 43–50.

[44] G.-H. Chen and H.-S. Chen. “Nanometer-Thick Sol–Gel Silica–Titania Film Infused with Superparamagnetic Fe3O4 Nanoparticles for Electromagnetic Interference Shielding.” *ACS Applied Nano Materials* 3.9 (2020), pp. 8858–8865.

[45] A. Li and G. Ahmadi. “Dispersion and deposition of spherical particles from point sources in a turbulent channel flow.” *Aerosol science and technology* 16.4 (1992), pp. 209–226.

[46] D. N. Boon. *Thesis consultant*. Asvalt AB., Accessed: 04-2019 untill 03-2020.

3

PUF MICROPARTICLES FOR ANTICOUNTERFEITING

This chapter is based on the article:
Zhang M., Raghunath A., Zhao A., Eral H. B., Biocompatible optical physically unclonable function hydrogel microparticles for on-dose authentication. Heliyon 2024, 10 (1), e22895.

3.1 Introduction

To combat rampant counterfeiting on packaging, on-dose authentication (ODA) tags were introduced. ODA tags are usually biocompatible and directly embedded into the end products themselves to enable verification of their origin and safety even in the absence of packaging. A few prototypes of ODA tags, from microtaggants [1–5] to macro films [6, 7] including various on-dose printing technologies [8–10] have been demonstrated in recent years. ODA tags are a more robust, resilient, and environmentally friendly alternative to traditional authentication protocols, as they are integrated into solid drugs rather than relying on packaging [11]. However, ODA tags may not yet be at the highest level of safety. For instance, barcodes produced by flow lithography [2, 4] are susceptible to cracking and cloning by sophisticated criminals who have access to the same techniques. In this case, a combination with Physical Unclonable Functions (PUF), i.e., an on-dose PUF that creates an authentication system that cannot be duplicated, is considered an effective solution [6].

Originally developed for hardware and information security, PUFs are important components for highly secure anti-counterfeiting systems [12]. Recently, it was successfully translated by Kim et al.[6] for tagging pharmaceuticals. To avoid any confusion, the term PUF in this study only refers to physical tags for authentication that utilize intrinsic randomness at the microscale or nanoscale introduced during fabrication processes as a unique 'fingerprint' [13].

PUF is usually described as a black box [12] through which input challenges are passed and output responses are returned. It is almost impossible to generate two identical output responses because the PUF tags are fabricated via chemical methods in a stochastic process. By raising the system entropy, the randomness of the resulting PUF tags is immensely increased and consequently ensures the uniqueness of each tag. In this way, it is easy to create but extremely difficult or expensive to clone a particular PUF tag, even using the manufacturer's methods [14]. Since responses are unpredictable, the authentication is secured.

If we view the PUF tag as a type of physical lock, the encoding process, which involves generating a response based on an input challenge, can be thought of as creating a key. It usually involves steps such as the acquisition and digitization of graphical patterns. Taking the example of the PUF system using fluorescent proteins for tagging pharmaceuticals as mentioned above [6], a fluorescence microscope is used under various excitation wavelengths (inputs) to get corresponding unique images (outputs). These images are further digitized into a corresponding cryptographic key, or a 'digital key', via a particular algorithm. This key is stored in a secure database prior to labeling. To authenticate, a key produced by a certain 'physical lock' is compared to the 'digital key' in the database. If two keys match, the labeled product can be considered genuine.

Moreover, a PUF can be created to have an exponential number of input challenge-output response pairs for high security. The end-users can retrieve all the information about the medicine such as the origin, expiry date, side effects, etc. from a database by using a particular reader which will produce the output after scanning the tag and matching it with the stored 'digital keys'.

The fabrication process, image acquisition, and digitization algorithm are crucial to avoid any false reading of on-dose PUF tags. On top of that, the materials adopted should be completely biocompatible. Efforts to prevent counterfeiting using on-dose PUF tags are still in the early stages of development, and there have been few published studies on the topic. Regrettably, the key factors mentioned above have not yet been fully met for practical application.

For example, in addition to the more often seen fluorescent dyes, PUF tags are also reported to have been fabricated with carbon nanotubes [15], colloidal metal nanoparticles [16, 17], cholesteric liquid crystal [18], lanthanide(III) ion dopants [19], rare-earth upconversion nanocrystals [20], and long-lasting fluorescent nanoparticles called quantum dots [21]. Unfortunately, most of these ingredients are toxic and hence forbidden for pharmaceutical applications. Another general problem that arises from fluorescent dyes is the short lifetime due to their easy quenching under improper storage [19]. In this case, the response tends to be unreliable, which can lead to incorrect determinations regarding authenticity.

The selection of material further restrains the method of image capture. For instance, fluorescent PUF tags are specifically acquired via fluorescence microscopy while metal nanoparticles and liquid crystal PUF need to be observed under a dark field microscope, or a Raman microscope [16, 22, 23]. Specifically, Demirok et al.[24] presented a PUF system based on alloy nanowires that can be read in multiple manners including X-ray fluorescence spectrometer, electrochemical microscope, and magnetometer. These techniques were thought to enhance the overall security of the PUF system. However, such sophisticated and bulky appliances constrain the readout to advanced labs. As a result, the reading cost unavoidably increases tremendously when every pharmaceutical tablet needs to be labeled.

For practical applications, one needs to consider the image quality when extracting the patterns. External perturbation cannot always be avoided since pattern recognition is often conducted under different conditions. For instance, the conditions under which the image is obtained for recognition to store the 'digital key' in the database may not be similar to the 'authentication key' at the user's end. The presence of complex patterns in this case instead becomes a drawback in terms of the image quality.

To counter the dire need for high-fidelity images, image processing algorithms usually involve multiple steps such as background correction, color differentiation, binarization, intensity value normalization, etc. [25, 26]. The final step of encoding is the recognition

of the characteristic pattern via a certain algorithm. The algorithms in terms of this field vary and are decided by the patterns. Similar to fingerprint identification where the ridge information is often analyzed [19], the positions and colors of the particles are usually recorded pixel by pixel for particle-embedded PUFs [16, 22]. When the characteristic pattern is composed of nanotubes or nanowires, the orientations or rotational degrees of these lines are often recorded[19, 27]. In other words, color, position, and orientation are generally adopted as inputs.

The corresponding output information is further digitized to reduce the size of the stored data and subsequently reduce the time required for the authentication process [17]. It is worth noting that the input/output complexity positively correlates with the computational cost which we usually wish to minimize to the level that even a mobile phone is sufficient for the user.

Finally, we should consider the authentication algorithm. A widely used model to determine the similarity between two images is comparing them to each other [28]. Such operation is acceptable when dealing with small sets of images, but will be very expensive computationally to individually compare each PUF since the database contains billions of 'digital keys'. For this reason, the string matching method is usually chosen but is still quite costly when the database is huge.

In conclusion, while the aforementioned PUFs are a noteworthy advancement in the realm of anti-counterfeiting, their practical applications are currently restricted due to limitations arising from material selection, image acquisition methodology, and encoding algorithms as discussed earlier.

In this study, we present two types of biocompatible PUF microparticles that utilize microsphere diameter and coordination as input. They are fabricated by embedding microspheres into a biocompatible matrix, Poly(ethylene glycol) diacrylate (PEGDA). The first design showcases a single-diameter on-dose PUF, where randomly distributed superparamagnetic colloids (SPCs) of identical diameters are embedded into PEGDA. The second design features a multiple-diameter system, achieved by embedding sunflower oil droplets of various diameters into PEGDA using a vortex-induced oil-in-water method. These microparticles, due to their biocompatibility and suitability for direct application at the dosage level, are referred to as on-dose PUFs. To extract information from the PUF microparticles, we propose a PUF working algorithm that only requires the diameters and coordinates of the spheres as input. A universal Matlab program capable of circle identification and binning is used to simplify the encoding process. As color and intensity are not utilized as inputs, image acquisition can be accomplished using common illumination and low-magnification microscopy. Furthermore, the performance of the single-diameter PUF was thoroughly examined using a sample size of 16 keys and evaluated using the NIST Statistical Suite (National Institute of Standards and Technology). The results demonstrate that the cryptographic responses exhibit sufficient randomness. Additionally, the single-

diameter on-dose PUF exhibits an impressive encoding capacity of 9.2×10^{18}, which is capable of accommodating the labeling requirements for annual Aspirin production.

3.2 Materials and methods

3.2.1 Materials

Poly(ethylene glycol) diacrylate (average Mn 700), 2-Hydroxy-2-methylpropiophenone (CAS No. 7473-98-5) were purchased from Sigma-Aldrich. Silicon film of thickness 20μm for the fabrication of microchannel was obtained from MyTech Ltd. The superparamagnetic microsphere PS-MAG-FluoYellow-COOH-AR488 with a saturation magnetization ranging from 15~ 25 Am^2/kg, a density of 1.49 g/cm^3 and a diameter of 4.54 μm was purchased from microParticles GmbH. The microsphere consists of a core made of polystyrene with iron oxide particles incorporated inside the polystyrene. The core is covered by a carboxyl group polymer shell with a thickness of 100-500 nm to prevent any leakage of the iron oxide particles to the surrounding medium. For easier observation, fluorescent dyes were also functionalized in the shell. The SPCs are originally packaged as aqueous solutions containing 1wt% of particles that have a coefficient of variation of 5%. The sunflower oil is pursued from local supermarkets and used without any preprocessing.

3.2.2 Preparation of single-diameter PUF microparticle

A 2 cm × 1.5 cm silicon film was first cut. On it a 1 cm × 1 cm square was hollowed out. The cut silicon film was then transferred to a glass slide. Two channels that connected the hollow area were carved to be used as inlet and outlet. After that, the ready channel was covered with a second glass slide and the microfluidic device was ready to use. The injected suspension is a mixture of photo-initiator (2-hydroxy-2-methylpropiophenone) with PEGDA-700 at a proportion 1:20 vol% and without any magnetic susceptibilities tuner to assure the edibility. To get a homogeneous distribution of the SPCs, the suspension was vortexed and placed in a sonication bath for 30 minutes at room temperature. The stop-flow lithography is conducted as previously described [4]. Their images were taken with the Andor CCD camera hooked up to the microscope at 20× magnification.

3.2.3 Preparation of oil/water PUF microparticle

A mixture of sunflower oil and PEG700 at a proportion 1:20 vol% was vortexed for 1 minute. 50 μL of the suspension was drop-cast to a glassslide and covered with another

slide. After that, the liquid film was brought under UV light for 30 seconds and cured. Then the microparticle is finally ready. The liquid film was also cured under UV light through a mask to get PUF particles as stop-flow lithography.

3.3 Results and discussion

3.3.1 Two types of on-dose PUF microparticle

3.3.1.1 *Single-diameter on-dose PUF*

The first on-dose PUF microparticle employs single-diameter as input and its synthesis via stop-flow lithography is depicted in Figure 3.1(a). Firstly, a suspension containing UV-responsive oligomer PEGDA, a photoinitiator, and superparamagnetic colloids (SPCs) are pumped into the microchannel. After the channel is filled, flow is stopped, and an external magnetic field is imposed using a Halbach array magnet. SPCs align when the magnetic field is parallel to the platform and segregate homogeneously when the vertical magnetic field dominates, as shown in Figure 3.1(b). Homogeneous and stochastic distribution of SPCs is crucial, as it serves to eliminate the bias in encoding from the very beginning. Thereafter, UV light passes through a mask to trigger photo-polymerization, and the on-dose PUF in a particle shape can be obtained (see Figure 3.1(e and f)).

Now that the diameter functions as input, microspheres are expected to be fixed in the same depth in this hydrogel microparticle to prevent invalid readings. Without a doubt, the settlement facilitated by gravitational force and Brownian motion will also generate a random scattering of SPCs at the gel bottom. Nevertheless, here, the Halbach magnet accelerates the settling speed of the colloids so a faster fabrication can be achieved, a benefit that magnetic trapping can bring. There are several other benefits via stop-flow lithography. For instance, the geometry of the final on-dose PUF microparticles can be independently controlled by a mask, consequently, the size of on-dose PUFs can be precisely manipulated on a micron scale. Furthermore, images of each microparticle can be recorded simultaneously by the microscope and saved for further processing, which can boost the efficiency of digital key generation. In this manner, database registration can be achieved without slowing the production line. This assists in minimizing the additional cost incurred for the product. Together, these characteristics endow higher security of our microparticle as well as keep the cost at an affordable level.

In addition to the previous discussion, there might be concerns about the biosafety and cytotoxicity of these microparticles. Biosafety has been thoroughly discussed in Chapter 2. The conclusion was that all the ingredients are biocompatible. Furthermore, this single-diameter type can be easily applied using other biocompatible microspheres, such as synthetic polymeric microspheres, which are widely used in medical applications [29].

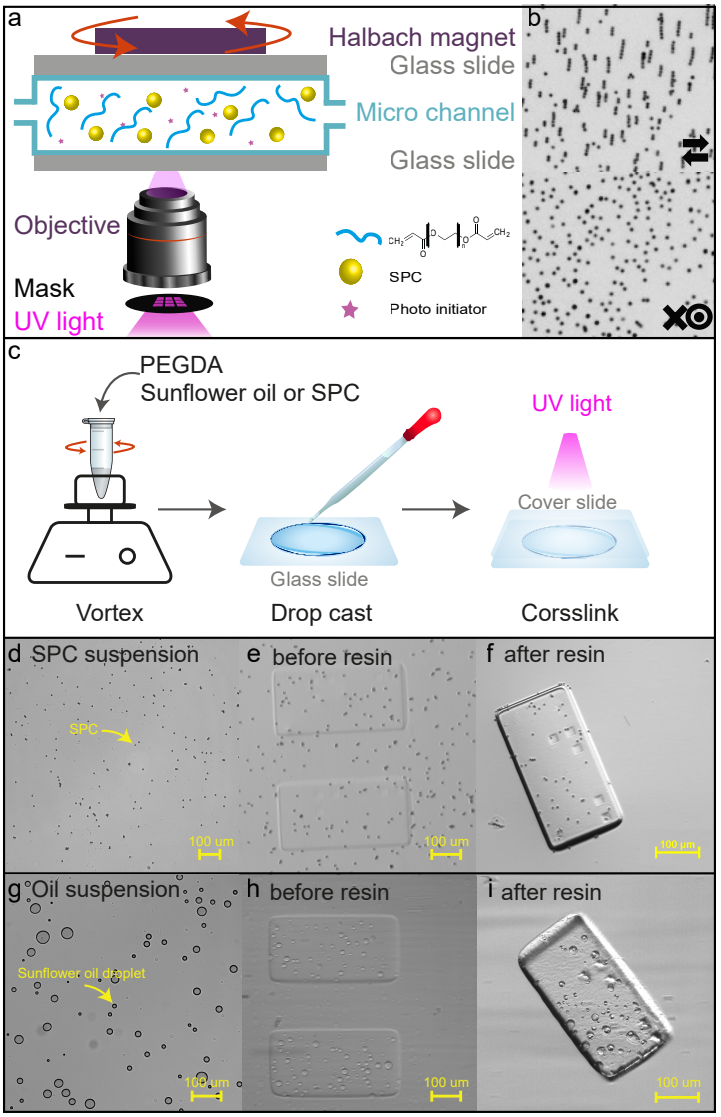

Figure 3.1: Two types of on-dose PUF design: The single-diameter type is created by employing stop-flow lithography of superparamagnetic colloids (SPCs) within Poly(ethylene glycol) diacrylate (PEGDA) (a). The alignment of SPCs is controlled using oriented magnetic fields, as demonstrated in (b). Initially, a suspension of homogeneously and stochastically distributed SPCs is obtained (d), followed by photosynthesis into microparticles. The images of the single-diameter microparticles before and after resin are shown in (e) and (f) respectively. On the other hand, the multiple-diameter type is produced through vortex and drop-casting of sunflower oil and PEGDA suspension, as depicted in (c). The homogeneous and stochastic distribution of oil droplets is first achieved as a suspension (g), and then transformed into microparticles via photosynthesis. The images of the multiple-diameter microparticles before and after resin are presented in (h) and (i) respectively.

3.3.1.2 *Multiple-diameter on-dose PUF*

A multiple-diameter on-dose PUF was prepared via drop casting of immiscible oil/water phase suspension as shown in Figure 3.1(c). Here, sunflower oil was used as the oil phase while PEG700 was used as the water phase. Followed by a short vortex, the suspension was drop cast and cross-linked by UV light. After peeling from the glass slide, a suspension containing various oil droplets is ready as seen in Figure 3.1(g). Moreover, this suspension can also be fabricated into particles if a mask is adopted as shown in Figure 3.1(h and i).

When two immiscible substances are mixed, the disperse phase will form a spherical droplet due to the surface tension. This phenomenon is widely seen in daily life such as the oil droplets in broth. With no control, the dispersed phase tends to create droplets over a wide size distribution, a major factor governing the generation of the PUF pattern, being desirable for multiple inputs. As showcased in Figure 3.1(g), the locations at which those droplets form and their diameters are stochastic parameters. The randomly distributed droplets of various sizes jointly represent the fingerprint patterns. Moreover, the interface between oil and water is distinct for clear visualization due to their appreciable difference in refractive index. Therefore, the droplets can be observed under common illumination sources including sunlight. It is worth noting that there are various ways to create such a wide size distribution, including but not limited to sonication, homogenization, and microfluidic drop-wise emulsification [30], as well as the vortex as showcased in this work. In addition, advanced microspheres such as multi-compartmental microspheres fabricated by gas-shearing [31, 32], microspheres with protrusions and cavities in various shapes [33] can also be transplanted to this system to further improve the safety level by extremely boosting the complexity of patterns. Similarly, the concept of generating unique patterns by randomness is not limited to the materials shown in this work and should be readily applicable to other types of materials.

In summary, the proposed on-dose PUF that utilizes microsphere diameter and coordination as input showcases versatility. It can be fabricated using different methods and ingredients. In the subsequent section, we will present a universal program designed to extract information from these PUFs.

3.3.2 Working algorithm

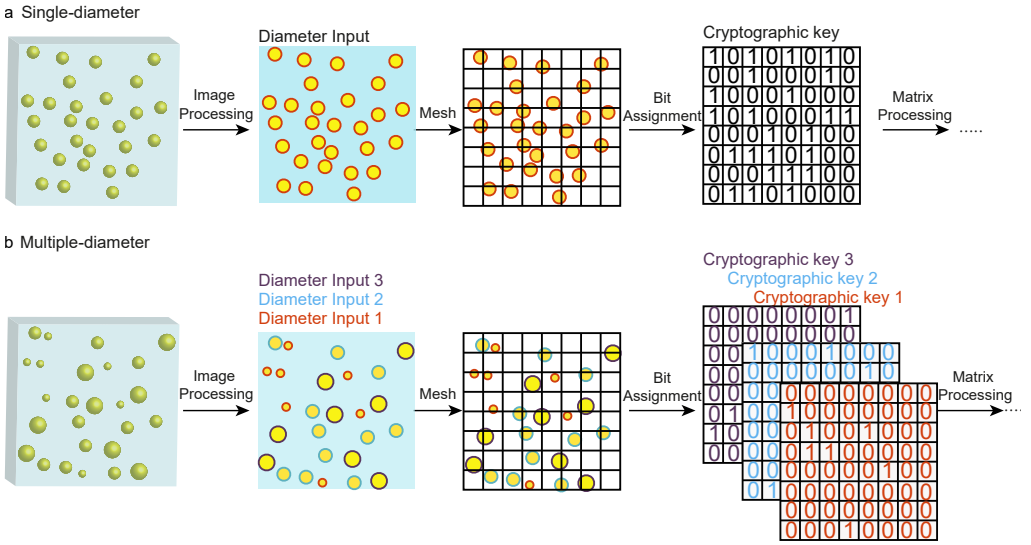

Figure 3.2: Schematic illustration of working algorithm. Cryptographic keys are generated from a diameter-based PUF authentication system using (a) single diameter and (b) multiple diameters as input. Following proper mesh and bit assignment, the cryptographic key, i.e. the output response matrix is further processed depending on the bit uniformity.

Figure 3.2 schematically illustrates the working protocols of key generation using diameter as input. After a proper image of the PUF tag is captured and meshed per certain amounts of pixels, it is processed in Matlab using earlier developed algorithms Hough transform [34]. Via the 3 steps in the Hough transform, i.e., greylization, binarization, and circle detection, the pixel coordinates for the centers of the spheres of a certain diameter input are extracted. After the spheres are identified, the coordinates of the center are then used to make a binary matrix the same size as the mesh. Cells in the binary matrix get assigned a value of *1* when the corresponding pixel in the image contains the center of a sphere, and *0* otherwise. Hough transform is widely used as it saves time using no loops to get a fast circle detection. The 3 steps of the Hough transform are summarized in Table B.S1 and showcased in Figure B.S1 in the Appendix. The MatLab code can also be found in the Appendix b.3.

Since the parameter of diameter can be arbitrarily chosen in the Hough transform, we can manipulate the number of inputs. For instance, for a single-diameter PUF with 5 μm spheres, a binary matrix will be returned if 5 μm is input. However, no circles will be detected if other diameters are input so a zero matrix will be returned instead. In this way, only the correct diameter can yield the desired response. We will not worry if the diameter

is known by counterfeiter because the distribution of bit 1 is random so each response is unique, which will be demonstrated in the following section.

Stronger security can be achieved by a multiple-diameter PUF with spheres of various sizes as shown in Figure 3.2(b). We can enter different inputs, and each input will return a corresponding output. In this way, several layers of cryptographic keys are generated. If the diameters of the spheres, or say, the adopted inputs for key generation, are unknown, the attacker cannot enumerate all possible inputs in a short time. If known, the PUF pattern from a PUF tag with 3 different circle sizes has 4 possible responses at each mesh point. This large challenge–response space makes the prediction almost impossible thanks to the exponential response produced. Still, readout time should be taken into consideration jointly with the input number to obstruct the total enumeration of the PUF [12].

After the matrix is assigned, a bias might show up. We can observe a significant bias toward the "*1*" state if the concentration of materials that loaded to produce circles is too high, or a bias to "*0*" when the concentration is too low. If we take the example of a 512×512 pixel Physical Unclonable Function (PUF), which contains approximately 28 spheres as illustrated in Figure 3.3(Response Binned $\times 1$), it implies that on average, only 28 cells out of the total 512×512 cells in the matrix hold the value of *1*. This indicates a significant bias towards *0* in the data, meaning that it is more probable for a cell to contain a *0* than a *1*. Therefore, such data is more susceptible to key prediction attacks, and it is favorable to reduce the amount of *0*s in this case.

There are various algorithms to reduce entropy leakage such as by utilizing a corrector. In this study, the response matrix was scaled down from 512×512 to 8×8 by applying data binning 6 times with a special rule applied to create the bins. The special rule is that the highest number in the bin is chosen to represent the bin. Since the matrix only contains the logical values of *0* and *1*, any bin containing even a single instance of the value of *1* will be represented by *1*. This binning will reduce the instances of *0* appearing in the matrix thus making it more secure by decreasing bias in the final digital key while retaining the spatial arrangement of the spheres in the physical key. In this way, the binning process is repeated to reach a final 8×8 size with a total of 64 cells. An example of the binning process is presented in Figure 3.3. It can be seen how the distribution of *1*s in the initial matrix develops with each time the binning process is applied. Thereafter, these response matrices can be stored in a secured database for comparison with the 'authentication key'.

The CPU time and wall-clock time of this circle finding and binning of images in 2048×2048 pixels are measured on a laptop (3.0 GHz, Dell Latitude 7320, Quad-Core) using Matlab Online version. The average CPU time was 4.7 seconds while the average wall-clock time was 2.5 seconds. If we implement this set of codes on mainstream mobile phones that are at least equipped with a 2.4 GHz CPU, the wall-clock time would be about 3.2 seconds, which is expected to be within users' acceptance considering the scanning time of QR code in 2953 bytes is reported to be up to 0.5 seconds [35].

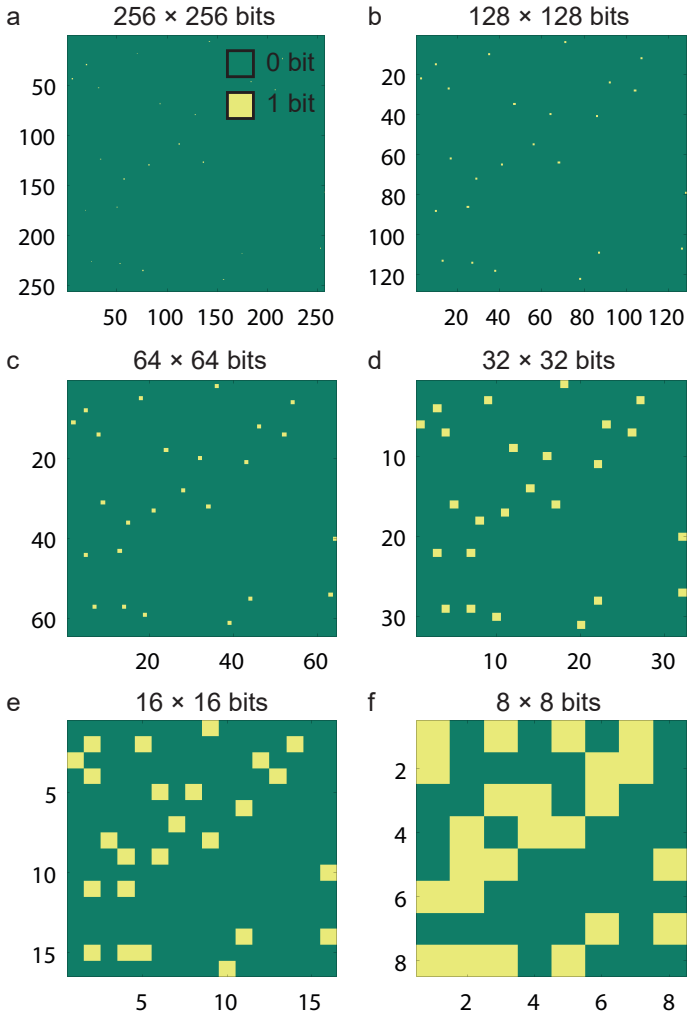

Figure 3.3: Data binning of the output response matrix. An original matrix of 512×512 is scaled down to (a) 256×256 in the first binning, and then to (b) 128×128, (c) 64×64, (d) 32×32, (e) 16×16 and finally to (f) 8×8. At this point, it is apparent that the proportion of *0*s and *1*s is closer to 0.5.

Overall, such a working algorithm of key generation using diameter as inputs combined with matrix binning avoids any expensive imaging system and is computationally efficient. Thus reading a PUF via mobile phone by general users is possible. Moreover, our algorithm removes the hindrance of synthesizing of biocompatible PUF tags, now that toxic fluorescence ingredients are unnecessary.

3.3.3 Evaluation of single-diameter on-dose PUF

3.3.3.1 *Randomness test*

Table 3.1: The results of the NIST test

Type of Test	Pass Rate	P-Value	Conclusion
Frequency Test (Monobit)	32/32	0.000954	Random
Frequency Test within a Block	31/32	0.468595	Random
Cummulative Sums (Forward) Test	32/32	0.739918	Random
Cummulative Sums (Reverse) Test	31/32	0.350485	Random
Run Test	32/32	0.178278	Random
Serial test	31/32	0.602458, 0.028181	Random
Approximate Entropy Test	31/32	0.178278	Random

Note: The P-value that resulted from each test is compared with the significance level (α of 0.01 in the first level test and 0.0001 in the second level test) to come to the conclusion of whether to accept the null hypothesis that the data is random. For a sample size of 32 binary sequences, the minimum passing rate for each statistical test is approximately 29.

A group of 16 single-diameter on-dose PUFs is produced and processed into 16 corresponding 'digital keys'.National Institute of Standards and Technology statistical test suite NIST SP 800–22 is adopted to assess whether any patterns can be detected that make it possible to predict the bit sequence. The results are summarized in Table 3.1. Here we canonically choose the single-diameter on-dose PUFs because it represents single input and thus is more vulnerable to attack. The resulting 16 images are 512×512 pixels in size with 0.32 μm per pixel and are provided in Figure B.S2 in the Appendix.

SP 800–22 is a widely used package to test for randomness for Random Number Generator (RNG)s [36]. Statistical testing involved choosing a null hypothesis (H_o) and an alternative hypothesis (H_a). For the randomness test, they are *Data is random* for H_o and *Data is not random* for H_a respectively. NIST SP 800-22 includes a set of 15 one-level tests and 2 two-level tests, which assess various aspects of randomness. Each one-level

test produces one or more p-values and returns as a pass rate (i.e., the proportion of the passed sequences), while the two-level tests evaluate the consistency of the p-values obtained from a particular one-level test.

To assess the validity of the null hypothesis and accept the alternative hypothesis, a significance level, denoted by α, is established for the P-value[36]. When $p \leqslant \alpha$, the null hypothesis is rejected, and the alternative hypothesis is accepted. To demonstrate that the data is random and the bits are uncorrelated with each other, higher P-values than α are preferred[37]. The significance level is dependent on the sample size, and the minimum sample size for a specific α can be calculated using mathematical computations[37]. For the first level of testing, the α value is set to 0.01, whereas for the second level, it is set to 0.0001, as per the NIST guidelines[38].

The investigation of each test in the group of 15 requires a minimum sequence length of the bitstream under investigation. In this study, the bitstream being tested is the combination of the digital keys of all 16 on-dose PUFs, resulting in a total sample size of 1024 as shown in Figure B.S3 meanwhile the raw data are presented in the Appendixb.4. Due to the short key size, only the tests that require a sequence length of less than 1024 are considered. Therefore, the selected tests for this study are the Frequency (Monobit) Test, Frequency Test within a Block, Runs Test, Longest Run of Ones in a Block, Serial Test, Approximate Entropy Test, and Cumulative Sums Test.

In Table 3.1, it can be seen that the bit stream from the digital key produced a p-value of a chi-squared ($\chi 2$) test and a pass rate in every test it was subjected to. The P-values are above the α. This means that the null hypothesis can be accepted for each test. Hence, the output from the on-dose PUFs is statistically random and consequently unpredictable, and thus unclonable.

3.3.3.2 *Bit Uniformity*

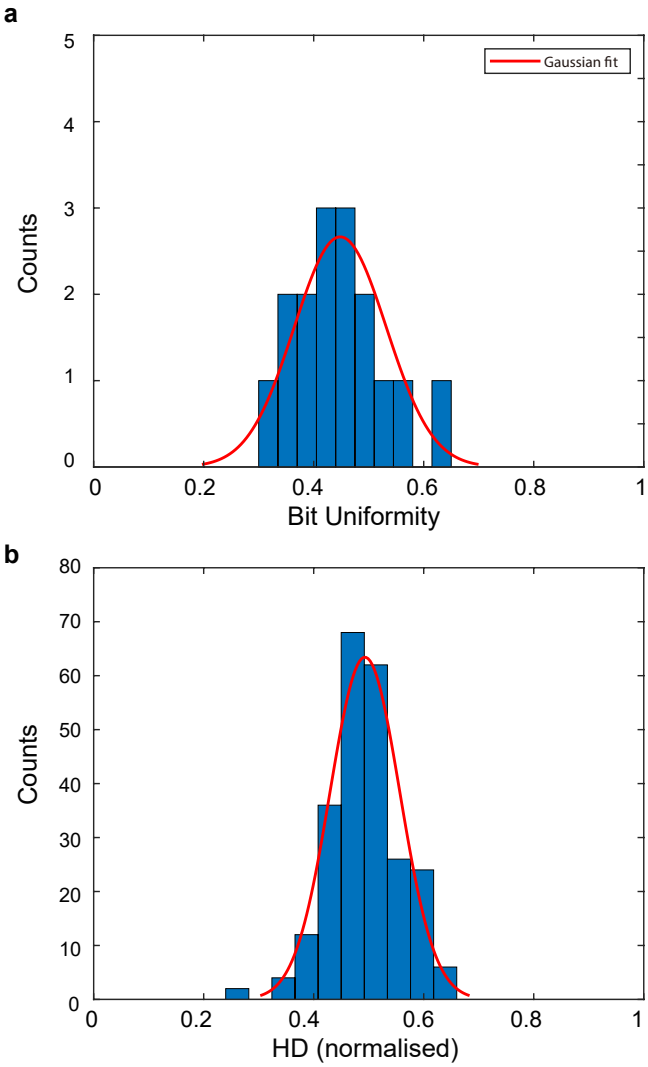

Figure 3.4: Performance characteristics in bit uniformity and Hamming distance. (a) The bit uniformity of the 16 different digitized on-dose PUF keys shows a close resemblance to a normal distribution and the Gaussian fit of the data produces a mean (μ) of 0.45 with a standard deviation (σ) of 0.084. (b) The pairwise Hamming distances of the 16 different digitized on-dose PUF keys show a close resemblance to a normal distribution and the Gaussian fit of the data produces a mean (μ) of 0.49 with a standard deviation (σ) of 0.063.

Bit uniformity of the above 16 single-diameter PUFs is investigated and shown in Figure 3.4(a). Bit uniformity is the proportion of *1* bits in the bit sequence, which is also known as the Hamming Weight [6]. The distribution of Hamming Weights in the on-dose PUF system should be similar to a normal distribution. From Figure 3.4(a), the mean (μ) can be observed to be close to 0.5 which is the ideal value indicating only a low bias in the data. This indicator can be optimized by manipulating the binning times in this study as we have previously shown in Figure 3.3. However, the binning will reduce the matrix size and consequently decrease the encoding capacity. This is not ideal when information-rich-PUF is needed. To avoid any unnecessary information loss, the concentration of the loaded SPCs is recommended to be precisely calculated before binning is applied.

3.3.3.3 *Hamming distance*

At the same time, Hamming Distances were found for every pair of keys and shown in Figure 3.4(b). The Hamming Distance is the number of bits that differ at the corresponding positions in two PUF keys. C_{16}^{2} combinations are possible yielding 120 values which should also resemble a normal distribution when plotted (seen AppendixB.S4). From Figure 3.4(b), the Gaussian fit of the Hamming Distance produces a μ of 0.49 and σ of 0.063 for this particular set of 16 PUFs. Since the Hamming distance is influenced by the similarities and differences between the keys, the μ and σ of the Gaussian fit can be used to find out the degrees of freedom of the PUF system by Equation 3.1. Using the degrees of freedom, the actual encoding capacity for this set of PUFs can be determined by Equation 3.2.

$$\text{Degrees of Freedom} = \frac{\mu \times (1-\mu)}{\sigma^2} = \frac{0.49 \times (1-0.49)}{0.063^2} \approx 63 \tag{3.1}$$

$$\text{Encoding Capacity} = 2^{63} = 9.2 \times 10^{18} \tag{3.2}$$

The Hamming distance distribution for this particular set of 16 PUFs is close to the ideal value of 0.5. With a single diameter input and a small encoding matrix of 8×8 cells, the encoding capacity already approaches 9.2×10^{18} for this canonical case. This capacity will grow exponentially with the number of inputs. It is quite promising to reach the ideal encoding capacity of PUF which is approximately 10^{300} [19].

3.3.3.4 *Device uniqueness*

Finally, the probability of similarity in corresponding bits in two random PUF keys in the system, termed as the device uniqueness, is evaluated. There are several traditional

metrics available to evaluate the device uniqueness, here we choose the mean of the inter-device Hamming distance i.e., HD_{mean} [6]. The outcome of HD_{mean} ranges from 0.0 to 0.5. The worst inter-device uniqueness is 0.0 when all devices generate the same signature. With a growing number of devices, this value can converge to 0.5, the most ideal value for uniqueness metric [39].

In this study, the HD_{mean} of the PUF system with mere 16 individual keys being investigated is calculated as 0.49, which is very close to the ideal value of 0.5. Thus, each key is considered to produce a unique response based on the entropy of the settling spheres.

3.4 Conclusion

On-dose PUFs have emerged as an appealing solution to tackle the rampant problem of counterfeit food and pharmaceuticals, due to level of security and affordability they offer. In an effort to expand the possibilities of input methods, we propose a PUF working algorithm that leverages both size of embedded objects (colloids and emulsion droplets) in a hydrogel particle and their coordinates as inputs. This study is the first exploration of its kind to utilize these parameters in optical PUFs to the best of our knowledge. Building on this idea, we developed two biocompatible on-dose PUF systems that rely on the entropy of randomly distributed SPCs or oil droplets to demonstrate the use of single or multiple inputs. The randomness and performance of the single-diameter PUF were evaluated and found to be ideal. These PUF microparticles can be read with bright field illumination. Moreover, the algorithm is computationally efficient, allowing for easy authenticity verification by general consumers, thus creating a significant hindrance to counterfeiting activities.

REFERENCES

[1] S. Han et al. “Lithographically Encoded Polymer Microtaggant Using High-Capacity and Error-Correctable QR Code for Anti-Counterfeiting of Drugs.” *Advanced Materials* 24.44 (2012), pp. 5924–5929.

[2] I. Rehor et al. “Biodegradable Microparticles for Simultaneous Detection of Counterfeit and Deteriorated Edible Products.” *Small* 13.39 (2017), p. 1701804.

[3] Y. C. Saraswat et al. “Shape anisotropic colloidal particle fabrication using 2-photon polymerization.” *Journal of colloid and interface science* 564 (2020), pp. 43–51.

[4] M. Zhang, T. Warth, N. Boon, A. F. Demirörs, and H. B. Eral. “Microfluidic Synthesis of Hydrogel Microparticles with Superparamagnetic Colloids Embedded at Prescribed Positions for Anticounterfeiting Applications.” *Advanced Materials Interfaces* (2022), p. 2200899.

[5] T. Yasunaga, T. Fukuoka, A. Yamaguchi, N. Ogawa, and H. Yamamoto. “Physical stability of stealth nanobeacon using surface-enhanced Raman scattering for anti-counterfeiting and monitoring medication adherence: Deposition on various coating tablets.” *International Journal of Pharmaceutics* 624 (2022), p. 121980.

[6] J. W. Leem et al. “Edible unclonable functions.” *Nature Communications* 11.1 (2020), p. 328.

[7] S. Takei. “Safety-oriented photolithography of water-soluble resist using water-coating and water-developable processes for edible pharmaceutical polymer films.” *Applied Physics Express* 11.8 (2018), p. 086501.

[8] K. Ludasi et al. “Anti-counterfeiting protection, personalized medicines- Development of 2D identification methods using laser technology.” *International Journal of Pharmaceutics* 605 (2021), p. 120793.

[9] S. J. Trenfield et al. “Track-and-trace: Novel anti-counterfeit measures for 3D printed personalized drug products using smart material inks.” *International Journal of Pharmaceutics* 567 (2019), p. 118443.

[10] H. Öblom et al. “Data-enriched edible pharmaceuticals (DEEP) of medical cannabis by inkjet printing.” *International Journal of Pharmaceutics* 589 (2020), p. 119866.

[11] H. Zhang et al. “Materials and technologies to combat counterfeiting of pharmaceuticals: current and future problem tackling.” *Advanced Materials* 32.11 (2020), p. 1905486.

[12] C. Herder, M.-D. Yu, F. Koushanfar, and S. Devadas. “Physical unclonable functions and applications: A tutorial.” *Proceedings of the IEEE* 102.8 (2014), pp. 1126–1141.

[13] Y. Gao, S. F. Al-Sarawi, and D. Abbott. “Physical unclonable functions.” *Nature Electronics* 3.2 (2020), pp. 81–91.

[14] C. Herder, M. Yu, F. Koushanfar, and S. Devadas. “Physical Unclonable Functions and Applications: A Tutorial.” *Proceedings of the IEEE* 102.8 (2014), pp. 1126–1141.

[15] Z. Hu et al. “Physically unclonable cryptographic primitives using self-assembled carbon nanotubes.” *Nature nanotechnology* 11.6 (2016), pp. 559–565.

[16] A. F. Smith, P. Patton, and S. E. Skrabalak. “Plasmonic nanoparticles as a physically unclonable function for responsive anti-counterfeit nanofingerprints.” *Advanced Functional Materials* 26.9 (2016), pp. 1315–1321.

[17] J. Kim et al. “Anti-counterfeit nanoscale fingerprints based on randomly distributed nanowires.” *Nanotechnology* 25.15 (2014), p. 155303.

[18] Y. Geng et al. “High-fidelity spherical cholesteric liquid crystal Bragg reflectors generating unclonable patterns for secure authentication.” *Scientific reports* 6.1 (2016), pp. 1–9.

[19] M. R. Carro-Temboury, R. Arppe, T. Vosch, and T. J. Sørensen. “An optical authentication system based on imaging of excitation-selected lanthanide luminescence.” *Science advances* 4.1 (2018), e1701384.

[20] J. Lee et al. “Universal process-inert encoding architecture for polymer microparticles.” *Nature materials* 13.5 (2014), pp. 524–529.

[21] O Ivanova, A Elliott, T Campbell, and C. Williams. “Unclonable security features for additive manufacturing.” *Additive Manufacturing* 1 (2014), pp. 24–31.

[22] Y. Zheng et al. “Unclonable Plasmonic Security Labels Achieved by Shadow-Mask-Lithography-Assisted Self-Assembly.” *Advanced Materials* 28.12 (2016), pp. 2330–2336.

[23] K. J. Si et al. “Dual-Coded Plasmene Nanosheets as Next-Generation Anticounterfeit Security Labels.” *Advanced Optical Materials* 3.12 (2015), pp. 1710–1717.

[24] U. K. Demirok, J. Burdick, and J. Wang. “Orthogonal multi-readout identification of alloy nanowire barcodes.” *Journal of the American Chemical Society* 131.1 (2009), pp. 22–23.

[25] M. Yang et al. “A smartphone-based quantitative detection platform of mycotoxins based on multiple-color upconversion nanoparticles.” *Nanoscale* 10.33 (2018), pp. 15865–15874.

[26] A. W.-C. Liew, H. Yan, and M. Yang. “Pattern recognition techniques for the emerging field of bioinformatics: A review.” *Pattern Recognition* 38.11 (2005), pp. 2055–2073.

[27] S. Johansen, M. Radziwon, L. Tavares, and H.-G. Rubahn. “Nanotag luminescent fingerprint anti-counterfeiting technology.” *Nanoscale research letters* 7.1 (2012), pp. 1–5.

[28] P. Sharma and M. Kaur. “Classification in pattern recognition: A review.” *International Journal of Advanced Research in Computer Science and Software Engineering* 3.4 (2013), pp. 298–306.

[29] K. Saralidze, L. H. Koole, and M. L. Knetsch. “Polymeric microspheres for medical applications.” *Materials* 3.6 (2010), pp. 3537–3564.

[30] K Krutkramelis, B Xia, and J Oakey. “Monodisperse polyethylene glycol diacrylate hydrogel microsphere formation by oxygen-controlled photopolymerization in a microfluidic device.” *Lab on a Chip* 16.8 (2016), pp. 1457–1465.

[31] G. Tang et al. “Gas-shearing fabrication of multicompartmental microspheres: a one-step and oil-free approach.” *Advanced Science* 6.9 (2019), p. 1802342.

[32] G. Tang et al. “Faithful fabrication of biocompatible multicompartmental memomicrospheres for digitally color-tunable barcoding.” *Small* 16.24 (2020), p. 1907586.

[33] S. Sacanna et al. “Shaping colloids for self-assembly.” *Nature communications* 4.1 (2013), pp. 1–6.

[34] MathWorks. *imfindcircles Description*. 2015. URL: `http://nl.mathworks.com/help/images/ref/imfindcircles.html`.

[35] H. A. Wahsheh and M. S. Al-Zahrani. “Secure and usable QR codes for healthcare systems: the case of covid-19 pandemic.” *2021 12th International Conference on Information and Communication Systems (ICICS)*. IEEE. 2021, pp. 324–329.

[36] A. Rukhin, J. Soto, J. Nechvatal, M. Smid, and E. Barker. *A statistical test suite for random and pseudorandom number generators for cryptographic applications*. Tech. rep. Booz-allen and hamilton inc mclean va, 2001.

[37] C. Georgescu, E. Simion, A.-P. Nita, and A. Toma. “A view on NIST randomness tests (In)Dependence.” *2017 9th International Conference on Electronics, Computers and Artificial Intelligence (ECAI)*. 2017, pp. 1–4.

[38] A. L. Rukhin. *A statistical test suite for random and pseudorandom number generators for cryptographic applications*. Tech. rep. 2001.

[39] A. Maiti, V. Gunreddy, and P. Schaumont. “A systematic method to evaluate and compare the performance of physical unclonable functions.” *Embedded systems design with FPGAs*. Springer, 2013, pp. 245–267.

4

HUMIDITY INDICATOR

This chapter is based on the article:
Zhang, M., Arunachalam, A., Perrin, H., Polat, S., Groenewold, J., Mendes, E., Eral, H. B., An Edible Humidity Indicator that Responds to Changes in Humidity Mechanically, ACS Applied Polymer Materials 2023, 5 (7), 4780-4788.

4.1 Introduction

The best-by-date information is mandatory and printed on packages of perishable products. Yet it does not provide dynamic information on product safety prior to consumption. For instance, several products past these dates are usually safe to eat depending on consumer handling practices [1]. Meanwhile, perishable products can also spoil before the reported best-by dates under improper storage conditions. Approximately 10% of food waste is a consequence of misinterpretation of the best-by date[2], resulting in considerable environmental and economic costs. Therefore, intelligent tags that can dynamically report on the storage environment are considered efficient to address these issues in food safety.

Intelligent tags are designed to monitor the storage environment of perishable products in a cost-efficient manner[3]. Macroscopic size intelligent tags such as temperature tags [4–9] and gas tags [10–14] have been widely studied and are constantly reported in recent years. In addition to macroscopic size intelligent tags, microparticles[15] that can report changes in pH[16] or carry encoded information[17] and respond to external stimuli[18] have also been reported.

Detection of humidity is often overlooked in the research field of intelligent tags despite its relevance in the storage of perishable products. Condensation of moisture on perishables can lead to hastened deterioration, bacterial growth, and reduction in their estimated shelf life. Some common undesirable effects of excess humidity in food include caking, stickiness, lumping, crumbling, and molding [19]. Medicines formulated as tablets and powders can also disintegrate or cake by absorbing excess moisture [20]. Moreover, medicines can deteriorate or exhibit undesirable chemical reactions, leading to reduced drug potency in the presence of excess moisture.

Research on humidity tags remains sparse to date despite the importance of humidity control as discussed above. The majority of reported humidity tags are chemo-chromatic, hence they respond to changes in humidity by changing their color[12, 21, 22] while other examples by virtue of geometric deformation have also been proposed [23, 24].

Thompson et al. [21] proposed a chemo-chromatic tag using cobalt chloride tag estimating the water activity of dried products. The easy hydration and dehydration reaction between $CoCl_2$ and $CoCl_2 \cdot 6H_2O$ induces a color change, thus indicating a humidity shift. However, direct contact with consumable products was not advised due to the fact that chronic ingestion of cobalt compounds has been widely reported to cause serious health problems [25]. Therefore, users are only recommended to place this tag on the outside of the packaging, which introduces the risk of reading the ambient humidity instead of the true condition experienced by the target products. To overcome that, Bridgeman et al. [26] proposed a hygroscopic composite tag of less toxic chemicals, i.e., sodium borohydride and DenimBlu30 dye. In this tag, DenimBlu30 dye functions as a redox indicator and

evolves from yellow to blue after absorbing water, hence reporting the humidity increase. However, direct contact is still not recommended due to toxicity concerns.

Abandoning chemical reactions, Snyder et al. [24] presented a tailored shape memory polymer of which the glass transition temperature can be driven lower to the operational temperature by vapor pressure. The absorbed water drives this transition by increasing the free volume and the mobility of polymer chains. Therefore, the initial rigid polymer develops into a flexible elastomeric state over time under vapor. However, the reversibility of this polymer only endows an instant humidity value and not the moisture exposure history.

Ionic liquids (ILs) have gained attention in recent years as they can be immobilized in polymer or metal-organic frameworks, enabling the creation of flexible composites that exhibit high sensitivity, fast response, and wearability as humidity sensors [27–31]. A noteworthy study by Esteves et al. focused on gelatin/ILs-based formulations, functioning as electrical and optical sensors, the formulations can be tailored to respond to humidity and detect volatile organic compounds under dry and humid conditions.

Despite the recent progress in intelligent tags, a biocompatible humidity indicator that can be placed in direct contact with food and medicine without contamination risk has not yet been reported in the literature to the best of our knowledge. The biocompatibility of the ionic liquids is not discussed in the above studies, it is quite promising to design fully biocompatible ILs humidity sensors. Nevertheless, reading ILs-based sensors requires the use of electrical devices due to the chemisorption of water molecules on the ILs which enhances its ionic conductivity and capacitance. However, this increases the cost of producing humidity tags and has environmental implications as the materials used in fabricating these electrical devices are typically plastics and metals. In addition, the indicators discussed above[21, 22, 24, 28], unfortunately, exhibit reversible changes. Since a perishable product exposed to high humidity conditions still shows deterioration or bacterial growth even if the humidity is brought back to the recommended level, it is impractical to interpret spoilage accurately using reversible indicators. Therefore, a food-grade, edible, non-toxic and irreversible humidity indicator with a tunable response time that matches the spoilage course is desirable.

In this chapter, we report an edible humidity indicator (EHI) made of food-grade ingredients that responds to undesired humidity exposure by irreversibly deforming and rolling on itself. The indicator is made of two food-grade polymer films with distinct protein, caseinate to plasticizer, glycerol ratios. Caseinate, originating from bovine milk, has been repeatably reported as a promising biodegradable packaging alternative in recent years[32]. Based on the thermogravimetric analysis, we hypothesize that the bending mechanism is a result of hygroscopic swelling and consequent counter diffusion of glycerol and water. Leveraging our understanding of the bending mechanism, we demonstrated that EHI's lag time, response time, and bending curvature can be tuned to expand its application scope.

Overall, the developed indicator shows the potential to irreversibly detect undesired humidity exposure. The humidity indicator's versatility is attributed to its ability to tune the lag time and response time by changing the layer thickness, making it suitable for applications where humidity changes occur gradually or infrequently over an extended period. The demonstrated response time is slow for applications requiring real-time or near-real time response. The indicator's deformation in response to humidity makes it also suitable for use as a humidity-activated actuator, particularly in situations where low humidity levels need to be maintained. Moreover, thanks to its food-grade hence edible ingredients, the EHI has two distinct advantages compared to commercial non-edible electronic and chemo-chromatic sensors. Firstly, the EHI can be placed in direct contact with perishable products hence it can report on the humidity level inside the packaging without any risk of contaminating the product. Secondly, in case the EHI is accidentally ingested, for instance, by infants or children, it does not pose any risk of oral toxicity.

4.2 Materials and methods

4.2.1 Fabrication of the EHI

The EHI is composed of two films containing distinct amounts of caseinate, glycerol, and water in each. We refer to the film with higher and lower glycerol ratios as high-glycerol film (HGF) and low-glycerol film (LGF) respectively. An illustration of the film production procedure (Figure 4.1(a)) and will be detailed as follows.

To prepare the film-forming mixtures, ultrapure water (Millipore MilliQ IQ 7000 system, 18 mΩ cm) and glycerol (CAS 56-81-5, Boom B.V, 86%) were mixed and magnetically stirred at 600 RPM and 60 °C. To this solution, sodium caseinate (CAS 9005-46, Sigma Aldrich) was gradually added over time intervals of 2-3 min to reach desired caseinate/glycerol/water ratio, which is 12:14:100 for the HGF (dyed blue) while 12:3:100 for the LGF (dyed pink) respectively. The stirring rate was subsequently increased to 850 RPM for 60 min. Afterward, food dyes (Dr. Oetker) were added to distinguish the HGF and LGF. The final mixtures were centrifuged at 7400 RPM for 12 min to remove any bubbles formed during the mixing process.

Film-forming mixtures were cast into plastic Petri dishes (9 cm in diameter, Sigma Aldrich) and baked in the oven at 40 °C for 48 hours. After gelation, the films were peeled off and stored in a desiccator (RH 10%). Films are conditioned for 24 hours in an environmental chamber (BTL-433, ESPEC) under specific RH before the test.

Moreover, the thickness of the film was controlled by the amount of the mixture used and measured by a film thickness gauge (Heidenhain). For instance, a 12 ml mixture can obtain an HGF of 0.310 mm thick and an LGF of 0.155 mm.

4.2.2 Protocol of demonstrations

The utility of EHIs is demonstrated with a urinalysis reagent strip (InSight, Acon Laboratories). An EHI strip (0.155 mm-HGF and 0.155 mm-LGF) of 5 mm by 20 mm was cut and attached to the blank end of the urinalysis strip along the short side with Norland Optical adhesive that cures using ultraviolet light. All EHIs were conditioned under 10% before usage and then exposed to atmospheric humidity that simulated a consumer leaving the actual storage bottle open by accident. The test was conducted at a lab temperature that fluctuated around 23 °C. After 48-hour atmospheric humidity exposure, we kept the test urine strip back in the desiccator for 4 hours to examine any reversibility. Followed with that, a urinalysis test was conducted on the model strip and compared with an original strip unexposed to atmospheric humidity. The preparation of artificial urine is the same as described in the literature [33].

For visualization, the EHI response was recorded throughout the process in the form of a time-lapse with an action camera (4K/30FPS video resolution, 20 megapixels, and a 170-degree super wide-angle 6G fisheye lens, Apexcam) to visualize the process. To measure the curvature evolution, the recorded time-lapse film was extracted per certain frames. The radius (R) of the rolled EHIs was analyzed using ImageJ. The rolling curvature was calculated as $\frac{1}{R}$.

4.2.3 Thermogravimetric analysis (TGA)

The thermal properties of the caseinate samples obtained in different glycerol concentrations media were examined using thermogravimetric analysis (TGA) conducted on an SDTQ600 instrument. In each analysis, approximately 8.0±0.5 mg sample was placed in an aluminum oxide crucible and heated over temperatures ranging from 30 °C to 750 °C at a rate 20 °C/min. A continuous nitrogen flow at a rate of 30 mL/min was supplied to TGA to maintain an inert atmosphere.

4.2.4 Thickness and aspect ratio test

For the thickness test, two combinations were tested. Combination 1 (C1) was made of a 0.155 mm-thick HGF and a 0.155 mm-thick LGF while combination 2 (C2) was a 0.206 mm-thick HGF and a 0.155 mm-thick LGF. After conditioning separately under 50% RH for 24 hours, the single-layer films were stuck together and immediately cut into rectangular strips. One end of the samples was fixed to a glass slide with water-proof tape. The ready-to-test EHIs are 15 mm in length. After that, the samples were transferred into the environmental chamber at 80% RH and a constant temperature of 25 °C. The EHI response was recorded in time-lapse from the top view to visualize the rolling process.

Finally, pictures were extracted and the projected area of the rolled circle was analyzed using ImageJ image analysis software. We use *Normalized Area* to represent the rolling in this test, which was calculated as Projected area/Initial area.

For the aspect ratio test, the conditioning and test procedure were the same as the thickness test as described above besides that samples were cut into rectangular strips of various lengths and widths. We only focus on the final geometries. Therefore, images were only captured after the rolling was completed. The radius (R) of the rolls was analyzed using ImageJ as well.

4.3 Results and discussion

4.3.1 Fabrication and demonstration

The fabrication process consists of several simple steps (Figure 4.1(a)) and is detailed in Section *Fabrication of the EHI*. In a nutshell, aqueous solutions containing two distinct ratios of caseinate and glycerol are evaporated to form films. To distinguish high glycerol (HGF, blue) and low glycerol (LGF, pink) content films, blue and pink food dyes are added to the solutions prior to the evaporation step, respectively. Upon drying, the caseinate and glycerol solutions form a film. Due to the higher water affinity of glycerol, the HGF tends to absorb more water and swells further (Figures C.S1, C.S2 in the Appendix). The films are conditioned by storing them in desired humidity over 24 hours. The conditioned films are then attached to each other leveraging the intrinsic sticky nature of films to fabricate bilayer EHIs.

To avoid potential oral toxicity issues, EHIs are made of only food-grade ingredients, namely, caseinate, glycerol, and water. Caseinate is proposed as biodegradable packaging material [34] due to its attributes such as biocompatibility, biodegradability, and wide availability. Meanwhile, the casein film on its own is brittle and hence not easy to handle. Various amounts of food-grade plasticizer glycerol are added to each layer to improve its flexibility. To ensure that EHIs are made of entirely non-toxic ingredients, no glue is adopted in the *stick-together* step. Perhaps due to caseinate's self-healing ability which rises from its coiled nature and ability to form weak intermolecular interactions within polymeric networks, i.e. electrostatic, hydrophobic, and hydrogen bonds as mentioned above[35], the single caseinate films can attach to each other and form a stable bilayer film. A scanning electron microscope image (Figure C.S3 in the Appendix) shows that the gap between the two layers is negligible. In general, this composite bilayer contains only edible ingredients, which avoid any safety concern about direct contact with edible products.

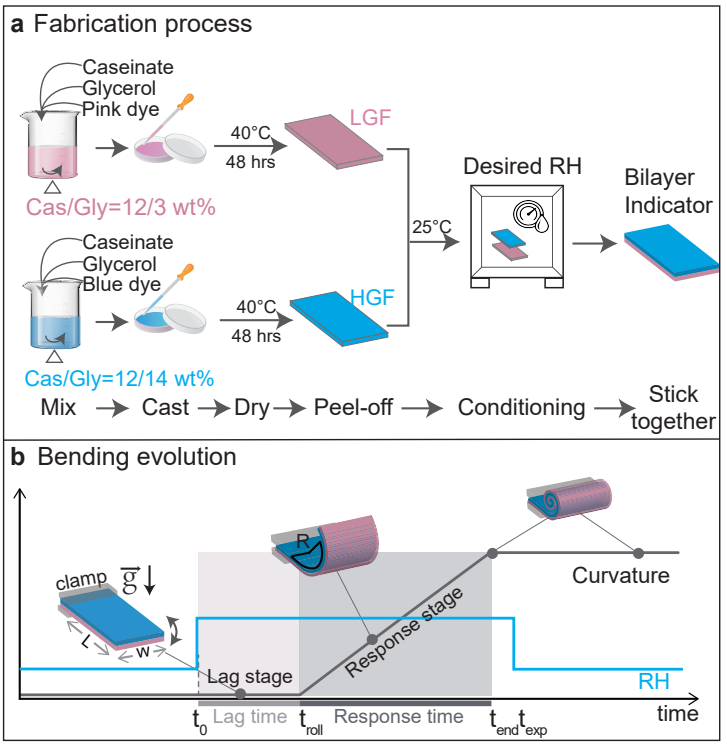

Figure 4.1: (a) Schematic representation of the fabrication process of the edible humidity indicator (EHI). (b) The flat EHI bends and rolls on itself to report humidity exposure. The bending evolution is irreversible and exhibits two stages including *Lag stage* and *Response stage*, which is schematically shown in the zoom plot (bottom). Figure not drawn to scale.

4.3.1.1 *Bending evolution*

The EHIs response to accidental humidity exposure is illustrated as bending curvature development (Figure 4.1(b)). Moreover, the curvature development and macro shape of EHI are detailed as well. The curvature is defined as the inverse radius of bending (R) as illustrated. Prior to humidity exposure, the EHI keeps its flat shape for a relatively long time (at least 15 days under 10% RH, Figure C.S4 in the Appendix). We observed two distinct regimes, a *Lag stage* where the EHI absorbs water from the environment with no significant bending followed by a *Response stage* where EHI deforms and gradually rolls on itself. After that, EHI does not revert back to its initial shape when the humidity level is brought down. We refer to this experimental observation as the irreversible bending of EHI, a feature that is essential for detecting and reporting humidity exposure.

To be more specific, we define *Lag stage* as the stage from t_0 to t_{roll} where t_0 is the moment the EHI is exposed to a high humidity level while t_{roll} is the moment the EHI starts to roll (see Figure 4.1(b)). In this *Lag stage*, the EHI commences to bend slightly and the direction of this minute bending changes multiple times yet the curvature is negligible compared to *Response stage*. From t_{roll} on, the EHI enters into the *Response stage* where a pronounced bending is observed with a bending direction towards HGF. In other words, HGF remains inside the rolled structure. The curvature of the bending increases over time and the EHI can roll on itself to form multiple rolls. After t_{end}, the EHI holds its shape even when the humidity is brought back to the initial RH levels after days.

The reported bending and consequent rolling behavior are observed in other systems as a result of a mismatch in layer properties [36]. Especially, the rolling phenomenon in hydrogel system induced by hygroscopic swelling difference between the two layers has been reported and leveraged in the design of hygroscopic bilayer structures [37–42]. In these bilayer structures, one layer expands more and induces compressive stress on the other layer. Consequently, the hydrogel bilayer structure bends towards the layer with lower swelling ratio. In other words, when these hydrogel bilayers bend and roll upon humidity exposure, less hygroscopic (less water-absorbing) film remains inside the rolled structure. We refer to this bending direction as rolling onto the less hygroscopic film.

Surprisingly, such a bending direction is not observed in our study. EHI sways back and forth slowly at the early stages of the exposure, it eventually bends toward and rolls onto HGF (more hygroscopic film, blue) regardless of RH value, EHI composition, or geometry. In other words, HGF (blue) remains inside the rolled structure and LGF (pink) remains outside (Figure 4.1(b)). This is intriguing since HGF has a higher water adsorption ability and a higher swellability than LGF (see Figures C.S1, C.S2 in the Appendix). If the bending mechanism of EHIs was identical to the aforementioned hydrogel bilayer structures, bending towards LGF would be expected. As we observe a different bending direction from the hydrogels in literature, the bending mechanism of EHI can not be solely explained with distinct water adsorption capacity of two layers attached together, namely HGF and LGF. A different rolling mechanism is needed to explain this observation.

4.3.1.2 *Demonstrations*

We showcase how EHI can be implemented to monitor humidity levels of urine strips that need to be kept in a desiccated environment (Figure 4.2). The urine test strip aids in the fast screening of various diseases[43]. Improper handling and storage of these test strips, especially due to humidity exposure, have been reported to give rise to incorrect diagnosis[44]. We test whether EHI can be used to detect urine test strips with compromised functionality due to humidity exposure (Figure 4.2).

For this test, we exposed urine strips with EHIs attached to lab humidity fluctuating between 48% ~ 64% throughout the experiment and monitored the bending of the EHI strips

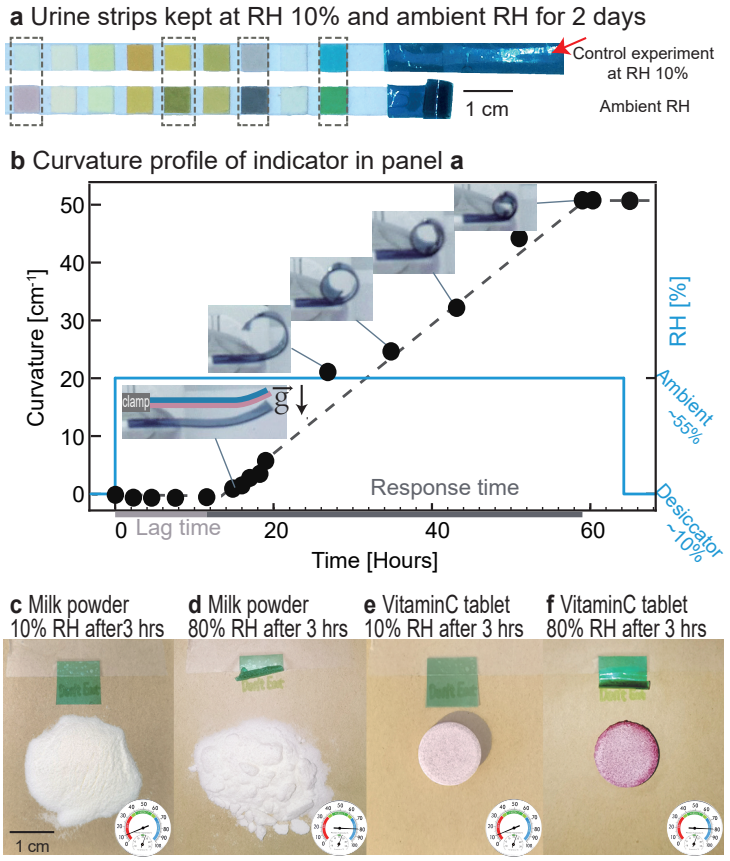

Figure 4.2: The demonstration on how EHI (pointed by red arrow) reports exposure to the elevated humidity by mechanical deformation. Panel (a) presents two EHIs-attached urine strips stored under different humidity conditions after 2 days. After two days, the ability of the strips to fulfill their function is validated by identical artificial urine solutions. The strip at the top is the control sample stored at the recommended humidity level of 10 % RH gives the correct reading. However, the strip at the bottom, which is exposed to ambient conditions (fluctuating between 48 and 64 % RH), gives a false reading evident from color change distinct from the control (highlighted in grey). Panel (b) shows the curvature development of the EHI attached to the urine strip exposed to undesired ambient humidity conditions in panel a bottom. The dashed line is a guide for the eye. (c) Milk powder: 10% RH, 3 hours in desiccator.(d) Milk powder: 80% RH, 3 hours. (e) Vitamin C tablet: 10% RH, 3 hours in desiccator. (f) Vitamin C tablet: 80% RH, 3 hours. Moisture exposure diagnosed by rolled EHI while no EHI bending in control (desiccator-stored) experiments.

(Figure 4.2(a), bottom). The humidity-exposed urine strip with EHI attached is compared to the control sample kept at recommended 10% RH at room temperature (Figure 4.2(a), top). The control urine strip and exposed urine strip were afterward dipped in identical artificial urine solutions. The EHI exposed to ambient humidity rolls on itself, informing of undesired exposure to high humidity, while EHI in the control sample remained unaltered. Moreover, the control sample kept at 10% RH accurately measures the contents of artificial urine, but the exposed sample produces false readings. The bending is quantified by measuring the curvature (inverse radius, insets in Figure 4.2(b)) of the bend bilayer EHI extracted from time-lapse images of EHI. Within a response time of 47 hours, the curvature of the rolled EHI developed from 0 to 50 cm^{-1} after a lag time of approximately 13 hours. After humidity exposure, the curvature remained even though the urine strip was put back into the desiccator where the RH was 10%. Furthermore, EHI successfully diagnosed the exposure to humidity for two humidity-sensitive products, milk powder and Vitamin C tablet. The products and EHIs were kept at 80% RH for 3 hours while the control sample is kept in a desiccator. The EHIs in humidity-exposed samples bent and rolled on themselves while the control sample remained flat (Figure 4.2(c)). To sum up, EHIs can identify a perishable product that has been once exposed to high humidity by irreversible bending and rolling. A video of the bending and rolling with more details is also provided in Supporting Information (Supplementary movie C.S1, which can be accessed by scanning the QR code provided in the Appendix). In addition, other EHI applications, i.e., pharmaceutical tablets and cashew nut under 80% RH can be found (see Figure C.S5 in the Appendix).

As different products degrade in distinct time scales, the broader applicability of EHI hinges on the tunability of the lag time and response time. The bending/rolling mechanism needs to be understood not just out of scientific interests but also from an engineering interest to benefit EHI design.

4.3.2 Rolling mechanism

4.3.2.1 *TGA result*

As HGF (blue) has higher water absorption ability compared to LGF (pink), the EHI should have bent towards LGF if the bending mechanism was based solely on compressive stresses induced by layer swelling more. Nevertheless, the observed bending direction contradicts this initial expectation. More interestingly, scanning electron microscopy images revealed that the LGF of EHI bilayer elongated more than HGF after two weeks of storage outside the desiccator at ambient humidity conditions (see Figure C.S3 in the Appendix). Hence, we rationalize that a different physical mechanism should be in play.

To shed light on the mechanism behind bending and consequent rolling of the EHI on itself, we conducted thermogravimetric analysis (TGA) on various films: a bilayer EHI(1), a single HGF(2), and a single LGF(3) (Figure 4.3(a)). Prior to TGA the films were exposed to humidity. To accelerate the lag time, the conditioning of the single layers is at 50% RH instead of 10%. To amplify the water absorption and TGA results we performed the test at 80% RH. After 48 hours of exposure to 80% RH, the bilayer EHI(1) is separated manually by physically separating into HGF (bilayer, 1a) and LGF (bilayer, 1b). The TGA profiles of these films are obtained (Figure 4.3(b)). A pure caseinate film is also studied under the same condition to identify glycerol. Specific decomposition temperatures are also provided (Table C.S1 in the Appendix).

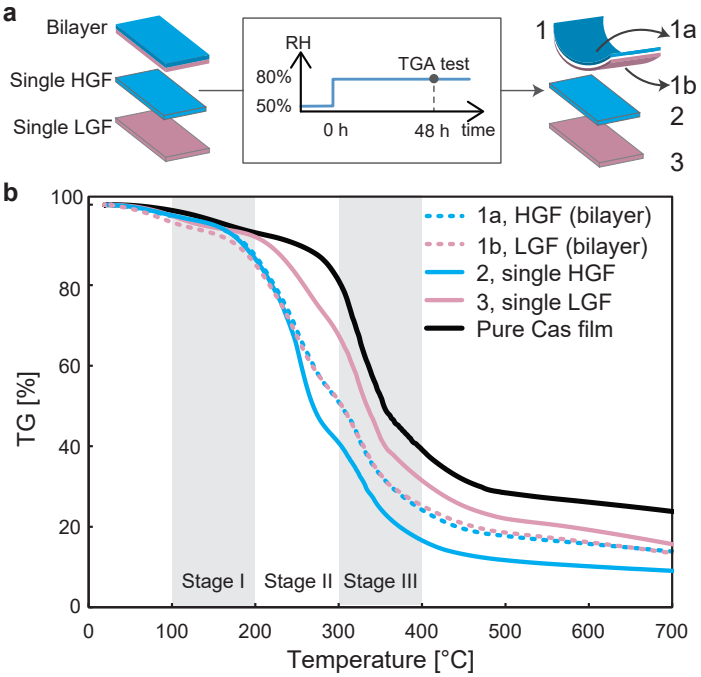

Figure 4.3: (a) The humidity exposure history and the referred name of various caseinate/glycerol films. (b) The TGA profiles of the tested films.

TGA profiles show three distinct regimes. In stage I (100 to 200 °C), water evaporation induced a similar mass loss trend in all the samples. Stage III, from around 300 °C, is the decomposition of sodium caseinate, leaving 30% residue at 700 °C. In stage II, where the part of our interest lies, we found that films 1a and 1b show an identical trend after the humidity exposure, indicating that the compositions of these two films are identical. Therefore, it is rationalized to hypothesize that glycerol diffused from HGF to LGF after humidity exposure, considering that glycerol is the only chemical that decomposes within stage II.

4.3.2.2 *Hypothesis for bending and rolling mechanism*

Based on the TGA observations, we propose a rolling mechanism that involves the adsorption of condensed water from the environment and subsequent the counter diffusion of glycerol and water across the bilayer. The hypothesized mechanism (Figure 4.4) is illustrated to rationalize the macroscopic observations of bending and consequent rolling direction as well as observed lag and response time.

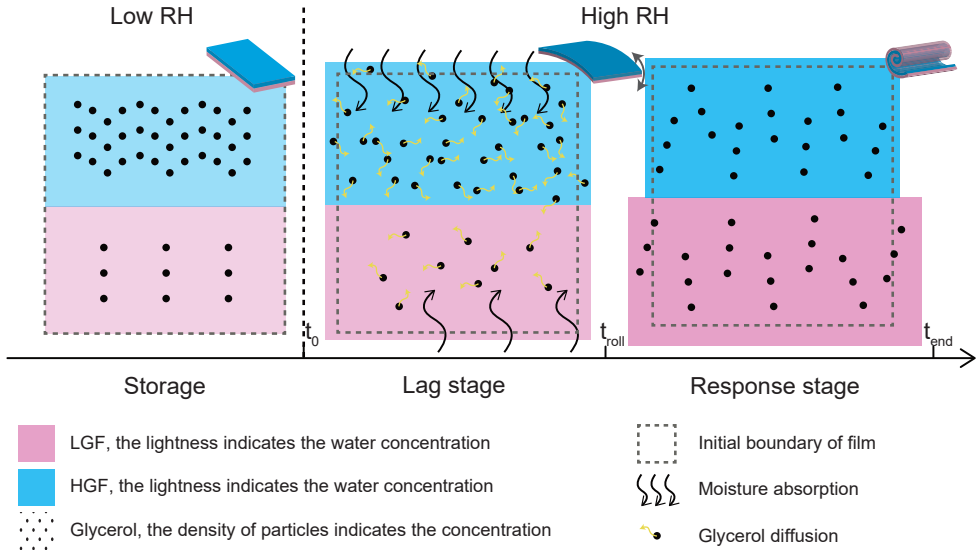

Figure 4.4: The proposed mechanism of rolling. Geometry and time are not drawn in scale.

During the *Storage stage* (at *Low RH*), LGF and HGF absorb a limited amount of water. Glycerol is constrained in each layer at this stage since the caseinates are densely packed and the glycerol diffusion is considered extremely slow. Therefore, the EHI is capable of maintaining its flat shape for a relatively long time under 10% RH. In fact, as already mentioned, the EHI can maintain its shape for at least 15 days when subjected to low relative humidity (10% RH) (see Figure C.S4 in the Appendix). This implies that the EHI is stable and reliable within our observation period, and its shape will not be affected until it is exposed to a relatively high level of humidity. Shelf stability should be further investigated and adjusted based on the shelf life of the product, and EHIs will be implemented.

At t_0 when humidity is introduced, both films start to absorb moisture and exhibit hygroscopic swelling. In this stage which we term as *lag stage*, we speculate that the films absorb more water and exhibit a volumetric change compared to the initial volume. As previously mentioned, the high concentration of glycerol in HGF tends to bond more water, there is a larger volume change in HGF (ΔV_{HGF}) compared to that of LGF (ΔV_{LGF}). On the macro scale, the bilayer firstly bends towards LGF with HGF as outer while LGF

as inner consistently (Supplementary movie C.S1, which can be accessed by scanning the QR code provided in the Appendix). However, since the network of the caseinate film is expanded by the absorbed moisture, the glycerol molecules from this moment can move from HGF to LGF due to the concentration gradient. We hypothesize that moisture uptaking and glycerol diffusion along with water diffusion lead to a competition in volume change between LGF and HGF ($\Delta V_{LGF} \approx \Delta V_{HGF}$). On the macro scale, we hypothesize the lag time observed is due to the time required for the condensed water to penetrate the glassy network.

In the *Response stage*, the bulk volume of each layer further expands, hence the caseinate proteins are loosely packed and the size of the pores within the caseinate network further grows. As a result, glycerol in this stage diffuses significantly from HGF to LGF. Furthermore, water absorbed by the HGF migrates to LGF accompanied by glycerol diffusion. These two factors henceforth help LGF eventually wins the competition in the volumetric increase ($\Delta V_{LGF} >> \Delta V_{HGF}$) and lead the bilayer to roll up with the LGF as outer along with HGF as inner [45] on the macro scale.

Moreover, interface effects such as the formation of a thick skin layer due to enhanced evaporation at corners and at the interface may alter local microstructure in EHI. The altered crust skin may slow down the diffusion of water consequently time scale of bending.

After *Response stage*, the counter diffusion of glycerol and water reaches equilibrium, and the two layers become identical in composition as supported by TGA results. The rolling of EHI on itself stops since there is no concentration gradient that can drive the dilatation. Similarly, since the bending and rolling are proposed to be driven by glycerol diffusion, the process cannot exhibit reversibility because there is no glycerol concentration difference in the equilibrium bilayer to provide the necessary driving force.

4.3.3 Tunability

It is crucial to engineering the EHI response, namely, the lag time, response time, and final curvature of rolling, to match the characteristic time scale of decomposition/degradation of the labeled products. In this section, we will demonstrate that the EHI response can be tuned by simply adjusting the layer thickness and aspect ratio.

4.3.3.1 *Tunability of lag time and response time*

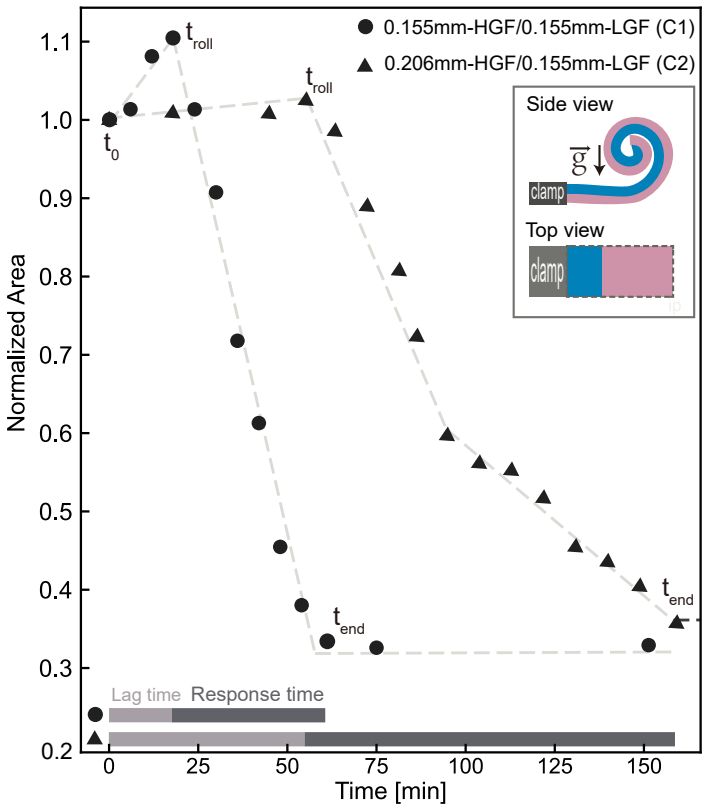

Figure 4.5: Normalized area (Projected area/Initial area) of EHIs as a function time for two representative EHIs with different layer thicknesses. The thickness of the films making up the EHIs are 0.155 mm-HGF/0.155 mm-LGF (C1, dots) and 0.206 mm-HGF/0.155 mm-LGF (C2, triangles), respectively. The films are conditioned at 50% RH as single layers for 24 hours, stuck together and tested at 80% RH. The measurement parameters are shown in the insert. Dash lines are a guide for the eye.

The tunability of lag time and response time through layer thickness is showcased by two EHIs with different thicknesses, i.e., 0.155 mm-HGF/0.155 mm-LGF (Figure 4.5, C1, dots) and 0.206 mm-HGF/0.155 mm-LGF (Figure 4.5, C2, triangles). The single layers are conditioned at 50% RH for 24 hours before being stuck together and tested at 80% RH. Under 80% RH EHI rolls on itself with a nearly constant curvature by forming a spiral at the end as sketched in the insert. For this reason, *Normalized Area*, i.e., Projected area/Initial area, instead of the curvature, is given to represent the rolling behavior. The projected area is highlighted by the grey dash line (Figure 4.5).

The lag time of the thinner EHI combination (C1, dots, 0.155 mm-HGF/0.155 mm-LGF) is 25 min. It exhibits a linear rolling behavior in line with earlier presented results, that is completed within 30 min. The rolled structure is maintained after 150 min. For the thicker combination (C2, triangles, 0.206 mm-HGF/0.155 mm-LGF), the lag time is 60 min meanwhile it takes around 90 min to complete rolling. By increasing around 30% of HGF thickness, both the lag time and response time are doubled. We can attribute this longer operation time to two reasons. First, a thicker film spends more time reaching the swollen equilibrium state. Secondly, the thicker combination, due to its reduced flexibility[37], has a tendency to bend at a slower pace, resulting in a longer response time when compared to the thinner combination. Similar to C1, C2 also holds its final structure after t_{end} (data not shown in the figure). Both C1 and C2 show a normalized area increase during the lag stage. This increase in the area could be attributed to the films swelling when they absorb moisture, as we already discussed (Figure 4.4).

However, the device is considered versatile due to the ability to easily tune its lag time and response time through layer thickness, making it suitable for various applications where the humidity changes slowly or infrequently over a longer period of time, such as monitoring humidity trends in a climate-controlled environment such as storage room. The response time varies from 90 to 150 minutes in the showcased combinations. While this showcased response time may not be ideal for applications requiring real-time response, it is suitable for warning users of slowly evolving humidity-triggered processes such as bacterial or mold growth which typically requires multiple hours to a few days based on environmental conditions and biological species.

4.3.3.2 *Tunability of final curvature*

The aspect ratio has already been consistently reported to influence the bending conformation (i.e. it dictates whether a bilayer structure rolls along long or short edge) for other bilayer systems [36, 46–48]. However, contradicting results exist in the literature regarding the quantitative relationship between aspect ratio and final bending curvature. Stoychev et al. [36], Wang et al. [49], and Abdolahi et al. [50] found the bending curvature of the free-standing hydrogel bilayer is independent of the aspect ratio, which agrees with Timoshenko's theory [51]. However, Kim et al. [52] observed a strong dependence between aspect ratio and bilayer bending. Moreover, multiple-rolling has been observed exclusively under the condition of a large aspect ratio by Alben, Balakrisnan, and Smela [46]. We already found that at 50% RH all our EHIs roll to a radius of around 2.5mm regardless of aspect ratio (see Figure C.S6 in the Appendix), where the rolling degree can be considered uniform within experimental limits. In this study, the relationship between the aspect ratio and the curvature of rolled EHI attains is further investigated for EHIs conditioned at 50% RH and exposed to 80% RH. The results are summarized (Figure 4.6).

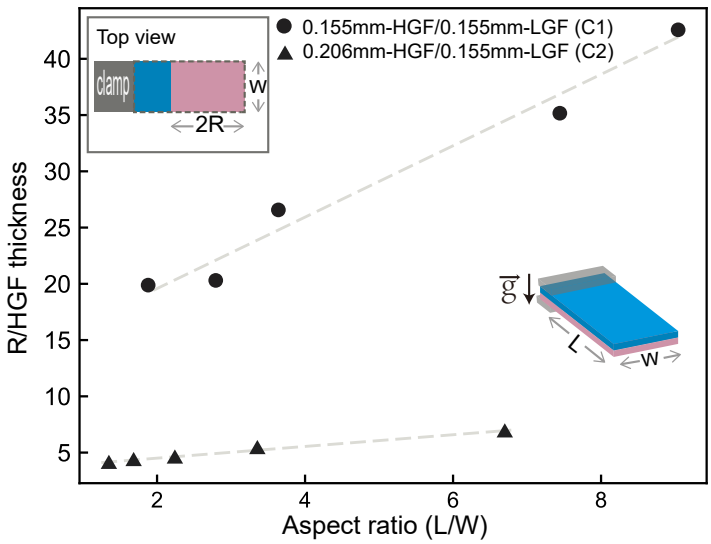

Figure 4.6: Final radius of the rolled EHI normalized by the thickness of HGF layer as a function of aspect ratio for EHIs with different layer thickness combinations. The thickness combinations of the EHIs are 0.155 mm-HGF/0.155 mm-LGF (C1, dots) and 0.206 mm-HGF/0.155 mm-LGF (C2, triangles), respectively. The films are conditioned at 50% RH and tested at 80% RH. The measured parameters from the final rolled EHI are schematically shown in the insert. The grey dash line is the linear fitting.

As the aspect ratio influences the bending conformation, to be more specific, bilayers will bend into a shape that minimizes resistance to bending in an energetically preferred way [52]. In this study, we only focus on the final curvature the rolled EHI attains because bending conformation is less critical for humidity interpretation according to our observations. To eliminate certain conformations, the short edge of EHI is attached to a solid object. When the short edge is fixed by a clamp, EHI looks like a cantilever beam, and the bending occurs along the long edge.

EHIs of two distinct thicknesses (both C1 and C2) were prepared in various aspect ratios, conditioned under 50% RH, and exposed to 80% RH. The final shape of the rolled EHI is characterized by radius (R) as illustrated in the insert. We further normalize the radius with the thickness of the HGF of EHI to ensure that we have a dimensionless graph (Figure 4.6). Interestingly, there is a clear linear correlation between $R/\mathrm{HGF\,thickness}$ and the aspect ratio l/w appeared. The coefficient of determination ($R^2 \approx 0.97$ for C1 and $R^2 \approx 0.99$ for C2) indicates a reasonably strong, positive linear correlation between non-dimensionalized R and aspect ratio. Since the length and the HGF layer thickness are fixed while the width is varied in this set of tests, we can also put it in a direct way, i.e., the final rolling radius is larger for a smaller width. It can be seen that C2 (the thicker combination, 0.206 mm-HGF/0.155 mm-LGF) overall shows a smaller R, which is within expectation considering that the larger total amount of glycerol transporting from HGF to LGF can induce more pronounced swelling in LGF in C2 compared to C1. Moreover, when we compare the two slopes of C1 and C2, it is evident from the observation that the aspect ratio exerts a more substantial effect on the final radius of rolled bilayer EHI in thinner C1 compared to C2.

It is concluded that in this caseinate/glycerol bilayer, the final size of the roll is influenced by the width of EHI under a higher humidity level, namely 80% RH. A similar observation was also found in micromachined polysilicon/chromium bilayer cantilever [53]. At this moment, we can not offer a quantitative theory explaining this observation, yet we speculate that the torque generated by the clamp along the width possibly plays a role in this phenomenon. The reason that the aspect ratio only influences the radius of the final shape under 80% is unclear to us at the moment. As discussed previously, we hypothesize that the bending of the EHI is initiated by glycerol diffusion along with water migration. During exposure to humidity, the water and glycerol molecules diffuse between layers until they reach the equilibrium state. The volume of each layer is also altered dynamically during this process. Therefore, we rationalize that adoption of Timoshenko's theory or the modified equation from Reyssat and Mahadevan [51] is not possible for EHIs conditioned at 50% RH then exposed to 80% RH where diffusion.

4.4 Conclusion

We developed a caseinate/glycerol based food-grade hence edible humidity indicator that informs of undesired humidity exposure by irreversible mechanical bending. Once exposed to higher humidity, EHI deforms and rolls on itself, informing the users of exposure to humidity. We characterized the rolling time and final geometry of EHI when exposed to high humidity levels as a function of EHI thickness and aspect ratio respectively. Moreover, the application of EHI has been demonstrated with a humidity-sensitive medical test kit, pharmaceutical tablets, milk powder, etc. We proposed a rolling mechanism coupling hygroscopic swelling, glycerol diffusion, and water diffusion. This mechanism is substantiated by TGA and guides us to tune the lag time and response time by manipulating the layer thickness. Meanwhile, the final curvature of the rolled EHI is shown to depend on the aspect ratio under 80% RH. However, when EHI is applied to label products in real life, one should take temperature variations into account since it affects diffusion. This is not addressed in this study but is worth investigating in the future. Overall, the developed indicator shows the potential to detect perishable products exposed to unsuitable humidity levels by deforming irreversibly upon humidity exposure. The indicator's ability to deform in reaction to humidity also renders it appropriate as a humidity-activated actuator, especially in scenarios where it is essential to uphold low humidity levels.

REFERENCES

[1] United States Department of Agriculture Food Safety and Inspection Service. *Food Product Dating*. Tech. rep. 2019.

[2] European Commission. *Date marking and food waste*. Tech. rep. 2018.

[3] H. Yousefi et al. "Intelligent food packaging: A review of smart sensing technologies for monitoring food quality." *ACS sensors* 4.4 (2019), pp. 808–821.

[4] H. Hong, J. M. Regenstein, and Y. Luo. "The importance of ATP-related compounds for the freshness and flavor of post-mortem fish and shellfish muscle: A review." *Critical Reviews in Food Science and Nutrition* 57.9 (2017), pp. 1787–1798.

[5] G. Fuertes et al. "Intelligent packaging systems: sensors and nanosensors to monitor food quality and safety." *Journal of Sensors* 2016 (2016), pp. 1–8.

[6] M. Mataragas, V. C. Bikouli, M. Korre, A. Sterioti, and P. N. Skandamis. "Development of a microbial Time Temperature Indicator for monitoring the shelf life of meat." *Innovative food science & emerging technologies* 52 (2019), pp. 89–99.

[7] B. Hu et al. "Development of a novel Maillard reaction-based time–temperature indicator for monitoring the fluorescent AGE content in reheated foods." *RSC Advances* 10.18 (2020), pp. 10402–10410.

[8] C. T. Santos, P. Veiga-Santos, P. Sestari, N. C. Sorrini, and R. de Oliveira Roça. "Protein time–temperature sensor for intelligent starch polymers." *Journal of Food Processing and Preservation* 44.5 (2020), e14428.

[9] G. Lanza, J. Perez-Taborda, and A Avila. "Time temperature indicators (TTIs) based on silver nanoparticles for monitoring of perishables products." *Journal of Physics: Conference Series*. Vol. 1247. 1. IOP Publishing. 2019, p. 012055.

[10] X. Meng, S. Kim, P. Puligundla, and S. Ko. "Carbon dioxide and oxygen gas sensors-possible application for monitoring quality, freshness, and safety of agricultural and food products with emphasis on importance of analytical signals and their transformation." *Journal of the Korean Society for Applied Biological Chemistry* 57.6 (2014), pp. 723–733.

[11] A. Nopwinyuwong, S. Trevanich, and P. Suppakul. "Development of a novel colorimetric indicator label for monitoring freshness of intermediate-moisture dessert spoilage." *Talanta* 81.3 (2010), pp. 1126–1132.

[12] N. Wells, D. Yusufu, and A. Mills. "Colourimetric plastic film indicator for the detection of the volatile basic nitrogen compounds associated with fish spoilage." *Talanta* 194 (2019), pp. 830–836.

[13] H.-N. Chun, B. Kim, and H.-S. Shin. "Evaluation of a freshness indicator for quality of fish products during storage." *Food science and biotechnology* 23.5 (2014), pp. 1719–1725.

[14] M. Smolander et al. “Myoglobin-based indicators for the evaluation of freshness of unmarinated broiler cuts.” *Innovative Food Science & Emerging Technologies* 3.3 (2002), pp. 279–288.

[15] M. E. Helgeson, S. C. Chapin, and P. S. Doyle. “Hydrogel microparticles from lithographic processes: Novel materials for fundamental and applied colloid science.” *Current opinion in colloid & interface science* 16.2 (2011), pp. 106–117.

[16] I. Rehor et al. “Biodegradable microparticles for simultaneous detection of counterfeit and deteriorated edible products.” *Small* 13.39 (2017), p. 1701804.

[17] Y. C. Saraswat et al. “Shape anisotropic colloidal particle fabrication using 2-photon polymerization.” *Journal of colloid and interface science* 564 (2020), pp. 43–51.

[18] M. Zhang, T. Warth, N. Boon, A. F. Demirörs, and H. B. Eral. “Microfluidic Synthesis of Hydrogel Microparticles with Superparamagnetic Colloids Embedded at Prescribed Positions for Anticounterfeiting Applications.” *Advanced Materials Interfaces* (2022), p. 2200899.

[19] S. Reddy, S Girisham, and G. N. Babu. *Applied Microbiology (agriculture, environmental, food and industrial microbiology)*. Scientific Publishers, 2017.

[20] K. Wright. *The Effects of Humidity on Pharmaceuticals*. 2018.

[21] J. F. Thompson et al. “DryCard TM—A Low-Cost Dryness Indicator for Dried Products.” *AIMS Agriculture and Food* 2.4 (2017), p. 339.

[22] N. Bumbudsanpharoke, S. Kwon, W. Lee, and S. Ko. “Optical response of photonic cellulose nanocrystal film for a novel humidity indicator.” *International journal of biological macromolecules* 140 (2019), pp. 91–97.

[23] A. T. Jafry, H. Lim, W.-K. Sung, and J. Lee. “Flexible time–temperature indicator: a versatile platform for laminated paper-based analytical devices.” *Microfluidics and Nanofluidics* 21.3 (2017), p. 57.

[24] R. Snyder et al. “Shape memory polymer sensors for tracking cumulative environmental exposure.” 7645 (2010), p. 76450C.

[25] D. J. Paustenbach, B. E. Tvermoes, K. M. Unice, B. L. Finley, and B. D. Kerger. “A review of the health hazards posed by cobalt.” *Critical reviews in toxicology* 43.4 (2013), pp. 316–362.

[26] D. Bridgeman, J. Corral, A. Quach, X. Xian, and E. Forzani. “Colorimetric Humidity Sensor Based on Liquid Composite Materials for the Monitoring of Food and Pharmaceuticals.” *LANGMUIR* 30.35 (2014), pp. 10785–10791.

[27] K. Mishra et al. “Ionic Liquid-Based Polymer Nanocomposites for Sensors, Energy, Biomedicine, and Environmental Applications: Roadmap to the Future.” *Advanced Science* 9.26 (2022), p. 2202187.

[28] C. Esteves et al. “Tackling Humidity with Designer Ionic Liquid-Based Gas Sensing Soft Materials.” *Advanced Materials* 34.8 (2022), p. 2107205.

[29] K. Wu et al. “A humidity sensor based on ionic liquid modified metal organic frameworks for low humidity detection.” *Sensors and Actuators B: Chemical* 355 (2022), p. 131136.

[30] X. Zhao et al. “Hydrophobic ionic liquid-in-polymer composites for ultrafast, linear response and highly sensitive humidity sensing.” *Nano Research* 14.26 (2021), pp. 1202–1209.

[31] S.-J. Park, J.-Y. Jeon, and T.-J. Ha. “Wearable humidity sensors based on bar-printed poly (ionic liquid) for real-time humidity monitoring systems.” *Sensors and Actuators B: Chemical* 354 (2022), p. 131248.

[32] S. K. Pankaj et al. “Physicochemical characterization of plasma-treated sodium caseinate film.” *Food research international* 66 (2014), pp. 438–444.

[33] N. Sarigul, F. Korkmaz, and İ. Kurultak. “A new artificial urine protocol to better imitate human urine.” *Scientific reports* 9.1 (2019), pp. 1–11.

[34] M. R. Khan et al. “Active casein coatings and films for perishable foods: structural properties and shelf-life extension.” *Coatings* 11.8 (2021), p. 899.

[35] J.-L. Audic, F. Fourcade, and B. Chaufer. “Biodegradable material obtained from renewable resource: Plasticized sodium caseinate films.” *Thermodynamics, Solubility and Environmental Issues*. Elsevier, 2007, pp. 369–382.

[36] G. Stoychev, S. Zakharchenko, S. Turcaud, J. W. Dunlop, and L. Ionov. “Shape-programmed folding of stimuli-responsive polymer bilayers.” *ACS nano* 6.5 (2012), pp. 3925–3934.

[37] J. He et al. “Highly efficient actuator of graphene/polydopamine uniform composite thin film driven by moisture gradients.” *Advanced Materials Interfaces* 3.14 (2016), p. 1600169.

[38] D. Morales, B. Bharti, M. D. Dickey, and O. D. Velev. “Bending of Responsive Hydrogel Sheets Guided by Field-Assembled Microparticle Endoskeleton Structures.” *Small* 12.17 (2016), pp. 2283–2290.

[39] Y. Feng, J. Xu, S. Zeng, Y. Gao, and J. Tan. “Controlled helical deformation of programmable bilayer structures: design and fabrication.” *Smart Materials and Structures* 29.8 (2020), p. 085042.

[40] M. Chen et al. “Polybenzoxazole nanofiber-reinforced moisture-responsive soft actuators.” *Scientific reports* 7.1 (2017), pp. 1–10.

[41] M. Jamal et al. “Bio-origami hydrogel scaffolds composed of photocrosslinked PEG bilayers.” *Advanced healthcare materials* 2.8 (2013), pp. 1142–1150.

[42] A Le Duigou and M Castro. “Moisture-induced self-shaping flax-reinforced polypropylene biocomposite actuator.” *Industrial Crops and Products* 71 (2015), pp. 1–6.

[43] cobas. *Compendium of urinalysis - Urine test strips and microscopy*. Tech. rep. 2010.

[44] M. J. Pugia and C. T. Zimmerle. *Device and method for detection of analytes*. Tech. rep. 2016.

[45] S. Naficy, R. Gately, R. Gorkin III, H. Xin, and G. M. Spinks. “4D printing of reversible shape morphing hydrogel structures.” *Macromolecular Materials and Engineering* 302.1 (2017), p. 1600212.

[46] S. Alben, B. Balakrisnan, and E. Smela. “Edge effects determine the direction of bilayer bending.” *Nano letters* 11.6 (2011), pp. 2280–2285.

[47] S. Alben. “Bending of bilayers with general initial shapes.” *Advances in Computational Mathematics* 41.1 (2015), pp. 1–22.

[48] J. Guo et al. “Bidirectional and biaxial curving of thermoresponsive bilayer plates with soft and stiff segments.” *Extreme Mechanics Letters* 16 (2017), pp. 6–12.

[49] X. Wang et al. “Multi-Responsive Bilayer Hydrogel Actuators with Programmable and Precisely Tunable Motions.” *Macromolecular Chemistry and Physics* 220.6 (2019), p. 1800562.

[50] J. Abdolahi, M. Baghani, N. Arbabi, and H. Mazaheri. “Analytical and numerical analysis of swelling-induced large bending of thermally-activated hydrogel bilayers.” *International Journal of Solids and Structures* 99 (2016), pp. 1–11.

[51] E. Reyssat and L. Mahadevan. “Hygromorphs: from pine cones to biomimetic bilayers.” *Journal of the Royal Society Interface* 6.39 (2009), pp. 951–957.

[52] J. Kim et al. “Reversible self-bending soft hydrogel microstructures with mechanically optimized designs.” *Chemical Engineering Journal* 321 (2017), pp. 384–393.

[53] M. T.-K. Hou and R. Chen. “Effect of width on the stress-induced bending of micromachined bilayer cantilevers.” *Journal of Micromechanics and Microengineering* 13.1 (2002), p. 141.

5

TIME-TEMPERATURE INDICATOR

This chapter is based on the manuscript:
Zhang, M., Yunus, A.M.R., Menon, S.V., Mok, A., Hinderink, E., Eral, H. B., Food grade time-temperature indicator made of purple pitaya embedded alginate for perishable products, to be submitted.

5.1 Introduction

Ensuring access to safe food is of utmost importance in our daily lives. Typically, consumers rely on the shelf life date or best-by date printed on the packaging to assess the food's quality. However, various factors, particularly temperature fluctuations, throughout the supply chain during storage and transportation can significantly distort the accuracy of these dates[1]. Improper storage of perishable products such as food and medicines can have serious consequences, leading to either wastage or poisoning upon the product deterioration or undesired bacterial growth. Shockingly, each year, up to 10% of the 88 million tonnes of food waste generated in the EU is attributed to issues related to date marking [2], and the unfortunate truth is that half a million people lose their lives due to food poisoning [3]. These challenges are particularly prevalent in underdeveloped areas with inadequate infrastructure, where limited refrigeration facilities, unreliable power supply, and inadequate transportation networks hinder the effectiveness of cold chains. However, it's important to note that even in more advanced areas, the effectiveness of cold chains can be compromised by human error, improper handling practices, or a lack of training.

In the pursuit of improving the diagnosis of storage conditions for perishable and temperature sensitive products, researchers are working on the development of time-temperature indicators (TTI). These indicators aim to continuously monitor and reflect the temperature history of the products, providing accessible visual information that can be understood by consumers [4]. The communication between end-users and TTIs is typically achieved through mechanical or chromic means, utilizing chemical, physical, or biological principles [1]. Chemical TTIs, for example, rely on cumulative chemical changes due to time and temperature, such as photochromic or oxidation reactions [1]. Physical TTIs involve changes in physical properties like diffusion, thermochromism, or photoacoustic lattice changes [5]. Biological TTIs, on the other hand, utilize enzyme reactions or lactic acid reactions [1].

Despite recent advancements, the widespread implementation of TTIs in the market has not yet been realized. An effective TTI should meet several standards. Firstly, it should demonstrate a clear change in response to temperature, allowing for the display of temperature history. Secondly, it should accurately diagnose temperature issues. Thirdly, it should be unaffected by external factors such as light, pH, enzymatic reactions, bacteria, ambient gas composition, humidity, electromagnetic interference, or labeled products. Last but not least, a TTI should be safe for use with labeled products.

Unfortunately, to the best of our knowledge, there is currently no TTI that is considered safe for direct contact with perishable products, especially for oral consumption. These TTIs are typically placed on the outer surface of heat-sensitive product packages, only monitoring the conditions of package ambiance but not the perishable products themselves [6]. This poses a significant challenge in accurately interpreting temperature abuses.

On the other hand, most TTIs have a narrow operating temperature range. For instance, the biological TTIs are only applicable to the room temperature range within which the enzyme reaction is optimal[7–10]. Meanwhile, the chemical TTIs utilizing the Maillard reaction can only exhibit change when the temperature is higher than 70 °C[11–13]. Physical TTIs, such as diffusion-driven indicators, can be customized for specific operating temperatures, but their complex structures, such as wicks and porous cells, pose a risk of malfunction and tend to be costly [6].

In this study, we present a novel time-temperature indicator (TTI) based on betacyanin-embedded alginate beads. These thermochromotic indicator beads utilize betacyanin extracted from purple pitaya fruit and edible alginate, Owing to their food-grade nature, these TTIs can be placed in direct contact with perishable products with no risk of contamination upon oral consumption as opposed to commercially available TTIs. This edible TTI demonstrates an irreversible thermochromic change, transitioning from purple to yellow, over a wide operating temperature range. Additionally, by manipulating the pH value of the beads, we can tune how fast TTI's color changes hence a broad range of spoilage kinetics spanning hours to days can be covered. Considering that meat and seafood are commonly packaged in modified atmospheres, we also investigated the impact of varying carbon dioxide (CO_2) and oxygen (O_2) concentrations on the thermochromic reaction within the beads. The results showed consistent color spectrum evolution from purple to yellow regardless of covered gas content, indicating the applicability of this edible TTI across different gas compositions.

5.2 Materials and methods

5.2.1 Fabrication of pitaya extracts and alginate-based TTI

2 g of freeze-dried purple pitaya powder (The Glow Lab) is mixed in 50 ml of water (18.2 MΩcm, Milli-Q). The mixture is magnetically stirred with a speed of 600 rpm for two hours at 40°C to infuse the color into the water. The mixture is then centrifuged for 15 minutes at 7400 rpm to separate the seeds and mucilage from the mixture [14]. The supernatant is then filtered to filter out the residual mucilage and seeds that fail to settle down using a filter paper (Whatman quantitative, ashless, GF/F 55 mm) to get the pitaya extracts. The pH is then adjusted by dissolving the necessary amounts of baking soda (Sodium bicarbonate, Arm & Hammer, E500ii) in the dye. Stock solutions of pitaya extract with various pH were ready to use.

For encapsulation in alginate, 5 ml of pitaya extract of the desired pH and 0.16 g of sodium alginate (CAS No. 9005-38-3, Food grade, Sigma Aldrich) is magnetically stirred for 30 minutes at room temperature to form a 3 wt% pitaya-alginate solution. The stirring is done at room temperature to reduce the degradation of the pitaya extract. The pitaya-

alginate solution is centrifuged at 7400 rpm for 15 minutes to eliminate bubbles in the solution. The solution is then added dropwise with a syringe into a 1 wt% calcium chloride (CAS No. 10043-52-4, Food grade, Merck) bath from a height of 1.2 cm with a needle of dimension 0.6*30mm. In the meantime, the calcium chloride bath is magnetically stirred at 400 rpm at room temperature to ensure the spherical shape of alginate beads. The beads were post-treated in the calcium chloride bath for 100 seconds to form a rigid shell. The beads are then rinsed with water and dried using tissues before being stored in vials to be frozen or refrigerated until further use.

5.2.2 Thermal behavior test under various pH conditions

Pitaya extract and alginate bead samples of pH 5,6,7 and 8 were fabricated for the thermal behavior study. Samples were set to temperature in an oven or refrigerator at a series of chosen temperatures, in particular, 4 °C, 23 °C, 40 °C, and 60 °C. Liquid samples were taken out at regular intervals for spectrophotometric measurement while the color change of beads is recorded in time-lapse video format to avoid the temperature fluctuations caused by the repeated oven door opening and closing.

Three sets of reversibility tests were conducted on the pH 8 sample as it is the most sensitive to heat. For the first set, the fresh samples were kept at -20 °C for 1 hour until it is totally frozen at first. After that, the samples were placed in the oven maintained at 23 °C or refrigerator at 4 °C for 24 hours. For the second testing set, the samples were kept at -20 °C for 24 hours and followed by heat treatment at 40 °C for 1 hour. Samples purged with N_2 to create an anaerobic environment were also studied. After purging for 1 hour at room temperature, the samples were kept at -20 °C for 24 hours and followed by heat treatment at 40 °C for 1 hour. All cycles were repeated twice, and the color change was recorded by the camera accordingly.

5.2.3 Colorimetric assay

CIELAB color system was adopted to measure the color. The total color difference can be quantified using ΔE as shown in Equation 5.1.

$$\Delta E = \sqrt{(L^* - L_o^*)^2 + (a^* - a_o^*)^2 + (b^* - b_o^*)^2} \tag{5.1}$$

Where, L^*, a^*, and b^* are the three parameters of the CIELAB color space coordinates. L^* denotes the lightness. a^* denotes red tones (positive value) and green tones (negative value). b^* denotes yellow tones (positive value) and blue tones (negative value). L_o^*, a_o^* and b_o^* are the colour space coordinates of the initial value.

Two different methods were used for the acquisition of the L^*, a^* and b^* value in this research. For liquid samples, spectrophotometric measurement (HACH DR600 UV-Vis

Spectrometer, CIELAB mode, number 2301) was applied at the wavelength of 535 nm. Alginate beads were first photographed in a lightbox (GT Commerce Photo studio photo box with LED lighting, 22x23x24 cm) and then analyzed through the Histogram Window of Adobe Photoshop CS6 as described by Yam and Papadakis[15].

5.2.4 Modified atmosphere test

Compressed air, nitrogen, and premixed gas (supplied by Linde-gas) were selected to compare the influence of the atmosphere. The premixed gas contains of 30% O_2, 40% CO_2 and 30% N_2. This specific ratio was chosen since it is commonly used in the food industry as a recommended gas mix for perishable food items such as chilled fish and seafood. Here the experiments of pH 8 pitaya extracts were performed at 60 °C for the accelerating purpose. The samples were filled in glass vials and purged with the selected gas for 1 hour. After that, samples are carefully sealed with parafilm and moved to the oven to test. A time-lapse video was recorded to avoid the temperature fluctuations caused by the repeated oven door opening and closing.

5.2.5 Plate count test of *L. casei Shirota*

As the indicator is used to determine heat abusage of *L. casei Shirota*, a plate counts test is carried out. *L. casei Shirota*, which is branded as Yakult, is pursued from a local supermarket. When pursued, the package from the freshest manufacture date is carefully chosen. The experimental procedure was carried out at the time intervals of 1 hour from 0 to 10 hours that maintained at 40 °C. 1 µL of *L. casei Shirota* samples were taken out from the unopened bottles and diluted by 10^6 with sterilized 0.85% NaCl solution and adequately mixed with a vortex mixer. The steel spreader (Sigma Aldrich) was used to spread the sample on the plate count agar (Merck Co.) and ensure uniform plating. The tip of the spreader was shown over a flame before being employed for the subsequent plating. Every test is repeated 3 times. Finally, the prepared plates were incubated at 37°C and 75% RH for two days. After the incubation period, the plates were taken out, and the mesophilic colonies were counted.

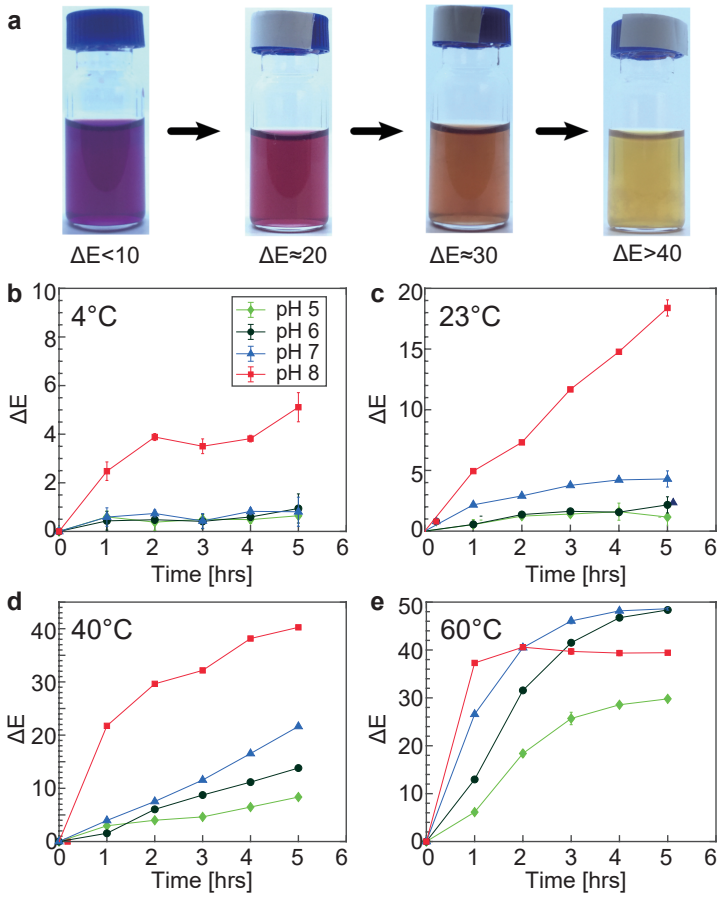

Figure 5.1: (a) Images of general color evolution of purple pitaya extract. Furthermore, color evolution is represented as ΔE as a function of time at (b) 4°C, (c) 23°C, (d) 40°C, (e) 60°C for the purple pitaya extract with pH values 5-8.

5.3 Results and discussion

5.3.1 Color evolution behavior of pitaya extracts

5.3.1.1 *Color evolution under various pH and operating temperatures*

Dye was extracted from the purple pitaya fruit with water and directly tested without any further purification, which has been described in section 5.2.1. In a nutshell, the freeze-dried purple pitaya powder is extracted using water at 40 °C. After centrifugation and filtration to remove the seeds of the pitaya, the matrix material sodium alginate and pH modifier baking soda are added to this pitaya extract at room temperature for 1 hour to get a well-dissolved pitaya-alginate solution. No procedure was conducted to purify the extracts further.

When exposed to heat, it demonstrates a gradual color change from purple to yellow. This color evolution was quantified using ΔE that was calculated from the CIELAB coordinates of the UV-VIS spectrometer results acquired hourly. The color evolution of the extract from purple to yellow and its correlation with the ΔE value is illustrated in Figure 5.1(a). The rich color variation is brought by the betacyanin group which is rich in purple pitaya. Purple pitaya is reported to have significantly higher betacyanin contents and hence benefit the desired tinctorial strength with reduced use amount[16]. The thermal sensitivity of betacyanin has already been extensively studied in the past decade. Betacyanin, a dye group of water-soluble phytochemical components, mainly contains betanin, phyllocactin, and hylocerenin[17]. Their chemical structures are shown in Figure D.S1 in the Appendix. The stability of betacyanin is reported to strongly depend on various factors such as temperature, pH, oxygen, etc.[18]. There are several possible pathways the betacyanin degrades due to thermal treatment. For instance, in an alkaline solution, betacyanin tends to degrade into bright yellow betalamic acid and colorless cyclo-Dopa through the hydrolysis of the aldimine bond in the absence of O_2. However, when O_2 is brought in, dehydrogenation will take place at the locations highlighted by the red dash line circle and produce a yellow neobetacyanin[19] as elucidated in Figure D.S1 in the Appendix. Furthermore, decarboxylation and deglycosylation are considered the main degradation pathways under acidic conditions[19, 20].

Figure 5.1(b-e) depicts the effect of pH and temperature on the color change which is represented as ΔE values. Four specific temperatures, namely 4°C, 23°C, 40°C, and 60°C are considerately selected because these values represent the typical temperatures of the fridge cell, room, hot summer, and scorching weather in tropical areas, respectively. These studied high temperatures fall into the temperature range of 8 to 63°C which is considered a "danger zone" by the food industry, where food is recommended not to be left out for more than 2 hours. Despite the limited duration of the test, which lasted only five hours, it is evident that the color evolution of pitaya extracts is strongly influenced by both the pH

value and temperature. Specifically, higher pH samples exhibited a faster color transformation at elevated temperatures. At lower temperatures, namely, 4°C and 23°C, non-alkaline pitaya extracts (pH 5, 6, and 7) show a nominal color change in the observed duration. We further increase the temperature to 40°C and 60°C, and visible transformations in color are finally able to be spotted in this short time window. For alkaline extracts (pH 8), it took almost 10 hours to get a yellow color (data not shown here) under 40 °C, however, this color change is seen within only two hours at 60°C.

We are not surprised that pH 8 extracts exhibit a greater color transformation. As aforementioned, the pH values from 5 - 7 are the stable pH range of the betacyanin pigments. Aldimine bond hydrolysis and dehydrogenation that are more susceptible to temperature effects tend to be provoked in a basic environment[19], should be responsible for the significant ΔE values observed across the lower temperature.

Our research findings indicate that the unpurified pitaya extracts, which naturally contain sugars, acids, antioxidants, and pectin substances[16, 18, 21], do not exhibit any side effects or effectively prevent color evolution. This aspect is particularly advantageous as it contributes to a low manufacturing cost of the Time-Temperature Indicator (TTI) since the purification process is often expensive. Furthermore, it is worth noting that this dye has remarkable temperature responsiveness, ranging from 4 to 100 °C. Figure D.S4 in the Appendix showcases the images of pitaya extract and its encapsulation form, TTI beads, work at 80 and 100 °C. To the best of our knowledge, this wide operating temperature range has not been reported before. We believe that this broad temperature range makes the TTI suitable for various real-life applications, covering the most common scenarios encountered.

5.3.1.2 *Irreversibility study*

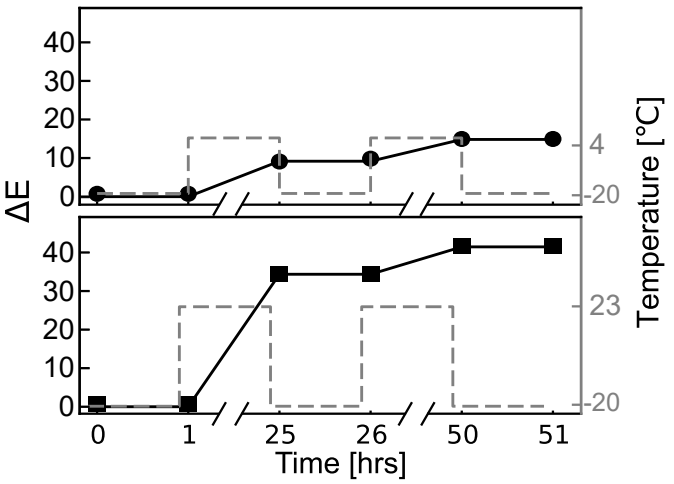

Figure 5.2: Irreversibility study showing the color change (ΔE) of the pH 8 pitaya extracts at 4°C and -20 °C (circle), 23°C and -20 °C (square) over two 24-hour cycles for 51 hours.

Irreversibility in color change is studied and summarized in this section. As shown in Figure D.S1 in the Appendix, the color evolution from purple to yellow is attributed to two pathways, i.e., the aldimine bond cleavage and dehydrogenation depending on the O_2 concentration in betacyanins. Specifically, a peculiarity of aldimine bond cleavage is its reversibility following a Schiff base condensation, where an amine reacts with carbonyl group to form an imine (-C=N-). In particular, after short-term heating, recondensation of betalamic acid and cyclo-Dopa derivatives to form the original betacyanins was reported, and the regeneration was observed at low temperatures such as 4 °C over 24 hours[22]. We have already demonstrated that our pH 8 pitaya extracts exhibit a subtle color alteration when exposed to a 4°C environment for 5 hours. We hypothesize that reversibility at this temperature is insignificant, as illustrated in Figure 5.1(b). Consequently, any concerns regarding reversibility when used with refrigerated products have been alleviated. However, in a scenario where the indicator developed is labeled for frozen products, the possible recondensation reaction of the betacyanin can lead to an incorrect reading during the final application. Hence, an irreversibility study in frozen conditions is essential.

The irreversibility study as shown in Figure 5.2 was conducted by freezing the pH 8 pitaya extracts for 1 hour at freeze temperature (-20°C) after 24 hours of heat exposure. Refrigeration temperature (4°C) and room temperature (23°C) were chosen as the canonical heat exposure temperatures. Meanwhile, a control experiment with the pH 8 pitaya extracts stored at -20°C over 51 hours was also conducted.

It can be observed from Figure 5.2 that after the initial 1-hour freezing and exposure to room temperature for 24 hours (square), the ΔE of extracts increased to around 34 as expected due to possible degradation pathways. Afterward, the sample was refrozen for 1 hour to simulate the accidental or intended experience of indicator to freezing temperature. No obvious reduction in ΔE was observed after this 1 hour. Subsequently, We further decreased the exposure temperature to 4°C (circle), still no reduction in ΔE was observed, which was evident that the freezing did not promote the recondensation reaction.

The irreversibility might be attributed to two reasons. The recondensation might be prohibited at the alkaline condition as reported by Herbach, Stintzing, and Carle[22]. Moreover, substituted cyclo-Dopa generated by the alkaline hydrolysis can further undergo oxidation at the available phenolic hydroxyl position leading to melanin-related molecules, or be deglycosylated by heat treatment [23]. Also, betalamic acid is reported to be heat sensitive and may undergo aldol condensation that leads to the generation of other components in the absence of oxygen [24]. Perhaps due to a combination of these reactions, the regeneration of betacyanin is hardly seen.

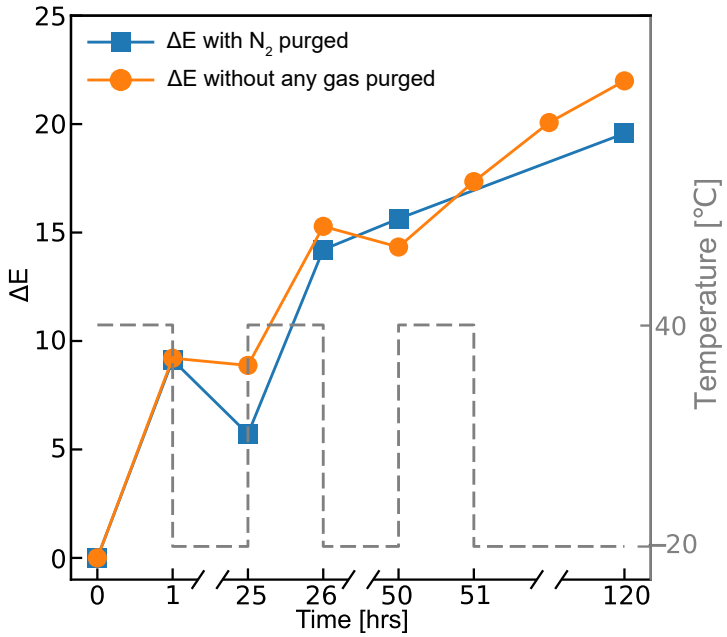

Figure 5.3: Irreversibility study showing the color change (ΔE) of the pH 8 pitaya extracts purged with N_2 (blue square) and no purge (orange circle) at 40°C for 1 hour and -20 °C for 24 hours over two 24 hours cycle followed with being kept at -20 °C for 72 hours.

We also have a concern that the heat exposure time and freeze time set in Figure 5.2 might be unfavorable to betacyanin regeneration. To address this concern, in the subsequent experiments, we increased the freeze time to 24 hours while shortening the heat

exposure time to 1 hour. To achieve a more pronounced color change, the heat exposure temperature was set to 40°C. The pH 8 pitaya extracts were subjected to three consecutive 24-hour cycles, followed by 72 hours of freezing (grey dashed line in Figure 5.3). The resulting color change (ΔE) is presented in Figure 5.3 (orange circle). For comparison, we also created an anaerobic atmosphere, indicated by the blue square in Figure 5.3.

Analyzing Figure 5.3, we observe a slight decrease in ΔE for both samples during the first cycle. However, it can still be concluded that once the betacyanin pigments in the pH 8 extract undergo thermal degradation, they do not recombine upon exposure to -20°C. This finding confirms that the indicator provides an accurate indication during the final application, despite the slight decrease in color change observed initially.

5.3.1.3 *Conformity under various atmosphere compositions*

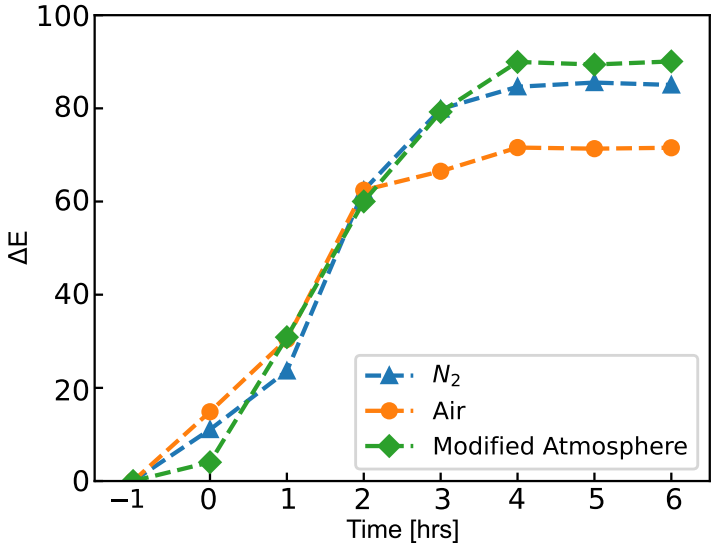

Figure 5.4: Variation of ΔE value with time at a temperature of 60 °C under various gas atmosphere.

It has been extensively reported that the atmosphere affects the degradation pathway of betacyanin[17–19, 22, 23]. For example, in the presence of oxygen, dehydrogenation will take place to form neobetanin (yellow) instead of alkaline hydrolysis into betalamic acid (bright yellow)[19]. In a scenario where the developed indicator is used for labeling fresh raw meat products, modified atmosphere packaging filled with various gas compositions is often applied to increase the shelf-life. Take a box of fresh raw beef for instance, O_2 is used to prevent anaerobic growth and maintain color, CO_2 to inhibit yeast, molds, and

microorganisms while N_2 to prevent package collapse [25]. Hence, a color change study under various atmosphere conditions is important.

Figure 5.4 displays the color change of pH 8 pitaya extracts at 60 °C that is purged with pure nitrogen, air (21% O_2 and 78% N_2), and modified atmosphere (30% O_2, 40% CO_2 and 30% N_2) respectively for 1 hour. Overall, a fast color change from purple to yellow happens as expected due to the high temperature (images can be found in Figure D.S6). The ΔE values all reach the maximum within 4 hours. However, the maximum ΔE of pitaya extracts purged with air (≈71) is relatively small compared to that of samples under nitrogen (≈85) and modified atmosphere (≈90). pH measurement (not shown here) proved that the extracts are acidified by the dissolved CO_2 from the modified atmosphere. Hence, the initial betacyanin concentration is probably well protected and results in a bigger color difference compared to the other two atmosphere systems. A bright yellow color that is speculated as the betalamic acid is noticed in the final N_2 purged sample, which is quantified via Photoshop as a relatively larger lightness value (L*, 64 compared to 53 for air and 58 for modified atmosphere) and perhaps causes higher maximum ΔE value when compare to air-purged samples.

To avoid any gas leakage from the packaging, we did not collect samples from the sealed vials for UV-vis spectrometer but time-lapse recorded the color change via camera and analyzed the color change in Adobe Photoshop (details can be found in the experimental section). It's important to note that different quantification methods may contribute to the observed higher ΔE values (>70) compared to Figure 5.1(e). Additionally, it is essential to consider that different lighting conditions can result in varying ΔE profiles. Moreover, the manual selection of the image acquisition window introduces some deviations, as the human eye is not adept at discerning subtle color differences with precision. In general, the exact maximum value of ΔE holds less significance as long as the noticeable change from purple to yellow can be observed by the naked eye. The subjective observation of color change is a more practical and reliable indicator in this context.

In summary, our findings suggest that different gaseous compositions may impact the degradation pathway of pitaya extracts, but they have minimal influence on the color change that is perceptible to the human eye. Therefore, it is deemed suitable for monitoring perishable products that are packaged in a modified atmosphere.

5.3.2 Alginate-based TTI

5.3.2.1 *Fabrication and color evolution of alginate-based TTI*

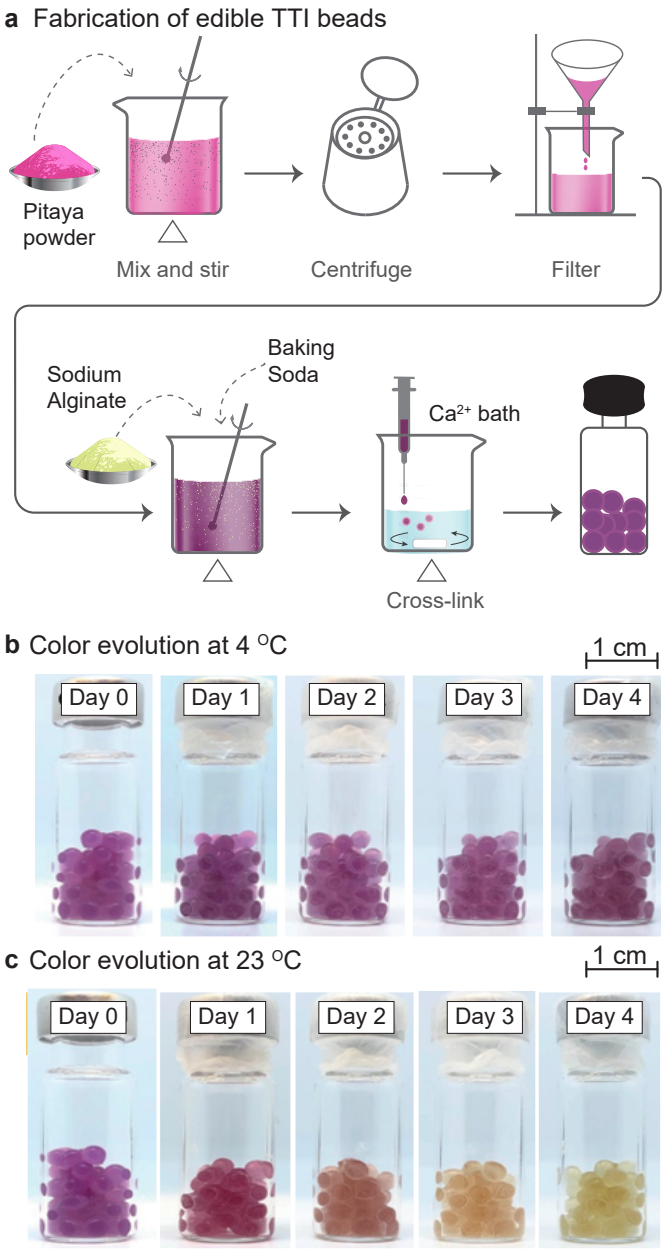

Figure 5.5: (a) Schematic of the edible TTI beads fabrication. (b) Color evolution is absent when a vial of edible TTI beads is kept at 4°C for 4 days (c) However, the TTI turns from purple to yellow under 23°C in 4 days.

To showcase the potential form of the Time-Temperature Indicator (TTI), we have taken a step further by encapsulating the pitaya extract into alginate. This encapsulation technique offers a way to present the TTI in a more practical and user-friendly format. The fabrication process of the alginate-based TTI consists of steps schematized in Figure 5.5(a) and detailed in Section 5.2.1.

To avoid any potential oral toxicity, our TTI beads are made of only food-grade ingredients, namely, purple pitaya, alginate, baking soda, and calcium chloride. We spherify the pitaya-alginate solution by extrusion dripping it through a syringe into a calcium chloride bath for cross-linking. After rinsing, the TTI beads are ready to use. The beads are always freshly fabricated and momentarily stored at 4 °C prior to colorimetric assays because TTI beads are sensitive to heat. The purple TTI beads transform to red, reddish-brown, brown, and yellow respectively in 4 days at room temperature but maintain the purple color at -4 °C as shown in Figure 5.5(b and c). More images of TTI beads of a different pH at various temperatures can be found in Figure D.S2 and D.S3.

Based on the above observations, no evidence is found that the heat sensitivity of the pitaya extract could be undermined or altered when incorporated into alginate hydrogel by drop spherification. A crash test was also conducted on the TTI beads to mimic the scenario when the TTI is damaged by accidents. Figure D.S5 shows that the deformation in the appearance does not influence the color evolution.

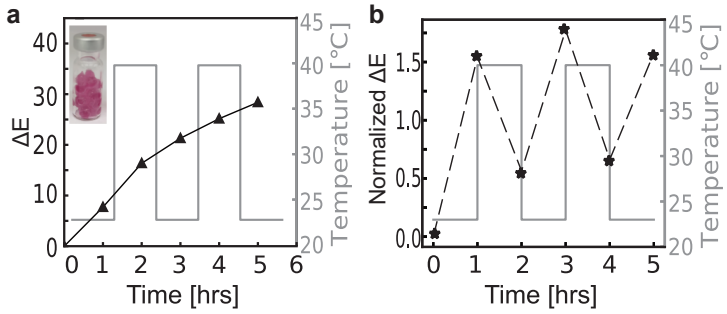

Figure 5.6: Color evolution represented as ΔE as a function of time. (a) Time course of ΔE values of TTI beads under alternating temperature between 23°C and 40°C (triangle). The temperature profile is schematized on the right y-axis. (b) displays the normalized ΔE values of TTI beads that scaled by ΔE values of pitaya extracts at 23°C and 40°C from Figure 5.1(c and d) respectively.

We further investigated the color transformation of TTI beads. pH 8 extract with its remarkable evolution in the short time window is selected for the development of the beads. Figure 5.6(a) shows the color change of the beads under alternating temperatures between 23°C and 40°C (triangle) which are maintained for 1 hour. ΔE values of liquid extracts under constant 23°C (circle) and 40°C (square) are duplicated from Figure 5.1(c

and d) for comparison. ΔE values of the beads are further normalized by that of liquid extracts as provided in Figure 5.6(b).

From Figure 5.6(a), we could see the ΔE values of the beads under the alternating temperatures are evenly distributed in the middle of the ΔE profiles of liquid extracts under constant 23°C and 40°C. It is conceivable to envision that the color transformation is sped up by 40°C and slowed down by 23°C. However, a delay in this alternation in color transformation is only revealed by normalization. As shown in Figure 5.6(b), the normalized ΔE is larger than 1 under 23°C but smaller than 1 under 40°C. This zigzag profile around 1 tells us that color evolution is an accumulation of changes over time that lag behind the chemical reactions. Thus, it is evident that the temperature fluctuation will affect the ΔE profile.

5.3.2.2 *Example Application*

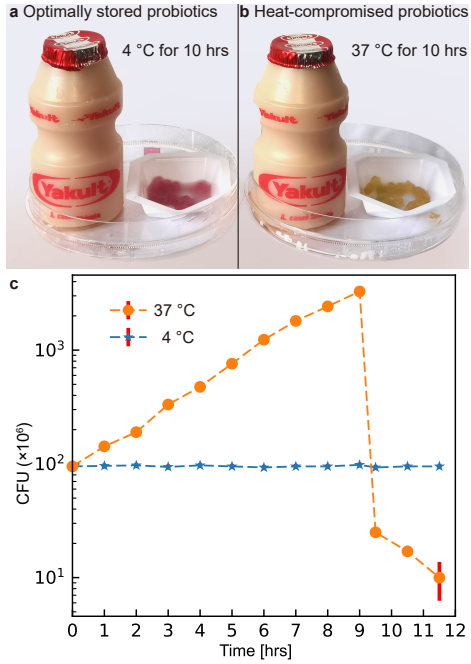

Figure 5.7: Demonstration of Edible TTI Functionality Supported by Microbial Testing: (a) Probiotics optimally stored at 4°C for 10 hours, maintaining good quality as indicated by purple beads. (b) Probiotics exposed to elevated temperatures at 37°C for 10 hours, resulting in compromised quality marked by yellow beads. Plate count tests reveal a reduction in the *L. casei Shirota* strain from the optimal storage level of 95 million CFU per milliliter in panel (a) to 25 million CFU per milliliter due to heat abuse. (c) Growth profiles of *L. casei Shirota*. Our TTI offers visual indicators: purple beads in (a) and yellow in (b) in case of heat abuse, providing a more reliable solution, especially when sensory detection of heat-induced damage is not feasible.

We anticipate that edible TTI can be utilized as a labeling tool for chilled food, particularly in situations where sensory detection of heat-induced damage is not feasible. Figure 5.7 presents an example of such an application. The *L. casei Shirota* strain, found in the popular probiotic-fermented milk drink Yakult, is known for its proven health benefits. It is recommended to store this probiotic drink below 10°C, and leaving it outside the refrigerator for extended periods should be strictly avoided [26]. Plate count tests reveal that, when exposed to 37°C for 10 hours, the *L. casei Shirota* strain decreases from the optimal storage value of 95 million CFU per milliliter (Figure 5.7 a) to 25 million CFU per milliliter (Figure 5.7 b). The growth profiles are shown in Figure 5.7 c. However, this significant reduction in strain viability cannot be detected through sensory means alone.

Here, our TTI serves as a reliable solution. Currently, we simply place the TTI beads next to the probiotic bottles. We acknowledge that further improvements, particularly in the area of printing technology, are necessary before commercial implementation can be achieved. However, a detailed discussion of this technical optimization is beyond the scope of this thesis.

5.4 Conclusion

Time-temperature indicators (TTIs) are active intelligent packaging tools that inform customers about the thermal history and the shelf life of the product during storage and transportation. In this study, we describe an edible TTI that contains a natural colorant betacyanin extracted from purple pitaya, sodium alginate, and baking soda that are widely used as food additives, and food grade $CaCl_2$ as the crosslinking agent. The thermochromic transform of betacyanin extracts was tuned by baking soda and exploited to report the temperature abuse while the sodium alginate functioned as the encapsulation matrix. Results show that the reported edible pitaya-based TTI alginate bead exhibits irreversible thermochromic change with a wide operating temperature range from 4 °C to at least 100 °C. The thermochromic change was accelerated by higher pH at a higher temperature. However, the gaseous atmosphere has a minor influence on the color spectrum evolution, demonstrating the conformity of this edible TTI in applications despite gas compositions. The reported TTI is proposed to label chilled perishable products that cannot be reliably assessed using sensory methods.

REFERENCES

[1] S. Wang et al. “Review of time temperature indicators as quality monitors in food packaging.” *Packaging Technology and Science* 28.10 (2015), pp. 839–867.

[2] *The problem of food waste*. https://foodprint.org/issues/the-problem-of-food-waste/. Accessed: 11-08-2022.

[3] *Food safety*. https://www.who.int/news-room/fact-sheets/detail/food-safety. Accessed: 11-08-2022.

[4] E. Sahin, M. Z. Babaï, Y. Dallery, and R. Vaillant. “Ensuring supply chain safety through time temperature integrators.” *The international journal of logistics management* (2007).

[5] Y. Zhang, Z. Hu, H. Xiang, G. Zhai, and M. Zhu. “Fabrication of visual textile temperature indicators based on reversible thermochromic fibers.” *Dyes and Pigments* 162 (2019), pp. 705–711.

[6] M. S. Firouz, K. Mohi-Alden, and M. Omid. “A critical review on intelligent and active packaging in the food industry: Research and development.” *Food Research International* 141 (2021), p. 110113.

[7] M. Mataragas, V. C. Bikouli, M. Korre, A. Sterioti, and P. N. Skandamis. “Development of a microbial Time Temperature Indicator for monitoring the shelf life of meat.” *Innovative food science & emerging technologies* 52 (2019), pp. 89–99.

[8] J.-R. Jhuang et al. “Development of immobilized laccase-based time temperature indicator by electrospinning zein fiber.” *Food Packaging and Shelf Life* 23 (2020), p. 100436.

[9] D. Wu et al. “Development and characterization of an enzymatic time-temperature indicator (TTI) based on Aspergillus niger lipase.” *LWT-Food Science and Technology* 60.2 (2015), pp. 1100–1104.

[10] Q. Li, M. Duan, W. Li, J. Hao, R. Li, et al. “Development and Testing of Fast Responsive Bi-Enzyme Time-Temperature Indicator.” *IOP Conference Series: Materials Science and Engineering*. Vol. 612. 2. IOP Publishing. 2019, p. 022043.

[11] Z. Uddin and W. Boonsupthip. “Development and characterization of a new nonenzymatic colored time–temperature indicator.” *Journal of Food Process Engineering* 42.4 (2019), e13027.

[12] B. Hu et al. “Development of a novel Maillard reaction-based time–temperature indicator for monitoring the fluorescent AGE content in reheated foods.” *RSC Advances* 10.18 (2020), pp. 10402–10410.

[13] C. T. Santos, P. Veiga-Santos, P. Sestari, N. C. Sorrini, and R. de Oliveira Roça. “Protein time–temperature sensor for intelligent starch polymers.” *Journal of Food Processing and Preservation* 44.5 (2020), e14428.

[14] C. Tang, N. M. N. MH, et al. “Stability of betacyanin pigments from red purple pitaya fruit (Hylocereus polyrhizus): influence of pH, temperature, metal ions and ascorbic acid.” *Indonesian Journal of Chemistry* 7.3 (2007), pp. 327–331.

[15] K. L. Yam and S. E. Papadakis. “A simple digital imaging method for measuring and analyzing color of food surfaces.” *Journal of food engineering* 61.1 (2004), pp. 137–142.

[16] K. M. Herbach, C. Maier, F. C. Stintzing, and R. Carle. “Effects of processing and storage on juice colour and betacyanin stability of purple pitaya (Hylocereus polyrhizus) juice.” *European Food Research and Technology* 224.5 (2007), pp. 649–658.

[17] F. C. Stintzing, A. Schieber, and R. Carle. “Betacyanins in fruits from red-purple pitaya, Hylocereus polyrhizus (Weber) Britton & Rose.” *Food Chemistry* 77.1 (2002), pp. 101–106.

[18] M. I. Khan. “Stabilization of betalains: A review.” *Food chemistry* 197 (2016), pp. 1280–1285.

[19] L. C. P. Gonçalves, B. M. Di Genova, F. A. Dörr, E. Pinto, and E. L. Bastos. “Effect of dielectric microwave heating on the color and antiradical capacity of betanin.” *Journal of Food Engineering* 118.1 (2013), pp. 49–55.

[20] K. M. Herbach, F. C. Stintzing, and R. Carle. “Betalain stability and degradation—structural and chromatic aspects.” *Journal of food science* 71.4 (2006), R41–R50.

[21] K. M. Herbach, M. Rohe, F. C. Stintzing, and R. Carle. “Structural and chromatic stability of purple pitaya (Hylocereus polyrhizus [Weber] Britton & Rose) betacyanins as affected by the juice matrix and selected additives.” *Food Research International* 39.6 (2006), pp. 667–677.

[22] K. M. Herbach, F. C. Stintzing, and R. Carle. “Stability and color changes of thermally treated betanin, phyllocactin, and hylocerenin solutions.” *Journal of Agricultural and Food Chemistry* 54.2 (2006), pp. 390–398.

[23] K. M. Herbach, F. C. Stintzing, and R. Carle. “Identification of heat-induced degradation products from purified betanin, phyllocactin and hylocerenin by high-performance liquid chromatography/electrospray ionization mass spectrometry.” *Rapid Communications in Mass Spectrometry* 19.18 (2005), pp. 2603–2616.

[24] A. Huang and J. V. ELBE. “Kinetics of the degradation and regeneration of betanine.” *Journal of Food Science* 50.4 (1985), pp. 1115–1120.

[25] T. A. Kandeepan G. “Modified Atmosphere Packaging (MAP) of Meat and Meat Products: A Review.” *Packaging technology and research* (2017).

[26] *About Yakult*. `https://www.yakult.co.in/about-yakult.php`. Accessed: 2023-06-22.

6

CONCLUSIONS

Leveraging the biocompatibility, swellability, and permeability attributes of hydrogel, we developed two on-does authentication measures for anti-counterfeiting purposes (Chapters 2 and 3). In addition, a humidity indicator (Chapter 4) and a time-temperature indicator (Chapter 5) for diagnosing food and pharmaceutical storage are designed respectively.

In Chapter 2, we present a microfluidic synthesis method for producing PEG microparticles with superparamagnetic colloids (SPCs) embedded at designated positions combining virtual magnetic moulds with stop-flow lithography. The hydrogel microparticles may function as an on-dose anti-counterfeiting measure for food and medicine. The embedded SPCs collectively act as a binary code matrix that can be read optically while their superparamagnetic nature makes the microparticles responsive to a magnetic field. However, we encountered issues in microparticle manufacturing such as untrapped SPCs settling in interstitial gaps of our Ni patches, as well as excessive trapping times. These scenarios result in unreliable encoding and reading of the binary code as well as unacceptably long production times. To overcome these experimental challenges, a combined scaling argument and finite element modeling were conducted. We identified $D_{void} : D_{patch}$=1 as the optimum experimental parameter to obtain a high trapping efficiency. Smaller or larger spacing will lead to a decline of magnetostatic force at the void and result in untrapped SPCs. To rule out such undesired scenarios, we proposed a washing strategy that has proven to compensate the undesired $D_{void} : D_{patch}$ ratio in the binary code. The proposed magnetic microparticles may inspire the development of quality control, tracking, and anti-counterfeiting technologies in order to combat increasing counterfeiting crime. Besides that, this approach successfully assembles SPCs into anisotropic patterns and traps them in a hydrogel matrix with desired 3D geometry, showing potential for synthesis of magnetically responsive structures such as microswimmers, micro self-propellers, and soft microrobots, not explored in this thesis.

In Chapter 3, we proposed a Physical Unclonable Function(PUF) working algorithm that utilizes sphere diameters and coordinates as inputs exploiting the uniqueness of PUF encryption. This is to the best of our knowledge the first study exploiting diameters and coordinates as a means to encode optical PUFs. Building on this know-how, two biocompatible on-dose PUF systems were developed drawing upon the entropy of the positions

of randomly distributed SPCs or oil droplets to showcase the single and multiple input(s) tags. The randomness and other performances of SPC-based PUF such as hamming distance and bit uniformity were evaluated and considered ideal. The reported PUF tags can be easily read without any special illumination source, and the algorithm is computationally efficient. Therefore, authenticity verification can be performed by end users with smartphones, rendering counterfeiting more difficult.

However, as a preliminary exploration of on-dose PUF using diameters and coordinates as inputs, there is still some work to do. For example, it would be interesting to calculate the encoding capacity with more diameter inputs to see where the limitation lies. We can also combine more input methods. If we cooperate with multiple edible fluorescent dyes and thus use colors as another layer of input, the encoding capacity will be significantly improved. In addition to that, exploring other edible systems and distribution methods such as emulsion polymerization of micro/nano droplets to get rid of SPCs would be of great importance to ensure food/pharmaceutical safety. With these in mind, we hope this study can be a good start to finally commercialize on-dose PUF tags. Moreover, in both optical and arbiter PUF architectures, it should be noted that environmental factors play a significant role. For the optical PUF, calibration of the input location is a concern. In this case, error-correcting techniques are used to increase the stability of the PUF while maintaining its security. Although key generation has zero error tolerance, PUF authentication usually incorporates an allowable error threshold, thereby decreasing the stability requirement, and often obviating the need for error correction.

In Chapter 4, we developed a caseinate/glycerol-based food-grade edible humidity indicator (EHI) that informs of undesired humidity exposure by irreversible mechanical bending. Once exposed to higher humidity, the EHI deforms and rolls on itself, informing the users of exposure to humidity. We characterized the dynamics and final geometry of EHI when exposed to high humidity levels as a function of EHI thickness and aspect ratio respectively. Moreover, the application of EHI has been demonstrated with a humidity-sensitive medical test kit. We proposed a rolling mechanism coupling hygroscopic swelling, glycerol diffusion, and water diffusion. This mechanism is substantiated by thermal gravimetric analysis and guides us to tune the lag time as well as response time by manipulating the layer thickness. Meanwhile, the final curvature of the rolled EHI is shown to depend on the aspect ratio under 80% relative humidity (RH). However, a realistic application of rolling should take temperature into account during the course of diffusion. This is not addressed in this thesis but is worth investigating in the future. Overall, the developed indicator shows the potential to detect perishable products exposed to unsuitable humidity levels in an irreversible manner.

In Chapter 5, we proposed an edible time-temperature indicator (TTI) that is composed of three constituents, i.e., betacyanin which is extracted from purple pitaya, a hydrogel matrix made of crosslinked sodium alginate, and a pH regulator baking soda. The ther-

mochromic transformation of betacyanin extracts reports the temperature abuse while the sodium alginate functions as an encapsulation matrix. The rate of color change was tuned by the pH agent baking soda. Results show that the reported edible pitaya-based TTI alginate bead exhibits irreversible thermochromic change under a wide operation temperature range from 4 °C to at least 100 °C. The thermochromic change was accelerated by higher pH as well as at a higher temperature. On top of that, the gaseous atmosphere has a minor influence on the color spectrum evolution, demonstrating the conformity of this edible TTI in applications regardless of gas compositions. The reported TTI is proposed to label chilled perishable products that cannot be reliably assessed using sensory methods.

Overall, hydrogels are a powerful base material for anticounterfeiting and food safety measures when combined with advanced manufacturing platforms and responsive molecules. The reader-friendly binarycodes and battery-less quality control indicators that are built upon smart hydrogels ensure safety on a single product level. Hydrogels empower end users to play a more active role in fighting against counterfeit and deteriorated products.

PART II APPENDIXES

a

APPENDIX TO CHAPTER 2 TEMPLATED HYDROGEL MICROPARTICLES FOR ANTICOUNTERFEITING

A.1 Mobile phase

For the mobile phase, the main challenge observed was the agglomeration of the SPCs in the microfluidic channel due to the Van der Waals interactions between particles as shown in Figure A.S1 (a). In this research the combination of ultrasonication and refractive index matching was tried to resolve this problem and get a good distribution.

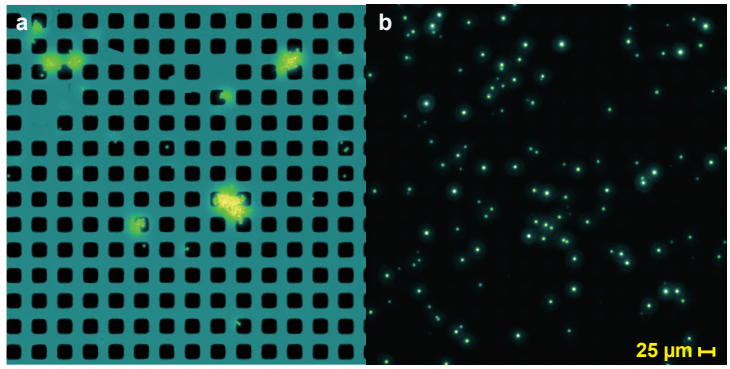

Figure A.S1: The agglomeration (a) was observed without refractive index matching and (b) be removed with edible cassia oil.

The 5 µm particles are made of around 80% polystyrene, which has a refractive index of 1.592.Hence, the edible Cassia Oil was decided to be implemented in the procedure due to its equal refractive index. Upon removing the water from the aqueous solution of the magnetic beads and adding this oil then followed by ultrasonication for 15 minutes, the following in Figure A.S1 (b) was observed.

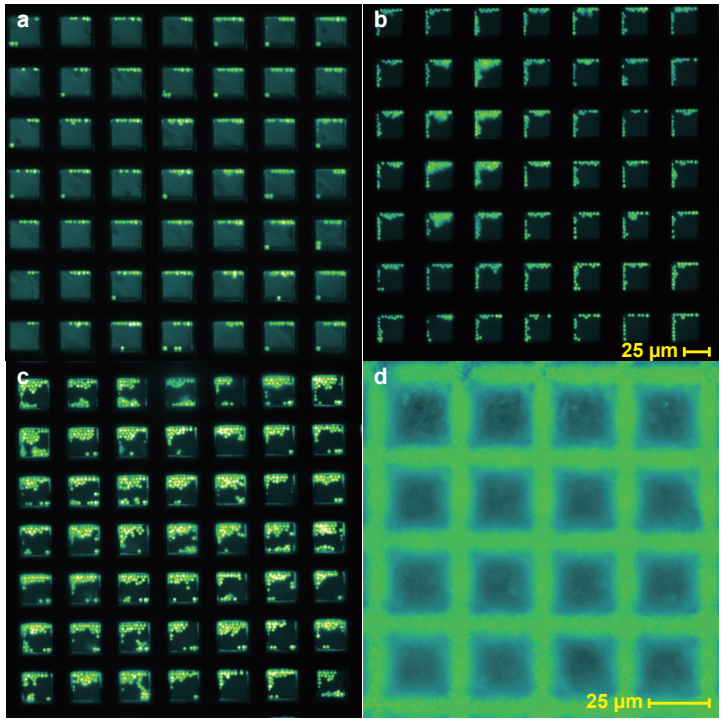

Figure A.S2: Influences of volume fractions on colloids trapping. The volume fractions and diameter of beads are respectively: (a)1.6%; 4.54 μm. (b) 2.4%; 4.54 μm. (c) 3.2%; 4.54 μm. (d) 12.0%; 1.00 μm.

When distributed well, the concentration of the mobile phase is not a problem any more to concern. Lower as 1.6% to higher as 12.0% of the volume percentage, the SPCs were neatly trapped by a Ni grid and the pattern agree to that of the grid as shown in Figure A.S2. However, as for a barcode, we prefer to one sphere per patch aligning. To achieve this, the concentration, size of the SPCs and Ni patches arrangement density should be coordinated which can be simply optimized by calculation and not the focus of this study.

A.2 Size and velocity, geometry and spacing based on COMSOL simulation

A.2.1 Size

A more detailed micrograd ients contour for Ni patches of different diameters is depicted in Supplementary Figure A.S3. In this simulation, all the D_{patch} equals to the D_{void} to minimize the change void will bring. All the slices were cut along the XZ surface through

the Ni patch center and only values for $|H(\vec{y})|\frac{\partial|\vec{H}|}{\partial(y)}$ larger than $10^{12}A^2/m^3$ was expressed in color. After that, the slice images were analysed by imageJ. The reach height (H) rises from 21.0 to 61.8 μm as the D_{patch} increases from 5 to 50 μm.

However, an unlimited increase in diameter is not desirable either. As diameter increases, located at the center of the Ni patch, the blank area where the magnetic force is rather weak will become larger. This phenomenon which is similar to the "skin effect" is proved in experimental results that the colloids were mostly trapped at the edge of the Ni patches. It will be equivalent to a hollow ring when the circle Ni patch is much larger than the colloids. An extremely big circle Ni patch will be a waste of Ni patch and barcode area. The colloids arranged along the periphery may provide additional magnetic force to attract the other ones into the panel layer by layer and lead to an uniform distribution as shown in Supplementary Figure A.S2 (c). Moreover, the large Ni patch may hinder the transmission of ultraviolet light and adversely affect the polymerization.

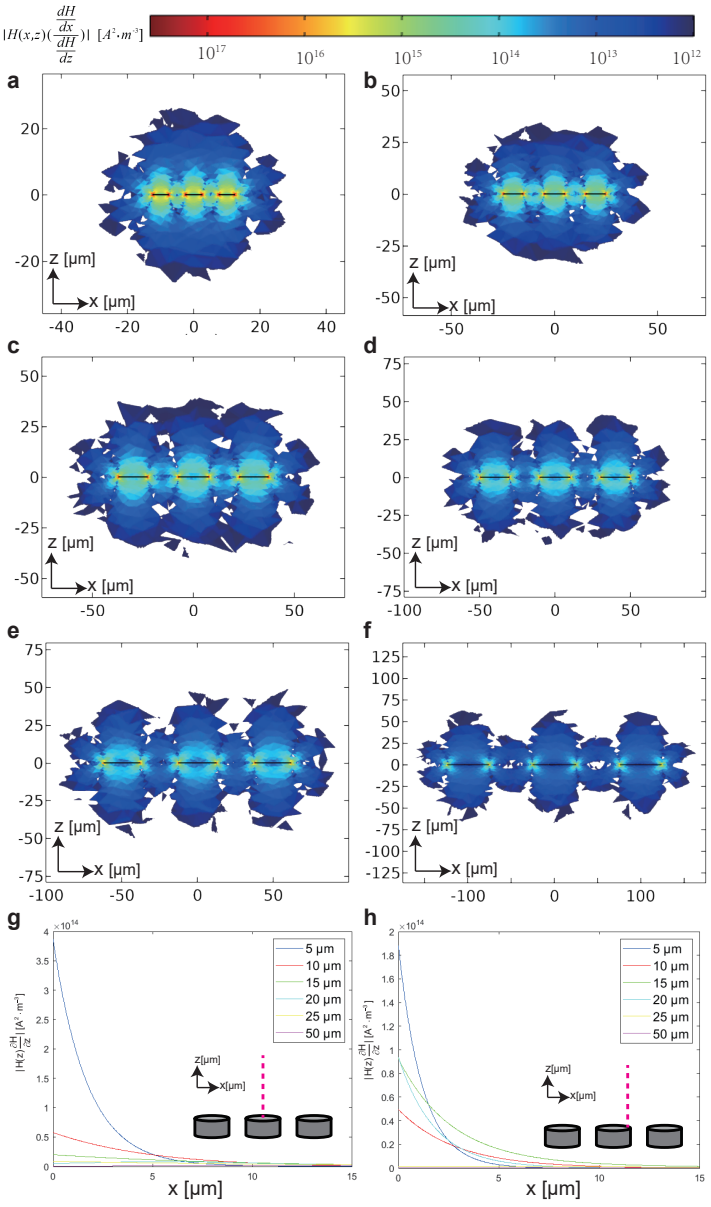

Figure A.S3: The magnetic field microgradients for different patch diameters obtained by COMSOL. (a)~ (f) are cut slices along the xz-plane; (g) and (h) are cutlines along z-axis in which (g) is along the center of a patch and (h) is the edge. (a) $D_{patch} = D_{void} =$ 5 μm; (b) $D_{patch} = D_{void} = 10$ μm; (c) $D_{patch} = D_{void} = 15$ μm; (d) $D_{patch} = D_{void} = 20$ μm; (e) $D_{patch} = D_{void} = 25$ μm; (f) $D_{patch} = D_{void} = 50$ μm.

A.2.2 Velocity profile

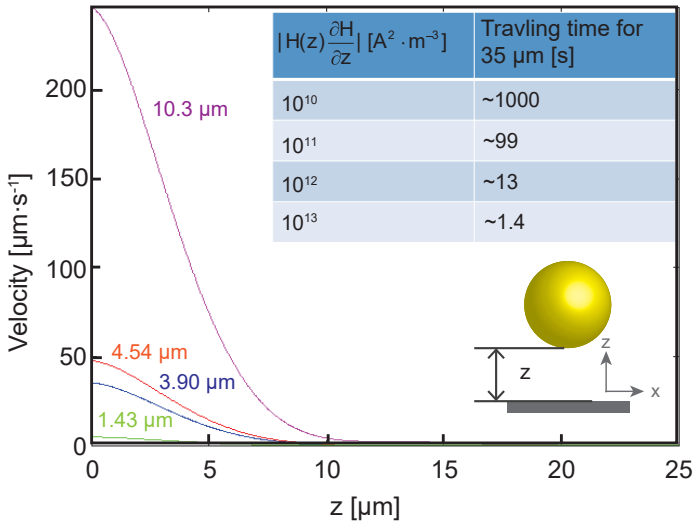

Figure A.S4: The velocity profile as a function of distance (z) from the patch for SPCs of various diameters. The table inserted gives an estimation of the traveling time over a height of 35 µm for 4.54 µm-diameter colloids under various constant magnetic microgradients.

With the knowledge of the dominating force, we summarized all the forces as shown in Equation A.S1.

$$\sum F_z = F_b + F_d - F_g - F_m + F_r \tag{A.S1}$$

Substituting Equations (1), (2) and A.S1, the settling velocity in z direction can be isolated in the form of Equation A.S2.

$$v_z = r^2 \cdot \frac{1}{\mu} \cdot [\frac{2}{9} \cdot (\rho_p - \rho_l) \cdot g + \frac{4}{6} \cdot \mu_0 \cdot \frac{\chi_{part} - \chi_{sol}}{\chi_{part} + 2\chi_{sol} + 3} \cdot |\vec{H}| \frac{\partial |\vec{H}|}{\partial (z)}] \tag{A.S2}$$

Random force F_r is a Gaussian variable, which on average is zero. Therefore, the average settling velocity v_z will not be influenced by F_r. Note that for an ensemble of trajectories, the standard deviation or variance in instantaneous z-velocities will be affected by the random force.

Based on Equation A.S2, the settling velocity for the SPCs used in experiments (D_{SPC}= 10.30, 4.54, 3.90 and 1.43 µm respectively) are calculated at different vertical distances

along z-axis for a canonical case of $D_{patch} = 5\mu m$ and their velocity profiles relative to the z position are provided in Figure A.S4.

Figure A.S4 gives an intuitive knowledge of the sediment speed. It can be noticed that the size of D_{SPC} exhibits a positive correlation with the velocity, this is an expected consequence of stronger F_m as previously discussed in Figure 2 (b). Moreover, it is evident that all SPCs are approximately stationary(~ 0 μm/s) when they are faraway from the patch regardless of the their size. Only when they are close enough to the patch, i.e., less than 10 μm, their velocities start to be influenced by the magnetic microgradients and exhibit a significant increase.

To further understand this, the microgradients profiles along x-z plane ($|H(\vec{x}, z)|\frac{\partial|\vec{H}|}{\partial(x,z)}$) of various D_{patch} are numerically evaluated in Supplementary Figure A.S3. From these profiles we found that the diameter of the Ni patch influences the height that the magnetic force can reach. Take D_{patch}= 5μm (Figure A.S3 (a)) as an example, the magnetic force can only reach to z=20 μm. The magnetic force turns weak beyond this range and consequently fails to aid the sedimenting. Assuming that most of the SPCs will flow along the center of the channel, here in this case study, a microfluidic channel in 20 μm height is supposed to be an efficient setup.

Besides the patch size, the x-z plane microgradients profiles of various geometries are numerically evaluated in Figure A.S5, A.S6. Our results presented in the supplementary information emphasize that geometries has minor influence on the magnetic microgradients in the z-axis.

Note that in the simulations in the supplementary, we use $10^{10}A^2/m^3$ as the minimum limit for the magnetic field gradient. All microgradients less than this value is omitted. This value is chosen based on the calculation in the insert of Figure A.S4. In this insert, the traveling time of a 4.54 μm-SPC across a 35 μm high microchannel is calculated to estimate the experimental accessibility. For convenience, we assume the vertical microgradient is constant along the trajectory towards the patch at 4 given values, i.e., 10^{10}, 10^{11}, 10^{12} and $10^{13}A^2/m^3$. Under a constant vertical microgradient of $10^{10}A^2/m^3$, a SPC will take $\sim$ 1000 seconds to sediment from in a 35 μm high microchannel. We further increase the vertical microgradient, for instance to $10^{12}A^2/m^3$, the travelling time is shortened to 13 seconds accordingly, which provides an experimentally desirable travelling time. Consequently, it suggests that a magnetic field strength gradient of at least $10^{12}A^2/m^3$ throughout the microchannel is necessary for effective trapping .

A.2.3 Geometries

The effect of the geometry of the Ni patch on the magnetostatic force was firstly investigated. Figure A.S5 shows $|H(\vec{x}, z)|\frac{\partial|\vec{H}|}{\partial(x,z)}$ values for different geometries of micro soft magnetic elements simulated by COMSOL. To enable comparisons between elements of

different geometries, the triangle, square, pentagon and circle were set up with same thickness of 200nm and the same area as the diameter of the circle is 5μm in separated air boxes. For example, the side length of the triangle, square and pentagon are 6.73, 4.43 and 3.38 μm respectively. $|\vec{H(z)}|\frac{\partial|\vec{H}|}{\partial(z)}$ components variation along z-axis crossing the center (Figure A.S5(b)) and edge (Figure A.S5 (c)) and slices crossing the center along the XZ surface (Figure A.S5(a)) were plot for each geometry.

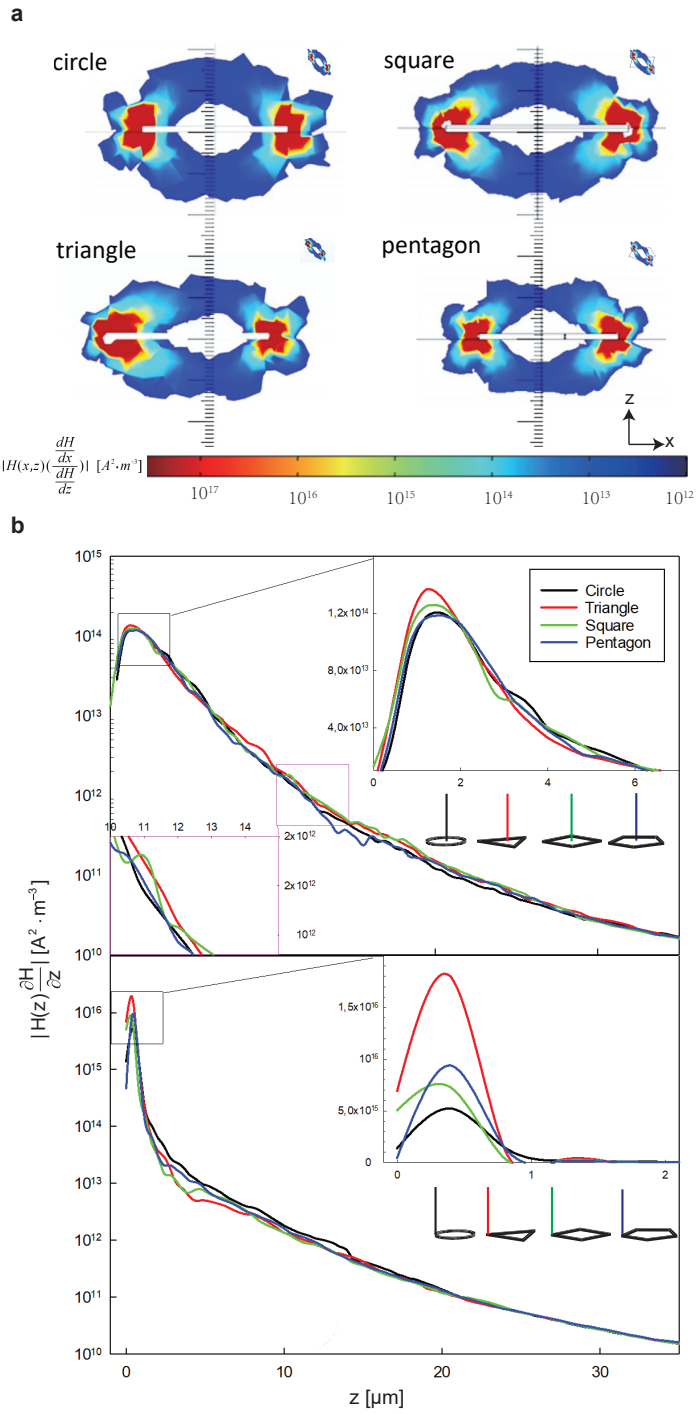

Figure A.S5: The magnetic field microgradient in the xz- plane on top of a Ni patch of various geometric shapes (circle, triangle, square and pentagon, dimensions 5×5×0.2 µm) obtained by COMSOL. (a) The cut slices in the xz-plane; (b) Semilogical plot of cutlines for the 4 geometric shapes in the center (top) and at the edge (bottom) along z axis.

Both the cut lines and the slices show that the geometries of the same thickness and area deliver similar performances. A reduced magnetic field in the periphery is induced once the Ni patch is activated by external magnetic field and generates The magnetic-field microgradients namely magnetostatic force acting on the SPCs. Rather than being the closer to the Ni patch the stronger the magnetostatic force is, but like a cap around the Ni patch where the magnetostatic force is relatively weak in center. The microgradient for all the 4 geometries sharply increase at the surface and dramatically decrease as it leave the surface. The maximum $|\mathrm{H}(\vec{z})|\frac{\partial|\vec{\mathrm{H}}|}{\partial(z)}$ for all the 4 geometries are at an order of 10^{17} which means the magnetostatic force will trap the SPCs tightly at the edge but not the center. The maximum reach (namely the height of the cap) for 1×10^{12} $\mathrm{A}^2/\mathrm{m}^3$ shows up in the center at around 10 µm in height and the maximum magnetostatic force generate at the vertices or edge. Another observation we would love to see is that the magnetostatic force can also act around the entity, as shown in the slices for all the 4 geometries in Figure A.S5 (a) , to pull the SPCs from the void to the Ni patches. Anyways, the geometry play a limited role in getting a higher reach for the magnetostatic force.

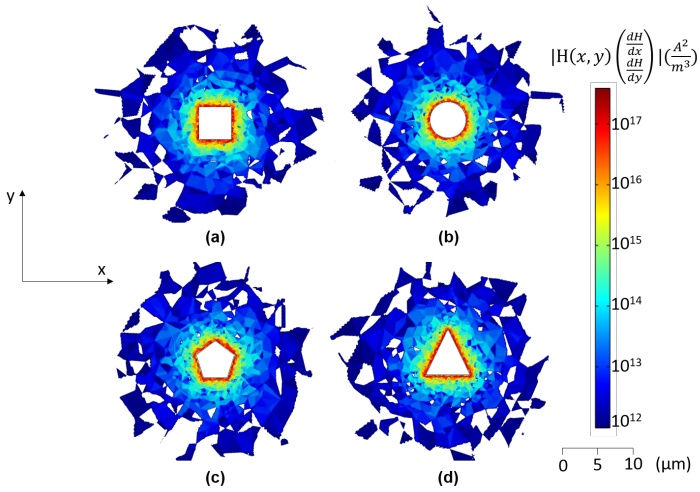

Figure A.S6: The magnetic field microgradient in the xy- plane on top of a Ni patch (z = 0.2 µm) for four different geometries, computed in COMSOL Multiphysics. Only values for $10^{12} \geqslant \frac{\mathrm{A}^2}{\mathrm{m}^3}$ are displayed. (a) Square. (b) Circle. (c) Pentagon. (d) Triangle.

While the trapping surface is in the same order for each geometry, triangle covers the biggest trapping surface. The paramagnetic microspheres have a preference to be trapped on top of the edges of a Ni patch as the microsphere is subjected to a larger magnetic field strength gradient at a edge. As such, it is likely that the center of the microsphere will we trapped on one of the three angles of the triangle, which might lead to inconsistencies for a uniform distribution of the microspheres. Despite of the discussion above, the geometries

has a limited influence on magnetostatic force reach compare to size and spacing. All the four geometries give a similar profile: the maximum reach (namely the height of the cap) for $1 \times 10^{12}\ A^2/m^3$ shows up in the center at around 10 μm in height while the maximum $|H(\vec{y})|\frac{\partial|\vec{H}|}{\partial(y)}$ and hence the maximum magnetostatic force generate at the vertices or edge.

A.2.4 Spacing

The magnetic-field microgradients $|H(\vec{x},z)|\frac{\partial|\vec{H}|}{\partial(x,z)}$ in the xz-plane for different patch voids are shown in Supplementary Figure A.S8. The three circular Ni patches with diameter of 5 μm and thickness of 200 nm are placed on z = 0 μm with different spacing are shown by the black lines. Only the value larger than $10^{12}A^2/m^3$ was expressed in color.

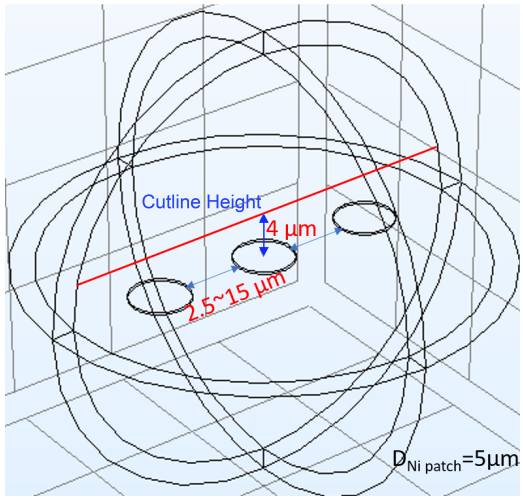

Figure A.S7: The scheme of the cutline position for void simulation

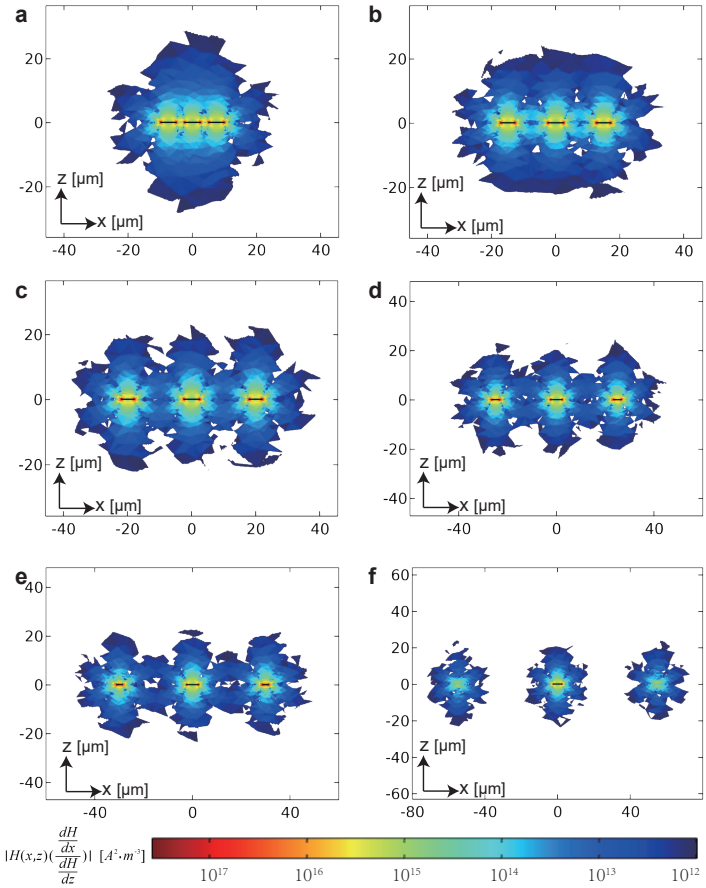

Figure A.S8: The magnetic field microgradients $|H(\vec{x},z)|\frac{\partial|\vec{H}|}{\partial(x,z)}$ in the xz-plane for 5 µm -diameter patches with different voids. D_{void} = (a) 5 µm; (b) 10 µm; (c) 15 µm; (d) 20µm; (e) 25 µm; (f) 50 µm.

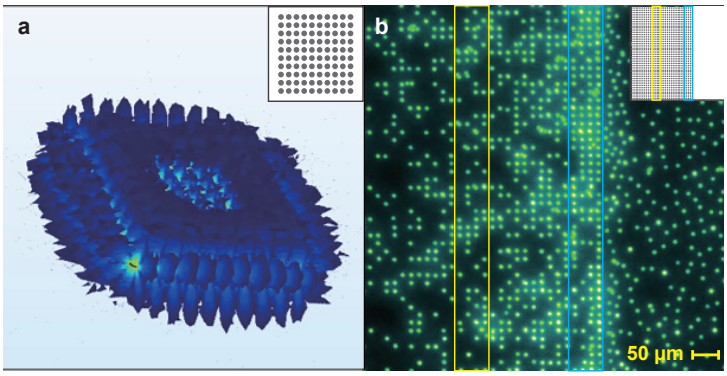

Figure A.S9: (a) The magnetic-field microgradient for 10 by 10 Ni patches array (as shown in insert). $D_{patch} = D_{void} = 5$ µm. (b) The SPCs line neatly along the periphery of the Ni patches array.

Acting as a big magnet, the magnetostatic force becomes smaller along from the array center to the periphery at where more colloids were trapped as show in Supplementary Figure A.S9. The simulation (Figure A.S9 (a)) is consist with the experimental result (Figure A.S9 (b)).

A.3 Validation

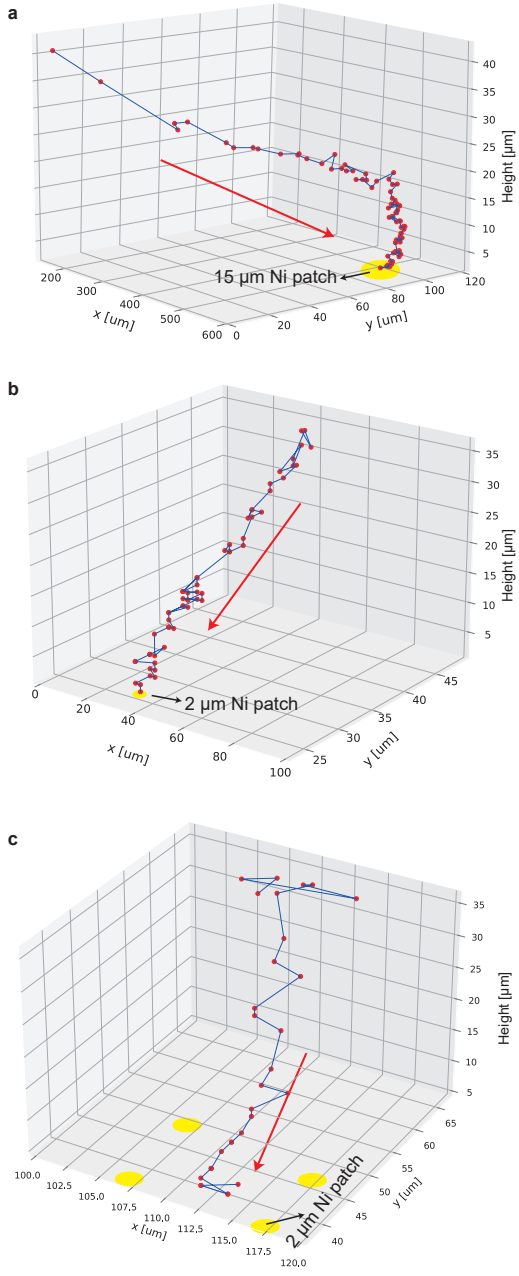

Figure A.S10: The particle trajectory rebuilt using Particle tracking velocimetry. (a) A 5 µm SPC moving to a 15 µm Ni patch and get trapped. A strong redirection can be noticed at the height of 10 µm. (b) A 5 µm SPC moving to a 2 µm Ni patch and get trapped. No redirection observed. (c) A 5 µm SPC moving to the void of several 2 µm Ni patch and be untrapped. No redirection observed. Data collected from movie S3, S4 and S5 respectively.

Figure A.S10 shows how a SPC moves in a microfluidic channel. When a SPC flowed above the 15 μm Ni patch, it moved down along an inclined line due to the gravity force and flow. Once it entered the magnetic force domain, i.e., 10 μm close to the Ni patch, the SPC changed its original direction and went straightforwardly to the Ni patch. However, such a redirection was not observed for 2 μm Ni patch. In Figure A.S10 (b), the SPC glided to the Ni patch all the way due to the flow and gravity force and happened to be trapped because it was lucky to be close enough to the Ni patch when it fell to the bottom. These observations agree with the dominating force analysis.

A.4 Movies

Movie A.S1: The hydrogel microparticles retain their structures and respond to the external magnetic field.

Movie A.S2: The barcode efficiency improves by the washing strategy.

Movie A.S3-S5: The particle trajectory movies for Particle tracking velocimetry analysis.

Scan to access the movies

b

APPENDIX TO CHAPTER 3 PUF MICROPARTICLES FOR ANTICOUNTERFEITING

B.1 Image processing

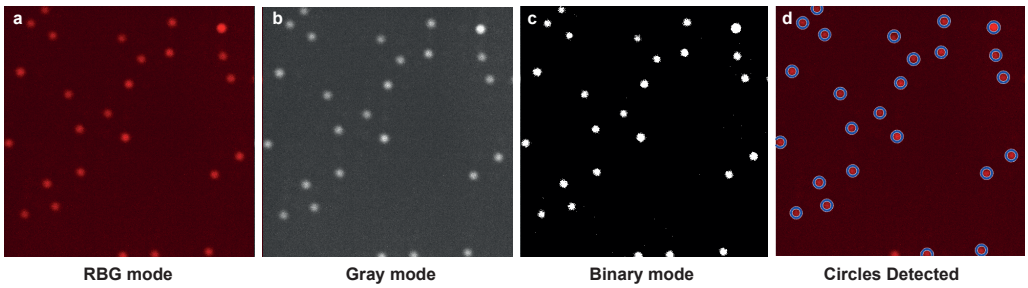

Figure B.S1: Image Processing. (a) Image resulting from the on-dose PUF device made with superparamagnetic microspheres of diameter 4.54 μm showing a physical area of 164 μmx164 μm. (b) The original RBG mode optical output response is converted to the grayscale image, the bright red SPCs can be clearly observed to be much lighter than the background in the gray mode. (c) The grayscale image with the bright SPCs is converted to the black-and-white image shown by binarising the pixels with a threshold of 0.15. (d) The circles detected within the image using Hough Transform in the binary black and white images plotted on the original color images. The MATLAB functions involved are shown in Table B.S1.

To elaborate, an image shown in Figure B.S1(a) was firstly converted to gray scale using build-in Matlab function *rgb2gray* thereby removing the color from the image. The gray scale image only retains the brilliance of each pixel. Figure B.S1(b) shows how the resulting image in gray scale looks after the conversion.

The grayscale images were then binarised using function *imbinarized* with a threshold luminescence input. This converts the pixels to black or white where every pixel with luminescence less than the threshold becomes black and the remaining white. A threshold of 0.15 was used to generate image (c) in Figure B.S1. Images produced under different lighting conditions might require the code to be adjusted slightly to produce the right out-

put depending on the contrast between the background and the microspheres in the image. In practice, the threshold could be automatically modified depending on the luminescence of the pixels by comparing to a reference image stored in the database.

In the last step, we apply function *imfindcircles* on the resulting image, and the pixel coordinates for the centers of the SPCs and the radii are extracted. Since all the SPCs are of the same diameter in the experimental on-dose PUF devices, the radius input is constantly set as 2.375 μm. If there were differently sized SPCs, then the radii would be used to group the centers in order to create more dimensions for the digital key. In order to demonstrate the accuracy of the detection of circles by Hough Transform with a sensitivity of 0.92 and edge threshold of 0.10 for the black and white images produced by binarising the images, the detected circles are redrawn on the original image for comparison which can be seen in Figure B.S1(d). The sensitivity and edge threshold were chosen such that all the SPCs, with more than half of its body in the image, are detected. The Matlab code can be found in Supplementary b.3.

B.2 Data for NIST statistical testing suite

Table B.S1: Image Processing Steps: The steps involved in digitizing the physical key are shown in the table with the corresponding MATLAB functions used.

Sl No.	Step	Description	MATLAB function
1	Optical Output Response Obtained	Images taken at x20 magnification and loaded into matlab	*imread*
2	Converted to grayscale	Color is removed from images based on luminescence of pixels	*rgb2gray*
3	Converted to binary	Pixels are binarised to hold either 0 or 1 based on a threshold of 0.15	*imbinarized*
4	Circles Detected	Centres and radii of circles estimated using Hough Transform with an edge threshold of 0.1 and a sensitivity of 0.92	*imfindcircles*

B.3 Matlab code

```
   clear all;
close all;
clc;

%read image
 im = imread('image.jpg');

% convert the image into grayscale
X = rgb2gray(im); % convert the image into binary scale or black and white
BW = imbinarize(X, 0.15);
% detect circles in image

   % call imfindcircles
[c,r]=imfindcircles(im,[20,35],'Objectpolarity','bright','Sensitivity',0.92,'EdgeThreshold',
0.1);

% display detected circles

figure();
imshow(im);
viscircles(c,r);
v=zeros(512,512);

% assign 1-bit for each bead to the right cell in the array
for i=1:length(r)
a=ceil(c(i,1));
b=ceil(c(i,2));
v(a,b)=1;
end
```

B.4 Images for performance investigation

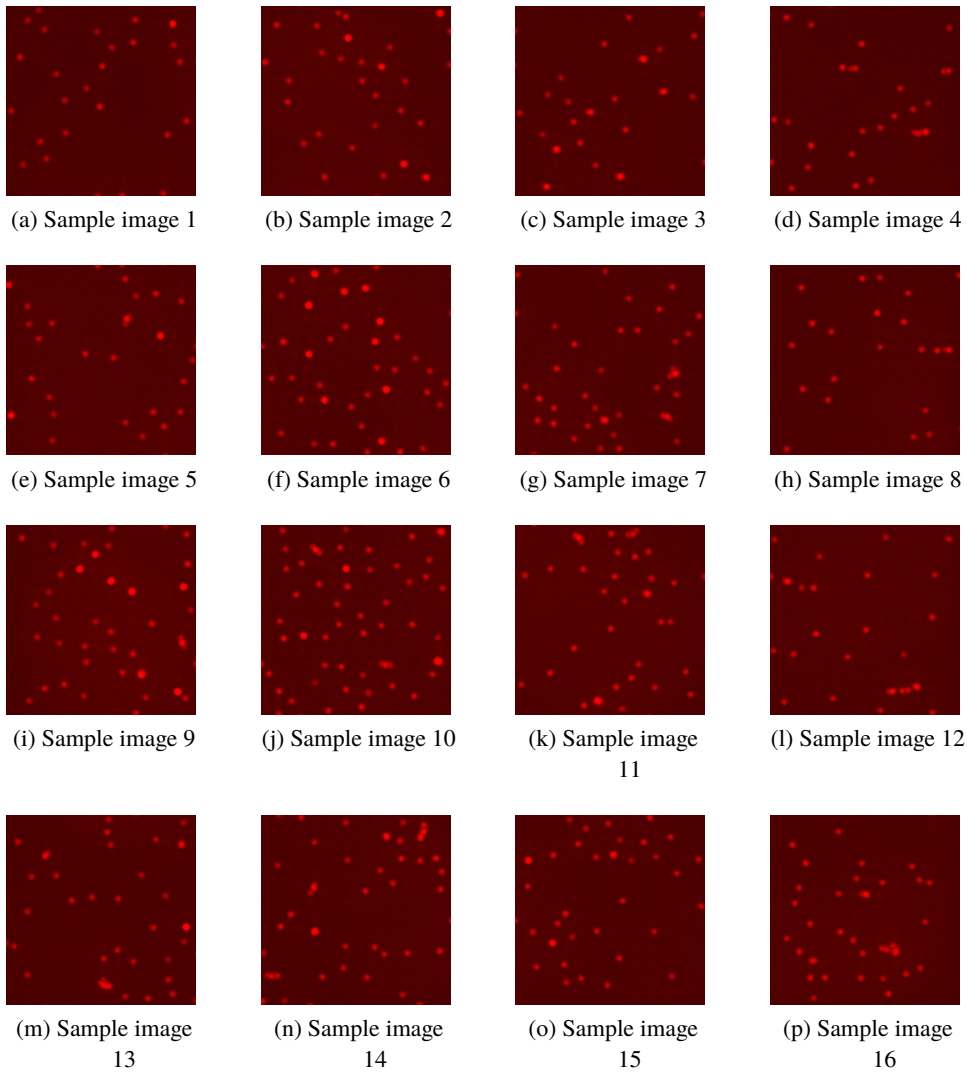

(a) Sample image 1 (b) Sample image 2 (c) Sample image 3 (d) Sample image 4

(e) Sample image 5 (f) Sample image 6 (g) Sample image 7 (h) Sample image 8

(i) Sample image 9 (j) Sample image 10 (k) Sample image 11 (l) Sample image 12

(m) Sample image 13 (n) Sample image 14 (o) Sample image 15 (p) Sample image 16

Figure B.S2: Images resulting from the PUF device made with microspheres of size 4.54μm showing a physical area of 164μm $\times$ 164μm each.

Data:

000010000011011100001100010010101001010100100000010100001101000010000
1100100001100010110000011000110000000000000010000001111111100011111010
0100101100100101100111010011011110100100000100000011110111110100111100
1000111101110100001111010001111011110111110110001001100010011001000101
0100110001011001011010110010100010111010011001000100010111001110010000
0101011000111101001000010100100001001111000001111010110000111111010101
1111101010100011010010101101000100000001110010010110010110110111101111
0111011010101000111110001011001101101000100000111010001011010111101001
0101011001010010011001000001001100111111000110000011011000000100000100000
1100001001110100000100101110011111101001001101111011101000010100100101
0110010100100110010000010011001111100011000001101100000010000100001100
1000000000101010111100011011000011011110001001101110001011110010011100
1101011101011110110011000010100100010010001100110000110100011100101010
0011011000011111100010101000010001001010100010000110001001000010110001
1000000111000001010000100100101010001011111011101010101000011000110100
0101100001100001110000000000010111101000

B.5 Raw results - NIST statistical test suite



Figure B.S3: Bitstreams from 16 on-dose PUF labels: The random bit sequences from the 16 on-dose PUF labels which was used for the NIST tests are given here.

Table B.S2: The full results of the NIST tests

Type of Test	P-Value	Conclusion
01. Frequency Test (Monobit)	0.0009246612603772096	Random
02. Frequency Test within a Block	0.001544703693384693	Random
03. Run Test	0.9754890621845419	Random
04. Longest Run of Ones in a Block	0.02483219666408431	Random
05. Binary Matrix Rank Test	0.29189144494343494	Random
06. Discrete Fourier Transform (Spectral) Test	0.4559083970315625	Random
07. Non-Overlapping Template Matching Test	0.3942821273821507	Random
08. Overlapping Template Matching Test	nan	Non-Random
09. Maurer's Universal Statistical test	-1.0	Non-Random
10. Linear Complexity Test	0.9856083034479547	Random
11. Serial test	0.1585, 0.2980	Random
12. Approximate Entropy Test	0.9999485439537766	Random
13. Cummulative Sums (Forward) Test	0.0016530836920858438	Random
14. Cummulative Sums (Reverse) Test	0.0018493225207545066	Random

B.6 Hamming distances

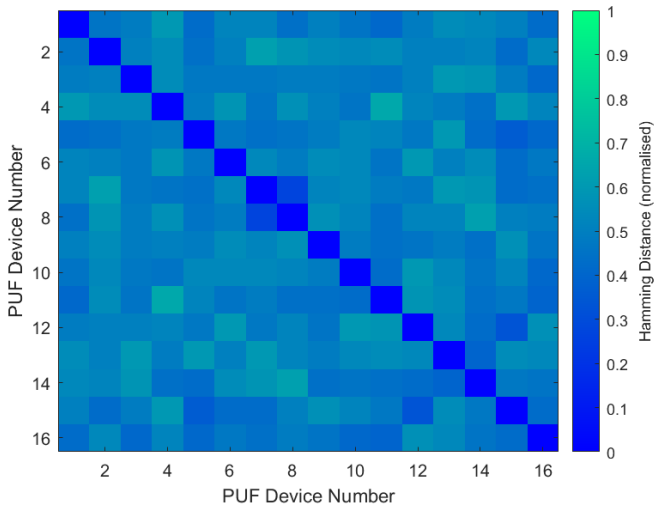

Figure B.S4: Hamming Distances between Devices. The hamming distance for each combination of pairwise PUF devices

C

APPENDIX TO CHAPTER 4 HUMIDITY INDICATOR

C.1 TGA test

Table C.S1 Specific decomposition temperatures of various edible humidity indicator (EHI) films

Sample	Stage I Dehydration of H_2O			Stage II Glycerol Decomposition			Stage III Casein decompostion			Residue sample @ 700 °C
	$T_{initial}$	T_{max}	T_{final}	$T_{initial}$	T_{max}	T_{final}	$T_{initial}$	T_{max}	T_{final}	
Sodium caseinate	100	160	195	-			270	325	370	23.8%
3% glycerol	60	105	135	195	265	285	290	325	360	15.7 %
14% glycerol	55	85	110	200	250	290	290	330	360	9.0 %
3% separated film		82			250			325		13.4%
14% separated film		78			252			325		13.9 %

C.2 Characteristic study of casein/glycerol film

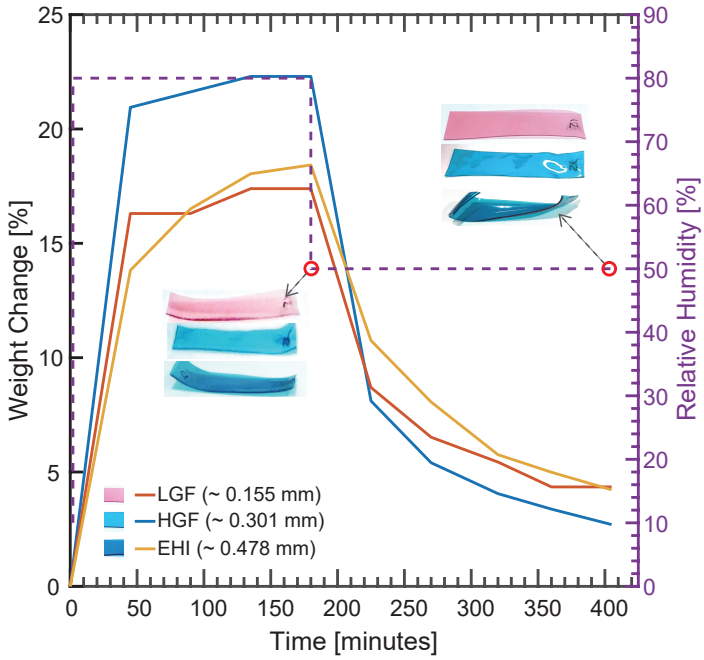

Figure C.S1: The moisture absorption and desorption performance of high glycerol film (HGF), low glycerol film (LGF), and a bilayer sensor composed of these two films (top) measured by the weight percentage change on the left Y-axis. The humidity course is represented by the purple dash line with the values on the right Y-axis. The thickness of the film is indicated in the legend. The macroscopic graphs of the three samples at equilibrium under relative humidity (RH) of 80% (bottom left) and 50% (top right) are displayed respectively.

In Hygroscopicity analysis we characterize the weight change of caseinate/glycerol films kept at 10% RH upon exposure to 80% RH first followed by exposure to 50% RH (dashed line in Figure C.S1). To do this, a set of moisture absorption experiments were conducted on a 0.155 mm-LGF, a 0.301 mm-HGF, and a bilayer indicator made of these two films in the humidity chamber. All the samples were cut into rectangular strips (45 mm x 13 mm). These samples were placed in the desiccator at 10% RH for 24 hours and then transferred to the environmental chamber (BTL-433, ESPEC) at 80% RH and allowed to equilibrate for up to 3 hours. After 3 hours, they were exposed to 50% RH and were weighed every 45 minutes until the weight became constant, indicating equilibrium with room humidity (Figure C.S1 (top)). The film response was recorded to visualize the bending process. All the measurements were conducted at a fixed temperature of 25 °C.

As depicted in Figure C.S1, the caseinate/glycerol film is moisture sensitive and responds to humidity changes in the environment. When films kept at 10% RH are exposed to high humidity conditions at 80% RH, the films adsorb water from the air as seen from the weight increase in the initial. They capture the water vapor and reach saturation within three hours independent of glycerol concentration. Upon exposure to room humidity of 50% RH, the films started to lose water immediately without hysteresis observed.

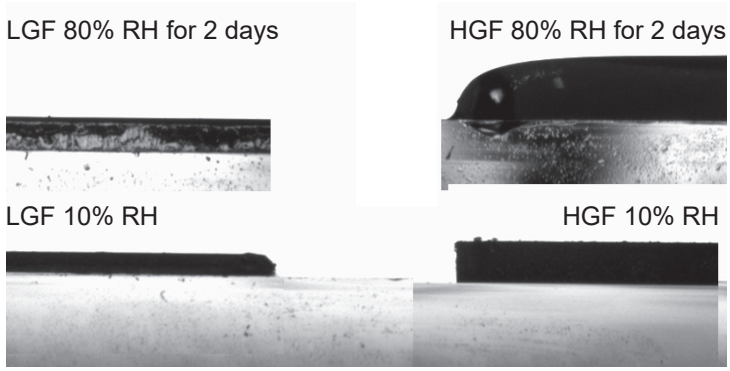

Figure C.S2: Thickness increase of LGF and HGF after exposure to 80% for 2 days.

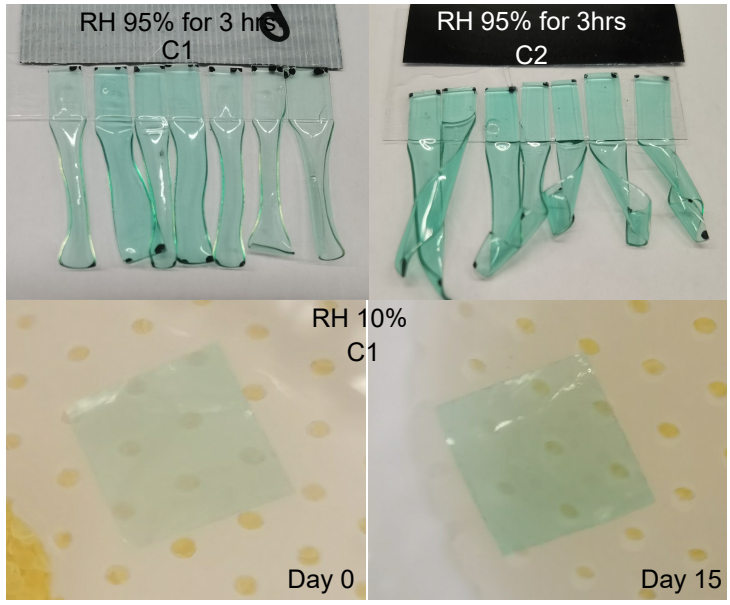

Figure C.S3: Images of EHIs bending under high RH (95%) and low RH (10%).

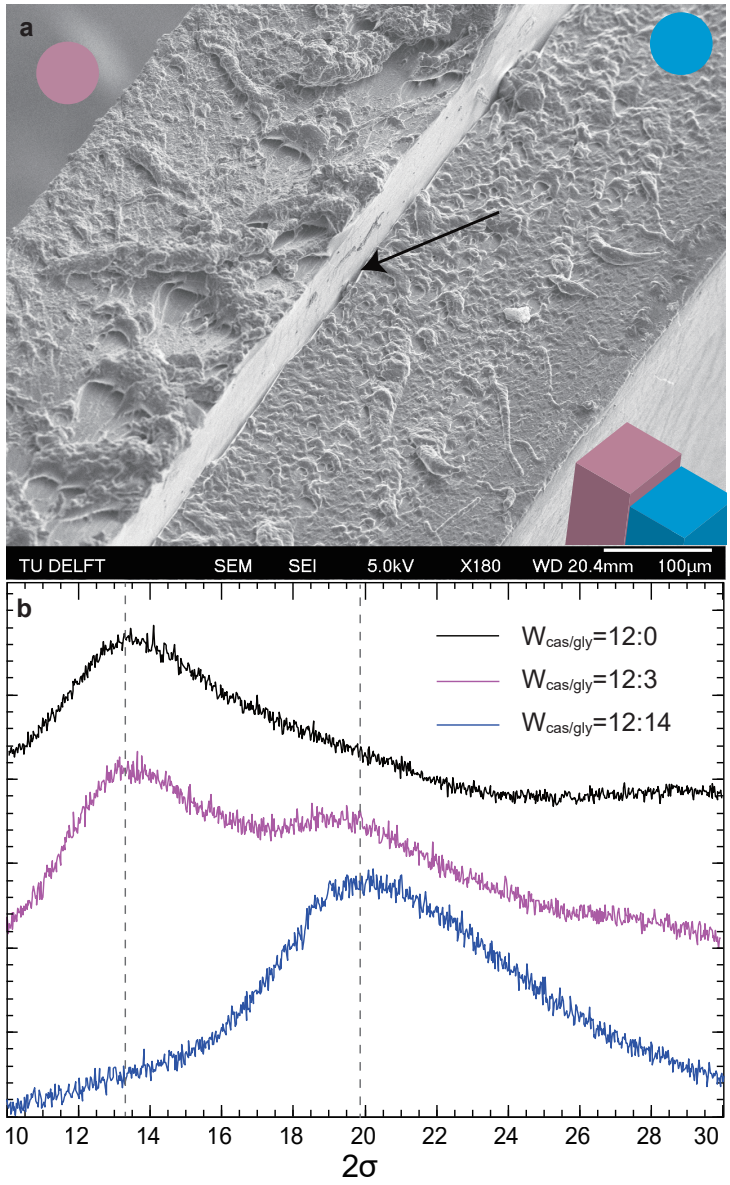

Figure C.S4: Scanning electron microscope image of the bilayer and X-ray diffraction (XRD) profiles of various single films. Panel (a) displays the cross-sectional scanning electron microscopy (SEM) images of the bilayer film. It can be seen that the two layers stick closely with a gap distance of less than 100 nm. There is an obvious difference between the two films. In the low-glycerol film (LGF), homogeneously distributed air-bubble-like shapes align along the interface. This is not seen in the high-glycerol film (HGF). HGF shows a homogeneous structure without any cavities. Enough amount of glycerol which acts as plasticizer aids in the elasticity of HGF meanwhile eliminated the incorporated air. Panel (b) shows the XRD analysis profiles of LGF, HGF, and pure caseinate film. The peak shifts from 13.5 to 20 with the increase of glycerol. In LGF, two peaks show up which means two forms of crystalline exist.

c.3 Bending behavior study

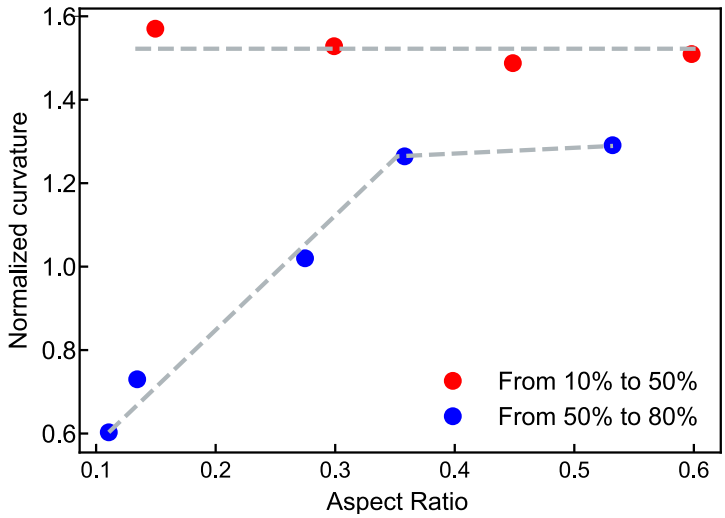

Figure C.S5: Normalized curvature of Combination 1 (C1) as aspect ratio. The composition of the C1 is 0.155 mm-HGF/0.155 mm-LGF. Relative humidity increased from 10% RH to 50% RH and 50% RH to 80% RH respectively.

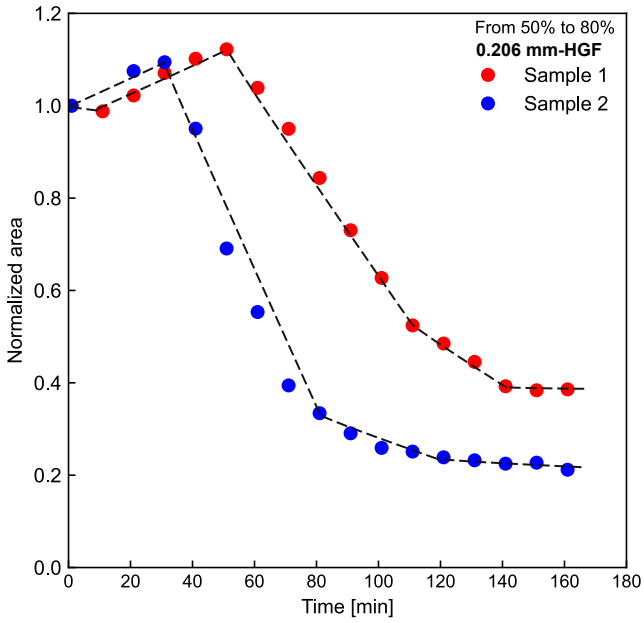

Figure C.S6: Normalized projected rolling area of Combination 2 (C2) as a function time. The composition of the C2 is 0.206 mm-HGF/0.155 mm-LGF. The conditioning RH is 50% RH and the test RH is 80% RH.

C.4 More example applications

Here we demonstrate two examples for food applications, i.e. a pharmaceutical tablet and a cashew nut under 80% RH. The EHI can be placed in direct contact with the showcased products without any concern due to its edible nature. We exposed the products and EHIs to 80% because this RH value is common during rainy weather. After two days' exposure, the EHIs attached to the tablet and cashew nut deformed and rolled on themselves to report exposure to the undesired humidity level. The effects of high humidity exposure for two days on these products are not unambiguously visible to the untrained eye yet the deformation of EHIs is easier to spot. As seen from the images, the tablet was only slightly swelled meanwhile the cashew nut looked the same as before but turned soggy and hard to break. The shape of EHIs for the tablet (strip) and the cashew nut (donut) was chosen for experimental convenience.

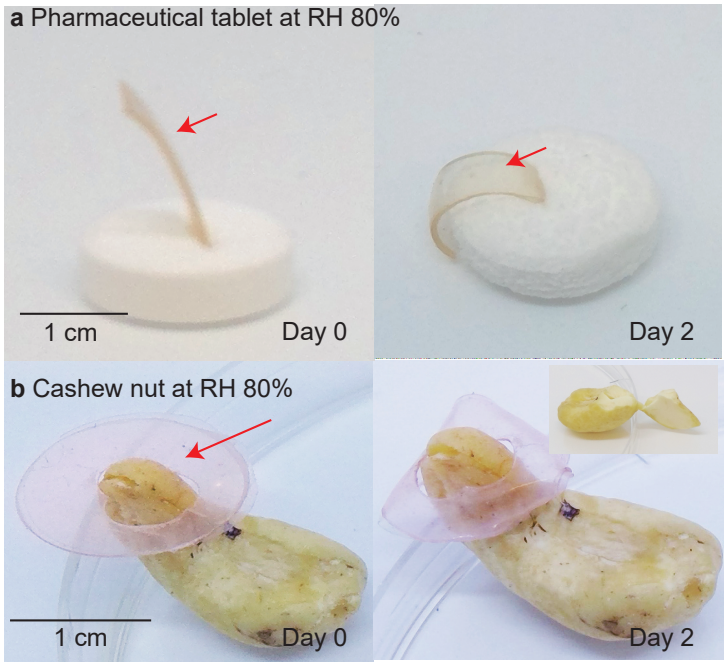

Figure C.S7: Two editor humidity indicator (EHI) applications

c.5 Movies

Movie C.S1: Video of the curvature development of the indicator attached to a urine strip.

Scan to access the movies

d

APPENDIX TO CHAPTER 5 TIME-TEMPERATURE INDICATOR

D.1 Two degradation pathways

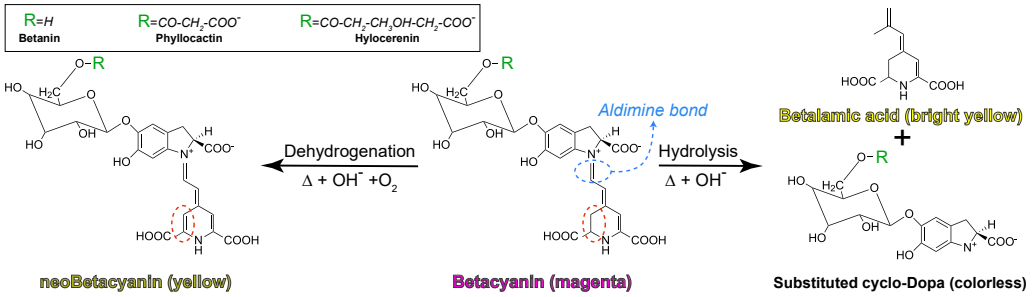

Figure D.S1: Two degradation pathways of betacyanin due to thermal treatment in an alkaline environment. Betacyanin tends to degrade into bright yellow betalamic acid and colorless cyclo-Dopa through the hydrolysis of the aldimine bond in the absence of O_2. When O_2 is brought in, the dehydrogenation takes place at locations highlighted by red dash circles to produce a yellow neobetacyanin[1].

D.2 Color evolution under various conditions

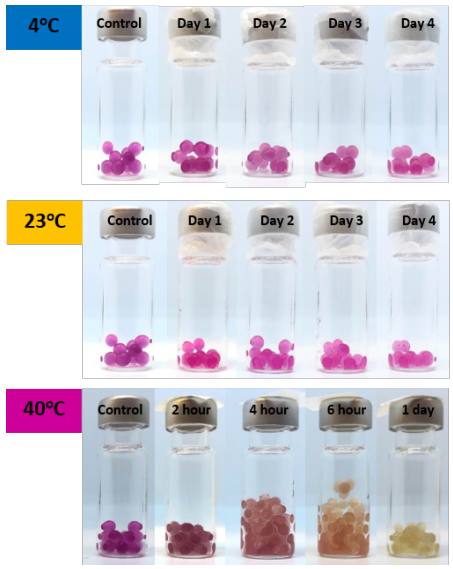

Figure D.S2: Colour change of alginate encapsulated pH 7 pitaya extracts at 4°C, 23°C and 40°C, respectively.



Figure D.S3: Colour change of alginate encapsulated pH 8 pitaya extracts at 4°C, 23°C and 40°C, respectively.

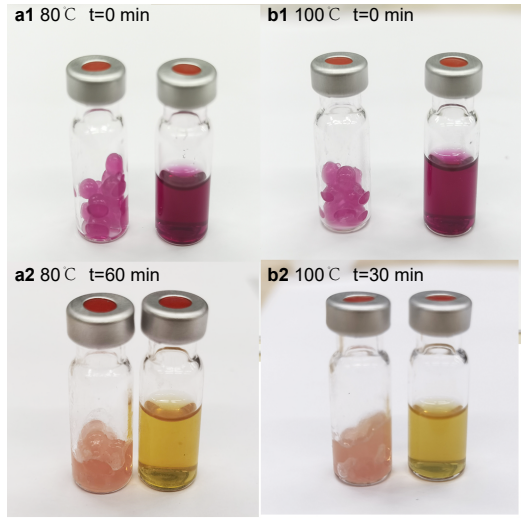

Figure D.S4: Image of pH 8 pitaya extracts and TTI beads at 80 and 100°C respectively. The higher temperature increases the color transformation.

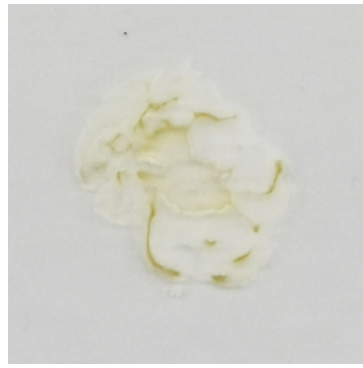

Figure D.S5: The image of a crashed pH 8 bead turned yellow under 80°C after 1 hour. The deformation of the bead has no influence on color change.

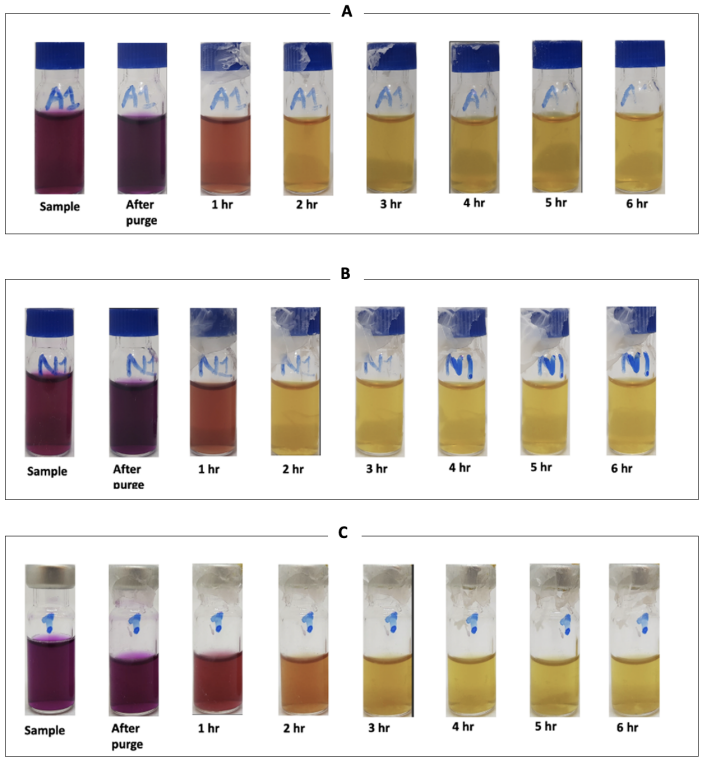

Figure D.S6: Images of pH 8 pitaya extract at 60 °C purged with (a) Compressed air, (b) Nitrogen, and (c)Modified atmosphere.

PART III

ACKNOWLEDGMENTS

I would like to express my deepest gratitude and appreciation to all those who have contributed to the completion of this doctoral dissertation. This work would not have been possible without the support, guidance, and encouragement of numerous individuals and institutions.

To begin, I would like to extend my heartfelt appreciation to my co-promotor/daily supervisor, Dr. H. Burak Eral, for granting me the opportunity to pursue my PhD within your research group. I am incredibly thankful for your valuable insights, consistently adding a fresh perspective to my work. You guided me through every aspect of my research and personal growth during my doctoral journey. Furthermore, I am genuinely grateful for the freedom you afforded me in choosing my research direction, assisting me in identifying intriguing topics and fostering my development as an independent researcher. It has been an absolute pleasure working under your mentorship and learning from you. People often refer to "survived" the PhD journey, but with you, I have truly thrived!

Equally important, I am eager to extend my heartfelt appreciation and sincere gratitude to my esteemed promotor, Dr. hab. Eduardo Mendes. Throughout the course of this dissertation, your profound knowledge, invaluable insights, and unwavering motivation have played a pivotal role in shaping its outcomes and contributing to my personal growth as a researcher.

I would like to extend my heartfelt thanks to the members of my doctoral committee, Prof.dr. J.H. van Esch, Prof.dr.ir. T.J.H. Vlugt, Prof.dr.ir. J.T. Padding, Dr. C.M.V.M Serra, Dr. Valeria Garbin, and Prof.dr. S.J. Picken, for their valuable input, constructive criticism, and suggestions that greatly enhanced the quality of this research. Their expertise and scholarly contributions have enriched my understanding of the subject matter and strengthened the academic rigor of this work.

I am immensely thankful to Dr. Ahmet Demirörs from ETH Zurich for his invaluable feedback and support during the challenging times of COVID-19 when accessing the lab was restricted. I am grateful for his assistance in preparing the cherished nickel patches. It was his brilliant idea on magnetic assembly provided the greatest insight, leading to my first publication.

I am sincerely grateful for the invaluable contributions of Dr. Jan Groenewold from UU, whose expertise and innovative thinking have played a vital role in the success of my research on humidity indicators. His insightful input and guidance have been instrumental in shaping the direction of my work and pushing the boundaries of knowledge in this

field. I deeply appreciate his commitment to fostering a collaborative and intellectually stimulating environment, which has greatly enhanced my research experience.

I would like to express my sincere appreciation to my master students, Ir. Alejandro Urbina, Ir. Thom Warth, Ir. Vishakh Menon, Ir. Abinaya Arunachalam, Ir. Roshan Akdar Mohamed Yunus, Dr. Aparna Raghunath and Ir. Amy Mok, for their unwavering dedication to my PhD research. Their consistent commitment, hard work, and enthusiasm have had a profound impact on the progress and outcomes of my doctoral journey. I am truly grateful for their steadfast pursuit of excellence, their valuable ideas, and their willingness to go the extra mile in their research endeavors. Their unwavering presence and contributions have brought fresh perspectives and invaluable insights that have greatly enriched the quality and depth of my work. I will always cherish their exceptional contributions and consider myself fortunate to have collaborated with such outstanding individuals. To those of you currently embarking on your Ph.D. journey, I sincerely hope that you are fortunate enough, just as I have been, to have the privilege of working with exceptional master students.

I would like to extend my deepest appreciation and gratitude to a group of exceptional individuals who have played a pivotal role in the success of my research. Dr. Hugo Perrin, Dr. Sevgi Polat, Dr. Zhao An, Dr. Niels Boon, Dr. Remco Hartkamp, Dr. Leong Zhiyi have all generously shared their valuable time, extensive experiences, and insightful perspectives, without which this research would not have been possible. They have enriched the quality and depth of my work, and I am truly fortunate to have had the opportunity to work with such remarkable individuals.

Hugo, I am consistently in awe of your incredible drawing skills. Our deep discussions have unveiled the source of your expertise in scientific drawing: your keen observation skills and unwavering attention to detail. I have gained an immense amount of knowledge from our interactions. Your broad understanding, distinct perspective, relentless pursuit of job opportunities, friendly nature toward everyone, and willingness to offer valuable input to others have truly inspired me. It saddens me that you have returned to France. I sincerely wish we could have the opportunity to share an office indefinitely, as your presence has had a profound impact on me.

Sevgi, my dear friend, before I had the pleasure of meeting you, I used to think that I worked diligently. However, in comparison to your incredible dedication, I feel a sense of shame. You truly amazed me when you helped me complete the TGA test, originally planned for two days, in just a single afternoon. Not only did you handle the data meticulously, but you also took the time to patiently explain it to me the following day, providing care akin to that of a nanny. Even when you were unwell, you worked tirelessly until the early hours of the morning. I, on the other hand, feel my age catching up with me and realize I cannot match your level of commitment, haha! I genuinely hope that we will have the opportunity to meet frequently in the near future.

Niels and Zhiyi, I must express my deep admiration for your exceptional guidance in structuring my manuscripts. On your initial reading of my drafts, you astutely identified the problem areas and provided critical inputs that ultimately saved my manuscripts. Your analytical thinking and invaluable insights have been instrumental in its improvement. Moreover, I cherish our conversations, whether it's venting about the food, discussing the weather, or even sharing anecdotes about my mischievous child. I find great joy in sharing with you every small milestone and achievement in my life. Thank you both for being not only outstanding advisors but also remarkable colleagues. Your support and camaraderie mean a lot to me.

I would like to express my heartfelt gratitude to Michel van den Brink, Jaap van Raamt, Junaid Mahmood, Bob Mulder, Kees Kwakernaak, Agnieszka Kooijman, and Liu Zhichao for their unwavering support and generosity in providing technical assistance to both myself and my students. Their willingness to go above and beyond in ensuring our success has been truly remarkable. Additionally, I would like to extend my thanks to the staff members who have consistently gone out of their way to facilitate our university experience: Leslie, Linda, Caroline, and Rob. Their invaluable help and support have made a significant difference in our academic journey, and I am truly grateful for their assistance. Here, I would like to extend a special appreciation to Leslie, whose assistance was invaluable in ensuring a smooth process for obtaining my visa and enabling me to start my first months in the Netherlands without any worries.

I also want to express my tremendous gratitude to my supervisors from my master journey: Prof. Bor-Yann Chen, Prof. Chang-Tang Chang, Prof. Yongtao Ding, Prof. Zhang Tielin, and Prof. Duan Baorong. Without your guidance, I wouldn't have achieved academic success or received the CSC scholarship for my doctoral journey. Your encouragement gave me the courage to step out of my comfort zone, leaving my permanent position at Yantai University. Thank you for paving the way and empowering me to pursue new opportunities.

I would like to express my sincere appreciation to Dr. Rishabh Ghotge, Dr. Luis Cutz, Prof. dr. Rene Pecnik, and (future Dr.) Marko Draskić for their invaluable advice on my pitching and my personal life. I am truly grateful for their generosity in sharing their knowledge and experiences, which have undoubtedly had a positive impact on my professional and personal development. A special thanks to Dr. Pedro Costa for his invaluable contribution in creating such a fantastic LaTeX template.

I would like to extend a heartfelt thank you to everyone in Erallab, including Rumen, Fatma, Nagaraj, Vikram, Yavuz, An Qi, Pingping, Willy, Casper, and many others. The moments we shared together, both inside and outside our joyful lab, have been truly special. I am grateful for the camaraderie, laughter, and friendship that made our time together so enjoyable. Your presence has made a significant impact on my journey, and I cherish the memories we created. Thank you for being a part of this incredible experience.

In addition, I would like to extend my deepest gratitude to my Chinese colleagues Fan Rong, Tao Xuan, Wei Liangyuan, Li Haoyu, Fu Shilong, Dong Teng, Li Heng, An Qi, Fang Bin, Guo Wenze, Cui Pingping and the Chinese son-in-law Zhiyi, for the countless homemade meals they graciously prepared. Gathering around the table, savoring their homemade dishes, and sharing stories have created cherished memories that will forever remain in my heart. I am immensely grateful for their thoughtfulness and the special bond we have formed through these shared meals. Thank you for nourishing not just my body but also my soul.

To the amazing individuals in 34-K-1-290, the most awesome office at TUD, including Rishabh, Nikolaos, Vilborg, Gustavo, Noura, Seyed, Stephan (half), Suriya, Marko, Hugo, Heng, Sevgi, Pingping, Irem, Elena, Sofen... A thousand words are omitted here. You know how much I love you guys! And Rishabh, my friend, you hold a very special place in my heart! I mean, if I wasn't worried about Zero breaking your roof, I would totally spend every New Year's Eve with you! Oh, and Marko, thank you for always being such a good friend to Zero!

I would like to express my heartfelt gratitude to Dr. Hanieh Bazyar, Dr. Arjo Loeve, and Prof. dr. ir. Thijs Runs for their trust and offering me the postdoc fellowship. Your belief in my abilities and the opportunity you have provided me with is truly appreciated. I am grateful for your support and the affirmation it brings to my past research, which serves as an inspiration to continue my journey. I would also like to extend my thanks to Rui-Paulo Cunha, my exceptional manager at Meatable, for your continuous support and encouragement. I am deeply grateful for the opportunities and guidance that have been bestowed upon me, and I am excited to contribute to the advancement of this field. Thank you once again for your trust and support.

I want to express my heartfelt thanks to everyone who has contributed to the development of my (future) startup, EatSens. Imge, Yvonne, Justin, Ruben and Dr. Emma Hinderink, your assistance at my patents are truly appreciated. Asier, Pablo, and Redena from YES!Delft, your assistance has been invaluable. I am deeply grateful to my mentor Pavel Cholakov and Vladimir Nedovic for their guidance and support. Special recognition goes to my co-founder, Liu Zhichao, for embarking on this exciting journey with me. I also extend my appreciation to the experts who have played a significant role in the success of EatSens. Jan-Willem Deutekom, Raymond Alves, Moshe, Wouter Robers, Wanda Stevens, Alex Dowdalls, Sonja Bruins, Ian Wachters, Johan Pieters, Jin Han, and many others, your expertise and wisdom have been truly invaluable. Your contributions have expanded the possibilities for my venture, and I am incredibly grateful for your support.

I would like to express my heartfelt gratitude to my parents and sister. As a rebellious member of the family, your initial incomprehension served as a driving force for me to succeed until this very day. To my dear friends: Sear and Safi, Bushra, Harman, my little

friend Hamza, Said, and Ahmed from Rembrandtschool, you have become like family to me, always providing warmth and support.

Lastly, I want to express my deepest gratitude to my little companion, Li Zelu (Zero). You have been the driving force that propelled me to embark on this doctoral journey. Your unwavering support has been the greatest source of motivation, carrying me through to the very end. You have shared in my moments of immense joy and profound sadness. Despite witnessing my occasional moments of madness, your love for me has remained constant. When people often remark, "Being a Ph.D. student and a mother must be incredibly challenging," I correct them by stating "My Ph.D. journey has been made easier by having a steadfast fan like you, always there to support me." All these little moments when you dipped your finger into the alginate solution, when you sat in front of my laptop to modify my "awful" figure, when you made the animation of my stop flow lithography procedure, when you tried to figure out how the bilayer bends upon absorbing the moisture, when you reminded me to go to bed, etc. are still vivid in my mind. Through my dedication and resolute determination, I wanted to demonstrate that I could achieve anything with hard work. And indeed, I have succeeded. I firmly believe that you, too, will accomplish remarkable feats in your future endeavors, just as I have done today.

Mengmeng Zhang
June 21st, 2023

CURRICULUM VITÆ

PERSONAL INFORMATION

FULL NAME: Mengmeng Zhang

BIRTH DATE: 02-05-1985

NATIONALITY: Chinese

EDUCATION

2019-2023: PhD Research Scholar,
Process & Energy Dpt., Delft University of Technology, The Netherlands.

2007-2010: MSc in Material Science, Yantai University, China;
Ilan Exchange Student, Ilan University, Taiwan (2009).

2003-2007: BSc in Polymer Science and Engineering, University of Jinan, China.

LIST OF PUBLICATIONS

[1] Zhang, M., Warth, T., Boon, N., Demirörs, A. F., Eral, H. B., Microfluidic Synthesis of Hydrogel Microparticles with Superparamagnetic Colloids Embedded at Prescribed Positions for Anticounterfeiting Applications. Advanced Material Interfaces 2022, 9, 2200899.

[2] Zhang, M., Arunachalam, A., Perrin, H., Polat, S., Groenewold, J., Mendes, E., Eral, H. B., An Edible Humidity Indicator that Responds to Changes in Humidity Mechanically, ACS Applied Polymer Materials 2023, 5 (7), 4780-4788.

[3] Zhang M., Raghunath A., Zhao A., Eral H. B., Biocompatible optical physically unclonable function hydrogel microparticles for on-dose authentication. Heliyon 2024, 10 (1), e22895.

[4] Zhang, M., Yunus, A.M.R., Menon, S.V., Mok, A., Hinderink, E., Eral, H. B., Food grade time-temperature indicator made of purple pitaya embedded alginate for perishable products, to be submitted.